Method development for the analysis of halogenated volatile and semi-volatile persistent organic pollutants (chlorinated, brominated, and fluorinated) using GC-APCI-T

Auteur : Capodici, Elisa
Promoteur(s) : 29906
Faculté : Faculté des Sciences
Diplôme : Master en sciences chimiques, à finalité approfondie
Année académique : 2025-2026
URI/URL : http://hdl.handle.net/2268.2/25434

FACULTE DES SCIENCES
Département de Chimie

MSLab – Professor Gauthier Eppe

Method development for the analysis of halogenated volatile and semi-volatile persistent organic pollutants (chlorinated, brominated, and fluorinated) using GC-APCI-TIMS-TOFMS

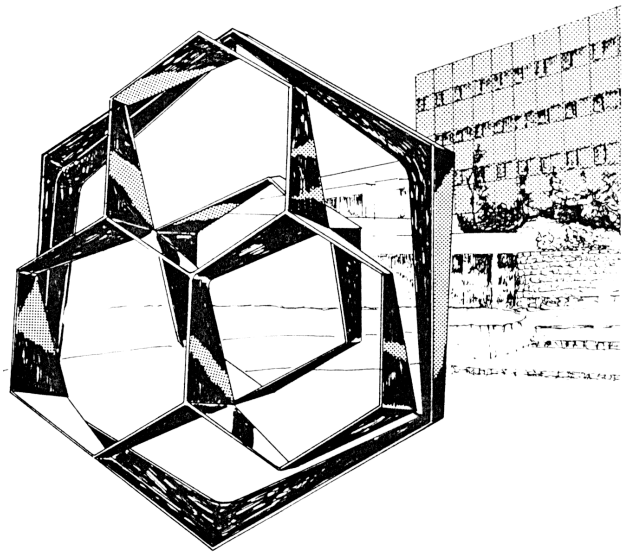

Année académique 2025-2026

Dissertation présentée par
Elisa Capodici
en vue de l'obtention du diplôme de
Master en Sciences Chimiques

I. Abstract

Volatile and semi-volatile halogenated persistent organic pollutants (POPs) are routinely monitored by gas chromatography coupled to mass spectrometry (GC-MS). However, the reliable identification and quantification of trace-level compounds can remain challenging, notably due to coeluting isomers and isobars. Adding an extra separation dimension by ion mobility spectrometry can improve overall separation performance and provide complementary identification information through collision cross section (CCS) values.

The aim of this Master's thesis was to develop and evaluate a gas chromatography–atmospheric pressure chemical ionization–trapped ion mobility spectrometry-time-of-flight mass spectrometry (GC-APCI-TIMS-TOFMS) workflow for the analysis of halogenated compounds relevant to POP monitoring.

In Chapter 1, a targeted GC-APCI-TIMS-TOFMS method was developed for three volatiles per- and polyfluoroalkyl substances (PFAS): perfluorooctyl ethanol, N-methylperfluoro-1-octanesulfonamide, and 2-(N-methylperfluoro-1-octanesulfonamido) ethanol. Instrumental parameters were optimized using a combination of one-factor-at-a-time testing and design of experiments, and fragmentation behavior was investigated under TIMS-off and TIMS-on conditions. A specific analytical issue, namely the broad ion mobility peak observed for N-methylperfluoro-1-octanesulfonamide, was explored and discussed.

In Chapter 2, food matrices prepared within the TEQfood project were analysed. Quantification results for emerging brominated and mixed halogenated POPs obtained using GC-APCI-TIMS-TOFMS were compared with those obtained using the reference GC-EI-sector high-resolution mass spectrometry (HRMS) method. While GC-APCI-TIMS-TOFMS enabled congener determination, it showed lower sensitivity for some ultra-trace congeners and tended to overestimate concentrations relative to GC-EI-sector HRMS for a subset of analytes.

Finally, Chapter 3 investigated pollutants sorbed on microplastics and macroplastics collected from rivers in Madagascar and from the Sambre River (Belgium), using targeted analysis with chlorinated biphenyl and polybrominated diphenyl ether standards combined with suspect screening to broaden chemical characterization.

Overall, this work highlights both the potential and current limitations of GC-APCI-TIMS-TOFMS for halogenated POP analysis and identifies methodological improvements required to extend the approach towards broader PFAS coverage and robust screening workflows.

II. Résumé

Les polluants organiques persistants (POP) halogénés volatils et semi-volatils sont couramment surveillés par chromatographie en phase gazeuse couplée à la spectrométrie de masse (GC-MS). Toutefois, l'identification et la quantification fiables de composés présents à l'état de traces restent délicates, notamment en raison de la co-élution d'isomères et d'isobares. L'ajout d'une dimension de séparation supplémentaire par spectrométrie de mobilité ionique permet d'améliorer les performances globales de séparation et d'apporter des informations complémentaires pour l'identification, via les valeurs de section efficace de collision (CCS).

L'objectif de ce mémoire de Master était de développer et d'évaluer une technique multidimensionnelle basée sur la chromatographie en phase gazeuse couplée à l'ionisation chimique à pression atmosphérique, à la spectrométrie de mobilité ionique piégée et à la spectrométrie de masse à temps de vol (GC-APCI-TIMS-TOFMS) pour l'analyse de composés halogénés pertinents dans le cadre de la surveillance des POP.

Dans le Chapitre 1, une méthode ciblée en GC-APCI-TIMS-TOFMS a été développée pour trois substances per- et polyfluoroalkylées (PFAS) volatiles : le perfluorooctyléthanol, le N-méthylperfluoro-1-octanesulfonamide et le 2-(N-méthylperfluoro-1-octanesulfonamido)éthanol. Les paramètres instrumentaux ont été optimisés à l'aide d'une combinaison d'approches « un facteur à la fois » et de plans d'expériences, et le comportement de fragmentation a été étudié en conditions TIMS désactivé et activé. Un problème analytique spécifique, à savoir le large pic de mobilité ionique observé pour le N-méthylperfluoro-1-octanesulfonamide, a été examiné et discuté.

Le Chapitre 2 porte sur l'analyse de matrices alimentaires préparées dans le cadre du projet TEQfood. Les résultats de quantification de POP émergents bromés et halogénés mixtes obtenus par GC-APCI-TIMS-TOFMS ont été comparés à ceux obtenus par la méthode de référence utilisant la GC-EI couplée à une spectrométrie de masse haute résolution à secteur magnétique (HRMS). Bien que la GC-APCI-TIMS-TOFMS ait permis la détermination des congénères, elle a montré une sensibilité plus faible pour certains congénères présents à l'ultra-trace et a eu tendance à surestimer les concentrations par rapport à la GC-EI-HRMS pour une partie des analytes.

Enfin, le Chapitre 3 s'est intéressé aux polluants adsorbés sur des microplastiques et macroplastiques collectés dans des rivières à Madagascar ainsi que dans la rivière Sambre (Belgique), en combinant une analyse ciblée à l'aide de standards de biphényles chlorés et d'éthers diphényliques polybromés avec une approche de criblage suspect afin d'élargir la caractérisation chimique.

Dans l'ensemble, ce travail met en évidence à la fois le potentiel et les limites actuelles de la GC-APCI-TIMS-TOFMS pour l'analyse des POP halogénés, et identifie les améliorations méthodologiques nécessaires pour étendre cette approche à une couverture plus large des PFAS et à des flux de travail de criblage robustes.

III. Remerciement

Je tiens à remercier Monsieur Eppe de m'avoir permis de réaliser mon mémoire au MSLab, ainsi que pour ses conseils.

J'aimerais remercier mon encadrant, Hugo, pour sa pédagogie et le savoir qu'il m'a transmis. Merci d'être resté présent et disponible, même après ton départ.

Je tiens également à remercier Georges ainsi qu'Aurore, qui m'ont encadrée après le départ d'Hugo. Merci à Georges d'avoir été mon second encadrant, pour son aide, ses nombreux conseils et sa patience. Merci à Aurore pour son aide dans les calculs théoriques et pour avoir répondu à mes nombreuses questions, malgré le fait qu'elle encadrait déjà une mémorante. Merci également à Laurie et Johan pour leurs conseils tout au long du mémoire.

Je remercie les membres du CART, Nathalie, Philippe et Cédric.

Je remercie également Omayma Missawi pour m'avoir permis de tester la méthode développée sur des échantillons de microplastiques.

Je remercie l'ensemble tous les membres du bureau pour leur bienveillance et le cadre de travail agréable qu'ils ont su créer : Wendy, Bastien, Lucas, Evan, Alexandre, Maude, Cédric, Stéphane (merci de m'avoir appris à jouer à la belote, maintenant je suis une pro), Aurélie (merci pour ton soutien) ainsi que les autres mémorants : Emeline, Maxime et Antoine.

Enfin, je souhaite remercier mon entourage personnel, mes parents, mes grands-parents, ma sœur et mon copain, pour leur soutien moral et leurs encouragements tout au long de ce travail.

Un outil d'assistance à la rédaction basé sur l'intelligence artificielle (ChatGPT) a été utilisé uniquement pour la correction linguistique et l'amélioration du style, sans contribution au contenu scientifique.

IV. Analytical techniques

A. Gas Chromatography

Gas chromatography (GC) is an analytical technique employed for the separation of volatile and semi-volatile compounds within a complex matrix. The separation is achieved based on the compounds' vaporization temperatures and the dynamic equilibrium established between the stationary phase and the mobile phase (i.e., the carrier gas).

The first step of gas chromatograph is the injection phase. There are three principal injection modes: split injection, splitless injection, and on-column injection [1]. In this study, the splitless injection technique was chosen, as it is particularly suited for the trace analysis of pollutants [1]. The sample is introduced through a septum into a glass liner. The liner is maintained at an elevated temperature, typically around 250 °C, above the boiling point of the solvent [1]. Thus, once a liquid sample is injected into the liner, it quickly vaporises.

Following injection, the gaseous sample is transferred to the head of the chromatographic column (Figure 1). At this point, the column is initially maintained at a low temperature [1], usually 10 to 20 °C below the solvent's boiling point. Consequently, the solvent condenses at the column entrance, effectively concentrating and trapping the analytes [1]. This results in sharp elution peaks and enhances resolution, according to equation 1.

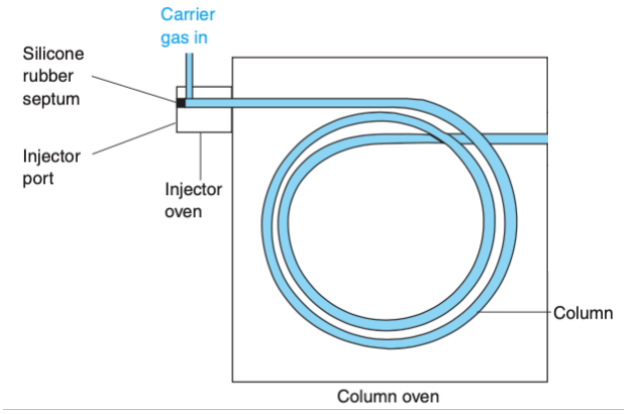

Figure 1: Schematic representation of a GC system [1]

$$R = \frac{t_{r,b} - t_{r,a}}{\frac{1}{2} * (w_a + w_b)} \quad (1)$$

Where,

- $t_{r,a}$ *and* $t_{r,b}$ are the retention times of two successive peaks
- w_a and w_b are the peak widths of two successive peaks

In a second step, a programmed temperature ramp is applied to the GC oven, inside which the GC column is located, allowing the sequential evaporation of the solvent and analytes and their migration through the chromatographic column [1]. In their gaseous state, the analytes are

transported by the carrier gas, which is supplied by a gas cylinder or generator. The carrier gas passes through the injector and enters the column, enabling the movement of compounds through it. Separation occurs as a result of the dynamic equilibrium established between the mobile phase (gas) and the stationary phase, which typically consists of polysiloxane-based polymers coated along the inner surface of the capillary column [1]. As analyte molecules travel through the column, they continuously partition between the two phases through repeated adsorption onto and desorption from the stationary phase [1].

Prolonged retention in the column leads to band broadening, caused by diffusion of the analytes from high-concentration regions to lower-concentration zones [1]. This results in broader peaks and a corresponding decrease in resolution (Equation 1). The efficiency of a chromatographic process is often described by the height equivalent to a theoretical plate (HETP or H), which represents the average distance a compound must travel to achieve equilibrium between the two phases [1]. This parameter can be optimized using the Van Deemter equation (Equation 2).

$$H = A + \frac{B}{u_x} + C * u_x \quad (2)$$

Where,

- A is the multiple paths term. However, in open tubular columns like most GC columns, it equals zero because the stationary phase covers the walls.
- $\frac{B}{u_x}$ is the longitudinal diffusion therm in the mobile phase. This therm represents the diffusion of analytes in the column from the high concentration regions to the low concentration regions.
- $C * u_x$ is the mass transfer term. It denotes the time required for the solute to reach equilibrium between the mobile and stationary phases.
- u_x is the linear gas rate (LGR).

When L (the length of the column) is divided by H, one obtains the number of theoretical plates (N). This is an indicator of the column's separation efficiency [1]. A higher number of plates corresponds to better resolution, as resolution is proportional to the square root of N (Equation 3) [1].

$$R = \frac{\sqrt{N}}{4} * \frac{\alpha - 1}{\alpha} * \frac{k_2}{1 + k_2} \quad (3)$$

Where,

- k is the retention factor. It is calculated by subtracting the dead time (t_m, the time it takes for an unretained compound, typically the solvent, to elute from the column) from the retention time of the analyte (t_r), and then dividing the result by t_m
- α is the selectivity factor (or relative retention). It represents the separation between two analytes and is calculated by dividing the higher retention factor (k_2) by the lower one (k_1)

B. Atmospheric pressure chemical ionisation

Following chromatographic separation, the next critical stage when mass spectroscopy is used as the detector is the ionization of analytes. In gas chromatography-mass spectrometry (GC-MS), the most commonly employed ionization technique is electron ionization (EI). EI is classified as a "hard" ionization method, meaning that it induces extensive fragmentation of analyte molecules [1]. While this can be advantageous for structural elucidation, it often results in the loss of the molecular ion, complicating compound identification [1]. Alternative ionization techniques, known as "soft" ionization methods, were developed and include Atmospheric Pressure Photo-Ionization (APPI), Chemical Ionization (CI), and APCI [1].
These soft methods are notable for preserving the molecular (precursor) ion, thereby facilitating more straightforward identification with tandem mass spectrometry [1].

Atmospheric pressure chemical ionization, which will be used in this thesis, has several operational and analytical advantages. First, APCI allows seamless switching from liquid chromatography-mass spectroscopy (LC-MS) to GC-MS coupling without breaking the vacuum of the mass spectrometer, which constitutes a significant operational benefit, especially since the two techniques are complementary [1]. Second, APCI usually offers enhanced sensitivity compared to EI [1]. In addition, it enables to facilitate compound identification as it preserves the molecular ion (precursor ion) [2]. Third, the carrier gas flow rate in APCI can be considerably higher than in EI sources due to the operation at atmospheric pression [2]. In the context of this analysis, this is a significant advantage because with H_2 as carrier gas, the optimal flow rate to obtained the lowest HETP is obtained at higher values compared to helium. Moreover, a higher flow rate reduces the residence time of analytes in the analytical column [1], thereby narrowing peak width and improving chromatographic resolution (equation 1).

In GC-APCI, the GC effluent is introduced into the ionization reaction chamber via a heated transfer line (figure 2). Ionization occurs within this chamber through a corona discharge, which is generated by a high electric field applied to a discharge pin under atmospheric pressure [3]. This process leads to the emission of electrons that, upon interaction with nitrogen gas, form a nitrogen plasma near the pin [3]. The resulting nitrogen cations (N_2^+) react with molecular N_2 to generate radical cations ($N_4^{+\bullet}$), which can readily ionize analyte molecules via charge transfer reactions, as described in Equation 4, [2]. This mechanism of ionisation is commonly referred to as ‘charge transfer’:

$$\begin{aligned} N_2 + e^- &\rightarrow N_2^+ + 2e^- \\ N_2^+ + 2N_2 &\rightarrow N_4^{+\bullet} + N_2 \\ N_4^+ + M^\bullet &\rightarrow M^{+\bullet} + N_2 \end{aligned} \quad (4)$$

Additionally, an alternative ionization pathway (‘proton transfer’) is possible in the presence of moisture or other proton donors, such as H_2 used as a carrier gas. In this mechanism, protonated analyte ions are formed through a series of proton transfer reactions involving the $N_4^{+\bullet}$ species and the proton source, as described in Equation 5 with water as an example [2]:

$$N_2 + e^- \rightarrow N_2^+ + 2e^-$$

$$N_2^+ + 2N_2 \rightarrow N_4^{+\bullet} + N_2$$
$$N_4^{+\bullet} + H_2O \rightarrow H_2O^{+\bullet} + 2N_2$$
$$H_2O^{+\bullet} + H_2O \rightarrow H_3O^+ + OH^\bullet \quad (5)$$
$$H_3O^+ + nH_2O \rightarrow H_3O^+(H_2O)_n$$
$$H^+(H_2O)_{n-1} + H_2O + N_2 \rightarrow H^+(H_2O)_n + N_2$$
$$H_3O^+(H_2O)_n + M \rightarrow [M+H]^+ + (n+1)\,H_2O$$

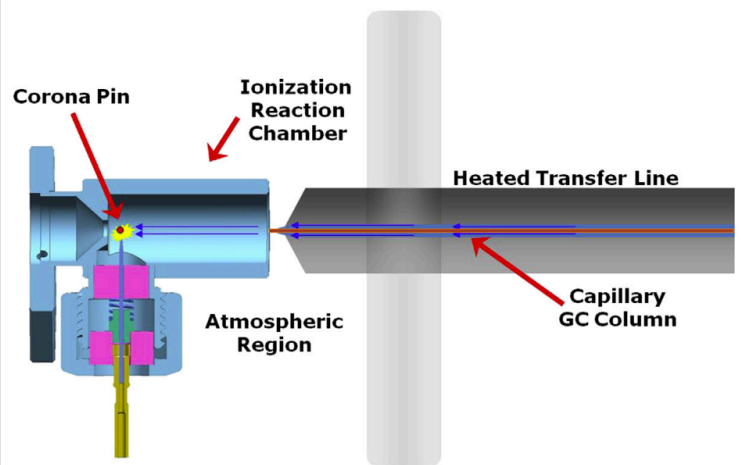

Figure 2: Schematic representation of the inside of an APCI source [2]

C. Ion Mobility

Ion mobility (IM) is a separation technique that discriminates ions based on their gas-phase conformation. This analytical approach offers several advantages. Notably, it enables the separation of isobaric compounds (i.e., compounds with the same nominal mass) and isomeric species (i.e., compounds with the same exact mass) [4]. As such, ion mobility enhances the overall separation capacity of analytical systems [4].

The fundamental principle of ion mobility relies on the application of a homogeneous electric field ($\vec{E}$), generated by a potential difference across a drift tube (Figure 3).

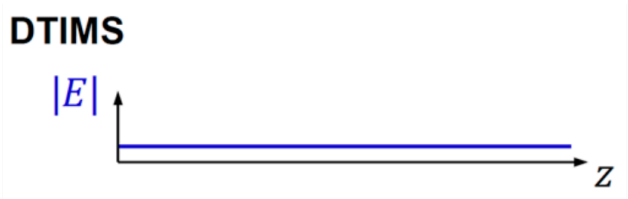

Figure 3: Schematic representation of the electric filed gradient used to trap ion in DTIMS [4]

Since the analytes are charged, they experience a force $\vec{F}$ described by the equation $\vec{F} = q * \vec{E}$ (where q is the charge of the compound and $\vec{E}$ is the electric filed), directing them along the field line [4]. On the other hand, these ions will collide with a buffer gas present in the drift cell, inducing a frictional force opposing the motion of the ions [4].
At equilibrium, when the electric force and the frictional force are equal in magnitude but opposite in direction, the ions reach a steady-state condition and traverse the drift tube at a constant velocity, denoted v_d [4]. This drift velocity is directly proportional to the electric field strength ($\vec{E}$), according to the relation (Equation 6) [4]:

$$v_d = K * \vec{E} \quad (6)$$

Where,

- the ion mobility K is the proportionality coefficient.

From the experimental ion mobility coefficient, the collision cross section (CCS or Ω) can be derived using the fundamental low-field equation (Equation 7) [4]:

$$K = \frac{3}{16} * \sqrt{\frac{2\pi}{\mu k_b T}} * \frac{ze}{\Omega N} \quad (7)$$

Where,

- μ is the reduced mass of ion-gas couple (g)
- k_b is the Boltzmann constant ($1{,}380649.10^{-23} J\,.\,K^{-1}$)
- N is the number of gas molecules per unit of volume (m^{-3})
- z is the net charge of ion
- e is the charge of an electron ($-1{,}602.10^{-19} C$)

The CCS provides critical information about the ion's shape and conformation in the gas phase, serving as a structural descriptor [4].

Several ion mobility technologies have been developed, but five main types are predominantly used in analytical sciences: the drift tube ion mobility spectroscopy (DTIMS), traveling wave IMS (TWIMS), differential mobility analyser (DMA), filed-asymmetric waveform IMS (FAIMS) and trapped ion mobility spectroscopy (TIMS) [4].

In this master thesis, measurements were performed using the TIMS technology (figure 4). This technique operates on principles similar to those described above, with specific modifications. TIMS uses a gradient electric field applied in the direction opposite to the gas flow to trap ions [4]. Ions are confined at specific positions along the electric field gradient (Figure 4), where their drift velocity and the opposing gas flow velocity cancel each other out [5]. This results in ion accumulation at distinct locations. Subsequently, ions are released sequentially by gradually decreasing the electric field gradient, enabling their elution according to mobility [5].

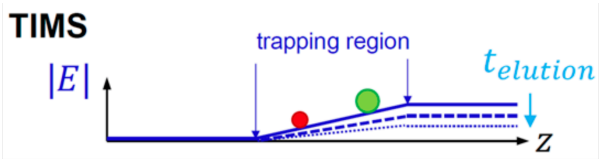

Figure 4: Schematic representation of the electric field gradient used to trap ion in TIMS [4]

D. Time-of-flight - Mass spectrometry

The final stage of compound analysis involves detection by a suitable detector. In chromatography, one of the employed detection methods is mass spectrometry (MS), which allows for both qualitative and quantitative analysis [1]. Mass spectrometry separates ions based on their mass-to-charge ratio (m/z) [1]. Various types of mass spectrometers are available, including quadrupole MS, ion trap MS, Orbitrap MS, and time-of-flight MS (TOF-MS [1]). In this master thesis, TOF-MS is used as the detector (Figure 5) [1].

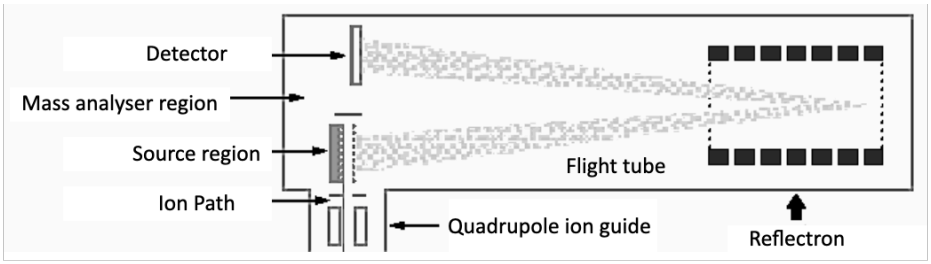

Figure 5: Schematic representation of TOF-MS [6]

After elution from the ion mobility cell, ions enter a source region, where a differential potential is applied. This potential converts electrical potential energy into kinetic energy of the ions (E_c, Equation 8), thereby accelerating the ions:

$$E_c = q * \Delta V \quad (8)$$

Where,

- q is the ion charge (C)
- ΔV is the applied voltage (V)

The ions are then propelled into the flight tube, a region under high vacuum and free of electric and magnetic fields, to minimize collisions with residual gas molecules [1]. However, due to slight differences in the initial spatial positions of the ions within the source region, ions of the same m/z ratio may acquire slightly different kinetic energies [1]. Consequently, ions with higher kinetic energy reach the detector more quickly than those with lower kinetic energy, which can reduce the resolving power (R) of the instrument [1].

To correct for this energy spread and enhance resolution, ions pass through a device called a reflectron before reaching the detector (Figure 5). The reflectron is composed of a series of electrodes with progressively increasing electric potentials [1]. It acts as an electrostatic mirror: ions with greater kinetic energy penetrate deeper into the reflectron and, therefore, follow a longer path compared to slower ions [1]. This compensates for differences in kinetic energy and

allows ions of identical m/z to arrive at the detector simultaneously, thereby improving mass resolution [1].

Another major benefit of TOF-MS is its high acquisition rate [1], which allows for the rapid collection of spectral data, which is particularly advantageous when analyzing fast chromatographic or ion mobility separations [2].

E. References

[1] Harris, Daniel C. Quantitative Chemical Analysis. Macmillan, 2010.

[2] Mullin, Lauren, Gareth Cleland, and Jennifer A. Burgess. 'Chapter 8 - Recent Advances in HRMS Analysis of Pesticide Residues Using Atmospheric Pressure Gas Chromatography and Ion Mobility'. In Applications in High Resolution Mass Spectrometry, edited by Roberto Romero-González and Antonia Garrido Frenich, 233–64. Elsevier, 2017. https://doi.org/10.1016/B978-0-12-809464-8.00008-7.

[3] Vadikkeettil, Yugesh, Yugeswaran Subramaniam, Ramaswamy Murugan, P. V. Ananthapadmanabhan, Javad Mostaghimi, Larry Pershin, Catherine Batiot-Dupeyrat, and Yasukazu Kobayashi. 'Plasma Assisted Decomposition and Reforming of Greenhouse Gases: A Review of Current Status and Emerging Trends'. Renewable and Sustainable Energy Reviews 161 (1 June 2022): 112343. https://doi.org/10.1016/j.rser.2022.112343.

[4] Gabelica, Valérie. 'Ion Mobility–Mass Spectrometry: An Overview', 11 November 2021. https://doi.org/10.1039/9781839162886-00001.

[5] Rid geway, Mark E., Markus Lubeck, Jan Jordens, Mattias Mann, and Melvin A. Park. 'Trapped Ion Mobility Spectrometry: A Short Review'. International Journal of Mass Spectrometry 425 (1 February 2018): 22–35. https://doi.org/10.1016/j.ijms.2018.01.006.

[6] ResearchGate. 'Figure 7. Schematic Structure of a Single-MS Time-of-Flight Mass...' Accessed 27 May 2025. https://www.researchgate.net/figure/Schematic-structure-of-a-single-MS-time-of-flight-mass-spectrometer-Applied-Biosystems_fig2_27516042.

V. Chapter 1: Development and optimisation of a method to analyse volatile PFAS on a GC-APCI-TIMS-TOFMS device

A. Introduction

1. Persistent Organic Pollutants

Persistent Organic Pollutants (POPs) constitute a class of chemical contaminants that have been widely used in agricultural and industrial applications since the 1940s [1].

They possess the ability to undergo long-range atmospheric transport [2]. Some POPs can exist in the gaseous phase at environmental temperatures [3]; thus, they are carried through the atmosphere and, depending on meteorological conditions, can be re-deposited in distant regions [2,3]. Moreover, the volatilization-deposition cycle may occur repeatedly [3], which explains why POPs are detected worldwide [2,4,5], even in remote areas where they have never been used, such as Antarctica and the Arctic Circle [2].

These compounds have been identified in various environmental matrices, including soil, water, biota, and even in synthetic particles such as microplastics (MPs). They are resistant to environmental degradation and therefore tend to persist and accumulate over time [2]. Additionally, POPs are resistant to metabolic breakdown [3] and are lipophilic, meaning they can accumulate in the fatty tissues of animals and humans, a process known as bioaccumulation [2,5].

This phenomenon has cascading effects within food webs: as animals consume contaminated prey, they accumulate POPs that cannot be easily eliminated. Consequently, the concentration of POPs increases at higher trophic levels, a process referred to as biomagnification [2].

In addition of persistence, bioaccumulation, and biomagnification, POPs are highly toxic. They are suspected of causing serious adverse effects on the health of both animals and humans, as well as on environment. Numerous studies report that exposure to POPs in humans is associated with cancer, immune and reproductive system dysfunction, and damage to the nervous and cardiovascular systems, among other health issues [2,4,5]. Similar effects have also been observed in wildlife [5].

Due to their key characteristics, long term toxicity, persistence against (bio)degradation, long-range transportation and strong potential for bioaccumulation, POPs represent a major threat to human health and the environment [1].

a) Brominated and chlorinated POPs

In response to these concerns, the Stockholm Convention on POPs entered into force in 2004, aiming to reduce and ultimately eliminate their production and use [1]. Among the “dirty dozen”

which are the twelve classes of POPs initially banned by the Stockholm Convention include polychlorinated dibenzo-p-dioxins (PCDDs) and dibenzofurans (PCDFs) (Figure 1), which are unintentionally generated as by-products of incomplete combustion and during the synthesis of other chemicals [1].

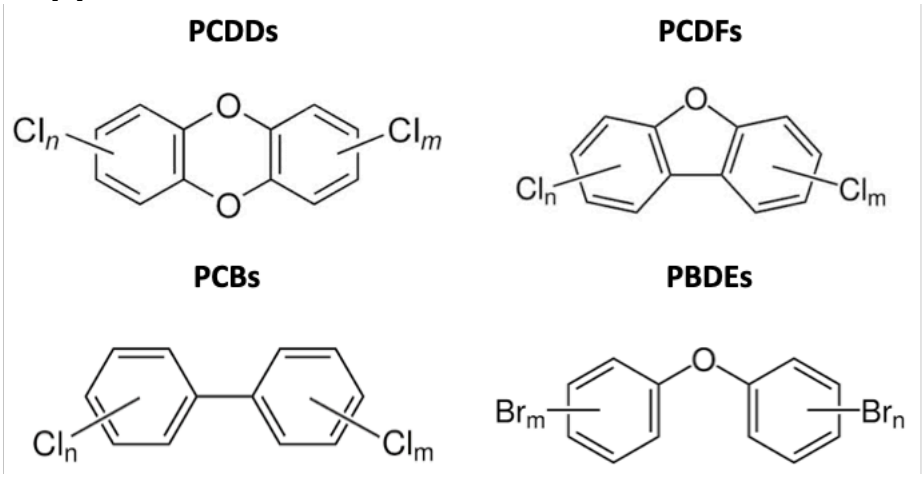

Figure 1: General chemical structure of PCDDs, PCDFs, PCBs and PBDEs [7,8,9]

Another prominent class includes polychlorinated biphenyls (PCBs) (Figure 1), formerly used in various industrial applications due to their desirable chemical properties. For instance, they served as additives in paints and as heat exchange fluids [9]. PCBs can also be formed as by-products in industrial processes [9]. Subsequently, additional compounds such as polybrominated diphenyl ethers (PBDEs) (Figure 1) were added to the Convention. These highly toxic substances were extensively utilized as flame retardants in numerous consumer and industrial products [9].

b) PFAS

A recently added groups of POPs, the per- and polyfluoroalkyl substances (PFAS), are characterized by hydrophobic and lipophobic properties [10]. In addition, PFAS possess carbon-fluorine (C-F) bonds, which are among the strongest and most stable chemical bonds known. This structural feature confers remarkable chemical and thermal stability to these compounds [10]. Owing to these unique properties, PFAS have been widely used in various applications and products such as firefighting foams, cosmetics, textiles, nonstick cookware, waterproof fabrics, fast-food packaging, and many others [11,12].

PFAS can be divided into two main categories: non-volatile, and volatile or semi-volatile compounds. To date, most analytical studies have focused on the non-volatile PFAS, primarily because the most commonly used technique is liquid chromatography-mass spectrometry (LC-MS) [10]. This focus is also reflected in the Stockholm Convention, which lists several non-volatile PFAS among its regulated substances, including perfluorooctane sulfonic acid (PFOS) and its salts, perfluorooctane sulfonyl fluoride (PFOSF), perfluorooctanoic acid (PFOA), its salts, and PFOA-related compounds (with certain exceptions); and perfluorohexane sulfonic acid (PFHxS) (Figure 2), its salts, and PFHxS-related compounds [13,14,15].

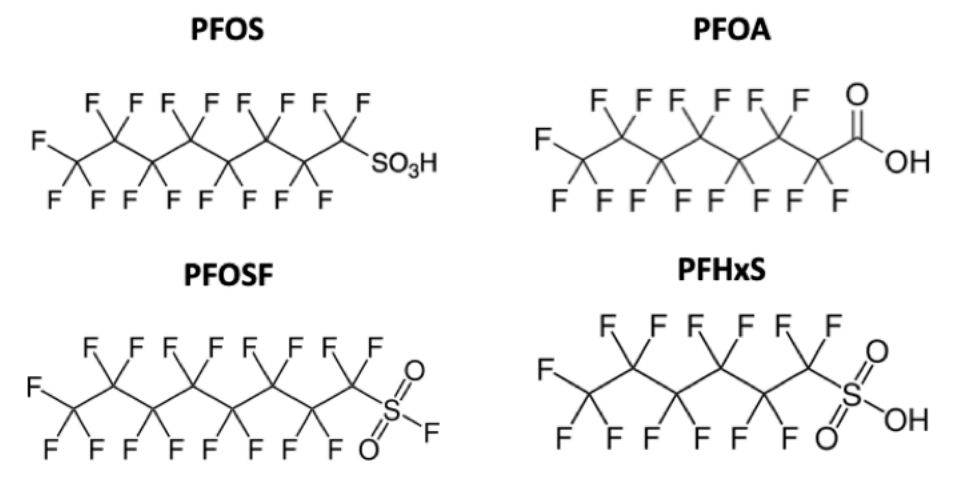

Figure 2: Chemical structures of PFOS, PFOA, PFOSF and PFHxS, all regulated by the Stockholm convention

c) Volatile and semi-volatile PFAS

However, volatile and semi-volatile PFAS are also widely used. This group includes fluorotelomer alcohols (FTOHs), perfluorooctane sulfonamides (PFOSAs), and perfluorooctane sulfonamidoethanols (PFOSEs) (Figure 3). These substances are used as paper coatings and performance chemicals in applications such as firefighting foams, insecticides, and water- and stain-resistant treatments for carpets, textiles, and leather. They are also found in paints, coatings, and adhesives [16]. Consequently, these compounds are present in many everyday household products, even though current regulations governing their use remain limited.

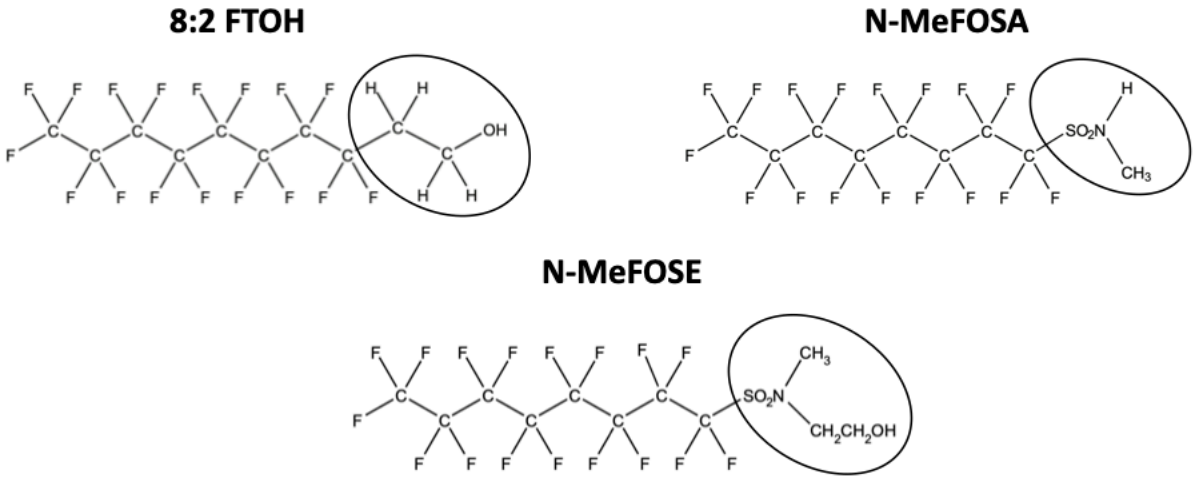

Figure 3: Chemical structures of 8 :2 FTOH, N-MeFOSA and N-MeFOSE

Several regulations are being implemented to phase out the use of PFASs. For example, Canada has proposed to designate PFASs as toxic substances, the European Chemicals Agency (ECHA) has suggested two options to ban certain PFASs, the REACH regulation aims to establish a universal restriction on PFASs based on the concept of essential uses [17,18]. However, these measures are progressing slowly due to the large number of PFASs, the lack of a clear definition of PFASs, the

incomplete understanding and knowledge of their properties, and the limited availability of less toxic alternatives [17,18].

In addition, it is important to analyse and regulate these volatiles PFAS because they can degrade via biotic (degradation by living organisms) and abiotic (degradation by non-biological factors) pathways to forms more toxic PFAS [19].

For instance, FTOHs are precursors of perfluoroalkyl carboxylic acids (PFCAs) (Figure 4), a class of compounds known for their high toxicity [19,20,21,22,23]. These substances exhibit a wide range of adverse effects, including reproductive and developmental toxicity, disruption of fatty acid metabolism and the endocrine system, as well as potential carcinogenicity [24]. Among the PFCAs, PFOA (Figure 2) and its salts are considered particularly hazardous and have been classified by the United States Environmental Protection Agency (USEPA) as likely human carcinogens [24].

Similarly, N-MeFOSAs and N-MeFOSEs act as precursors to perfluoroalkyl sulfonic acids (PFSAs) (Figure 4). These compounds exhibit toxicological profiles comparable to their precursors, although adverse effects may occur at lower exposure levels [25].

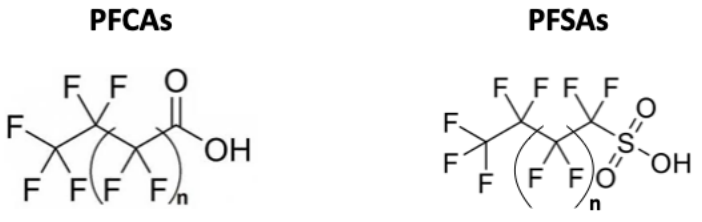

Figure 4: General chemical structures of PFCAs and PFSAs

2. Analytical techniques

a) Gas chromatography

As mentioned in Section 1.2, the most commonly used analytical technique for PFAS analysis is LC-MS. This method is highly sensitive and selective, making it particularly effective for the detection of PFASs. However, it is limited to the analysis of non-volatile PFASs [12].

The addition of gas chromatography-mass spectrometry (GC-MS) as a complementary technique may extend the analytical scope, as it enables the detection of semi-volatile and volatile compounds (this technique is further described in Section IV.A Analytical techniques). GC-MS also offers high sensitivity and selectivity and also allows for both non-target and suspect screening approaches, which, unlike targeted analyses, enables the identification of a larger number of compounds [13,26 ,27].

b) Ion mobility

Another separation dimension that can be incorporated is ion mobility spectrometry (IM) (this technique is further described in Section IV.C Analytical techniques). This technique, which separates ions based on their gas-phase size and shape, may enhance the separation of co-eluting compounds that are not resolved by chromatography, such as isobaric and isomeric species. It

also allows the determination of the collision cross section (CCS), which provides molecular-level structural information [27,28].

Ezaz Ahmed *et al.* were the first to apply ion mobility for the analysis of PFAS isomers using a differential mobility spectrometry-mass spectrometry (DMS-MS) system coupled with LC, demonstrating rapid separation of selected linear and branched PFASs [29]. Subsequently, Francesc Labad *et al.* separated a large number of polar PFASs using LC and traveling wave ion mobility spectrometry (TWIMS) instrument and determined their CCS values using TWIMS [30]. N. James *et al.* analyzed PFAS using LC–drift tube ion mobility spectrometry (DTIMS)-MS and investigated the correlation between mass and CCS [28]. However, these studies focused on non-volatile PFAS, as the analyses were performed using LC.

A study conducted by Amber MacNeil *et al.* analyzed less polar compounds, including PFAS, using a combined gas chromatography-cyclic ion mobility spectroscopy (GC-cIMS) system and demonstrated that this technique complements LC-based approaches [13]. Nevertheless, this remains one of the few studies involving GC-IM, highlighting the lack of information in the literature on PFAS analysis using GC-IM-MS instrumentation.

B. Objectives

This chapter has two main objectives.

The first objective focuses on developing a method for the analysis of three volatile PFASs: perfluorooctyl ethanol (8:2FTOH), *N*-methylperfluoro-1-octanesulfonamide (N-MeFOSA), and 2-(*N*-methylperfluoro-1-octanesulfonamido) ethanol (N-MeFOSE). This will require optimization of the GC parameters, the ionization source (APCI), and the TIMS settings.

The second objective will also be to identify and characterize the fragmentation patterns of these three PFAS compounds.

C. Materials and Methods

1. Chemical standards

Perfluorooctyl ethanol, *N*-methylperfluoro-1-octanesulfonamide and 2-(*N*-methylperfluoro-1-octanesulfonamido) ethanol standards were purchased from Wellington (Ontario, Canada). They were diluted in hexane to provide two solutions of 100 pg/μl and 10 pg/μl.

All solvents used were of the highest purity, suitable for the analysis of trace contaminants (Biosolve, Dieuze, France).

2. GC-APCI-TIMS-TOFMS instrument

Measurements were performed on a commercial timsTOF Flex mass spectrometer (Bruker, Bremen) and timsTOF Pro2 mass spectrometer (Bruker, Bremen) both equipped with a Scion 456-

GC connected to an atmospheric pressure chemical ionization (APCI) source for sample introduction and ionization (GC- APCI II, Bruker, Bremen).

The standards were injected automatically in spitless mode (injection temperature 250°C, 1 µL). The GC column was a low polarity Rxi-5Sil MS column (30 m × 0.25 mm × 0.25 µm, Restek). Helium (grade 6.0, 99,9%, Air Liquide, Belgium) was used as the carrier gas. Ion mobility separations were performed by trapped ion mobility (TIMS).

3. Optimization procedure

A classical optimization consists of varying a single parameter at a time, from its minimum to maximum value, while keeping all other parameters constant. Consequently, for each value of the investigated parameter, a separate experimental run is performed. This approach allows for the identification of the optimal value of an individual parameter but does not account for possible interactions between variables.

The concept of Design of Experiments (DOE) is "a systematic approach to studying the effects of multiple input factors (e.g., speed, temperature, or supplier) on process outputs (e.g., yield, impurity level, or cost)" [31]. The main advantage of this methodology lies in its ability to simultaneously evaluate the influence of several factors in order to optimize a process [32,33]. The overall experimental responses are then used to construct a mathematical model describing the relationship between factors and responses. This model defines the design space, which is "the multidimensional combination and interaction of input variables (e.g., material attributes) and process parameters that have been demonstrated to provide assurance of quality" [32]. Another significant advantage of DOE, compared to classical optimization, is its ability to reveal interactions and interdependencies among parameters.

In this work, the combination of classical optimization and DOE approach was used to optimize the parameters.

4. Methods

a) Data treatment

For GC-timsMS analysis, data were processed using DataAnalysis software (Bruker, version 5.3). For the first DOE, peak integration was based on the intensity of the gas chromatography peaks. For the second and third DOEs, peak integration was based on the area of the ion mobility peaks. Internal recalibration of mass-to-charge ratio (m/z) and ion mobility was performed using siloxanes originating from column bleed prior to data acquisition and data processing.

b) Design of Experiments

DOE was performed using the statistical software JMP (version 19.0). The experimental designs were constructed based on response surface methodology (RSM). For the first DOE, a central composite design (CCD) was selected to evaluate the significance of individual factors and their interactions, as this design allows exploration of factor behaviour beyond the experimental domain. However, experimental runs conducted at parameter values outside the defined domain

resulted in outliers, as these conditions fell outside the valid region of the response surface. Consequently, for the second and third DOE, a Box-Behnken design (BBD) was employed, as this design evaluates intermediate parameter levels without including out-of-domain values.

D. Results and discussions

A solution containing three standards volatile PFAS was used for the optimization of the GC-APCI-TIMS-TOFMS method (see Figure 3). Before optimization, a preliminary test was performed using a 100 pg/µL solution injected into the GC-APCI-MS instrument, with GC parameters selected from the literature [29,30] and APGC parameters based on previous optimization for brominated and chlorinated compounds (see Table 1), as PFAS had never been injected by GC before.

Parameters:	**GC**				
Injector	**Flow of gas (He)**	**Injected volume**	**Column**		
T = 250 °C	1 ml/min	1 µl splitless	T initial = 50°C → 300 °C with 10°C/min => 35 min run	Transfer line T = 250 °C	Head source T = 225 °C
Parameters:	**APCI**				
End plate offset	**Capillary**	**Corona**	**Nebulizer**	**Dry gas**	**Dry gas temperature**
500 V	4500 V	5000 nA	2.4 Bar	1.5 L/min	175°C

Table 1: GC parameters selected from the literature [29,30] and APCI parameters optimized for brominated and chlorinated compounds

This preliminary test was conclusive, as the extracted ion chromatograms (EICs) of the $[M+H]^+$ species showed significant signal intensities (see Figure 5).

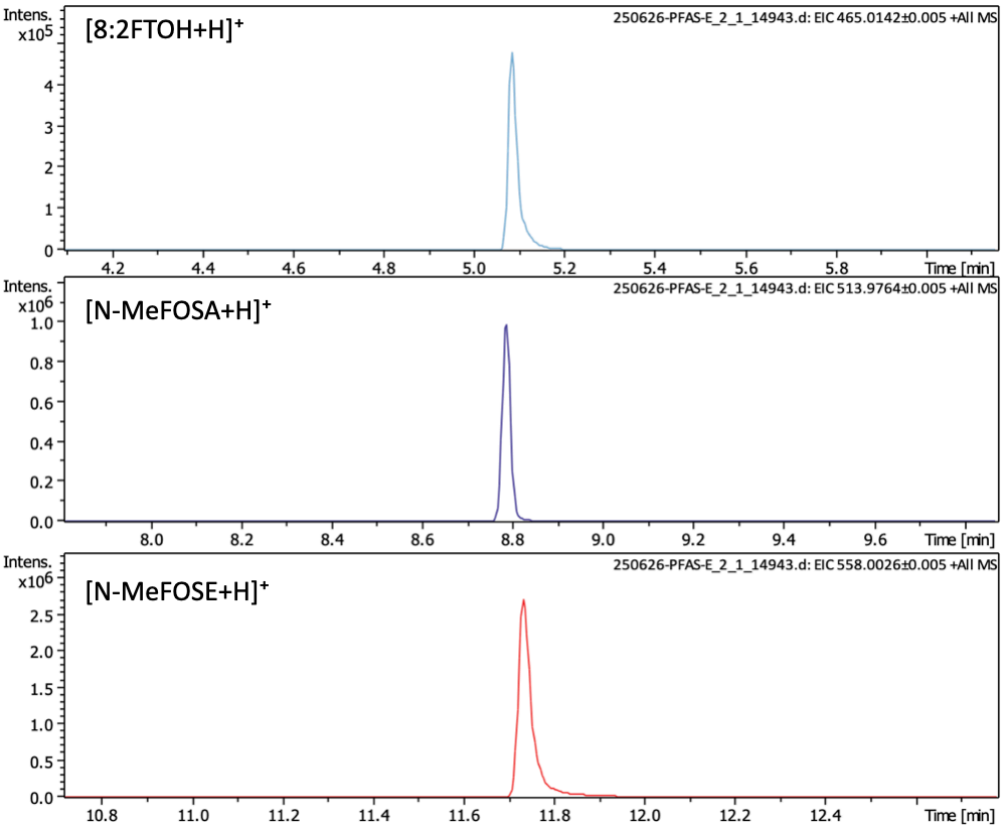

Figure 5: EICs of 8:2FTOH, N-MeFOSA and N-MeFOSE protonated for the100 pg/µl solution

For further optimization, two modifications were made. First, the concentration of the solution was reduced by a factor of 10 ([C] = 10 pg/µL). Second, the final oven temperature of the GC program was decreased from 300 °C to 200 °C, which reduced the total run time from 35 min to 21 min.

The development of the method was carried out in several steps due to the large number of parameters requiring optimization.

1. Optimization of source parameters

First, the source parameters were optimized in the GC-APCI-MS system using a DOE approach. Prior to this, a classical one-factor-at-a-time optimization was performed for source parameters (end plate offset, capillary voltage, corona current, nebulizer pressure, dry gas flow, dry gas temperature) the head source temperature, and the transfer line temperature (see Figure 2, section IV.B Analytical techniques). This allowed identification of the key parameters influencing the signal of the three standards and the relevant value ranges to be used for the DOE.

a) Classical Optimization

For this classical optimization, each parameter was varied individually from its minimum to intermediate and maximum values within the instrument-permitted range (see Table 2).

Parameters	Range	Min / Int / Max
End plate offset (V)	[0; 2500]	200 / 1000 / 2000
Capillary voltage (V)	[0; 6000]	1000 / 3000 / 5000
Corona current (nA)	[0; 40 000]	1000 / 3000 / 5000 / 10000 / 15000
Nebulizer (bar)	[0; 5.5]	1 / 3 / 5
Dry gas (l/min)	[0; 12]	2 / 6 / 10
Dry gas T (°C)	[0; 350]	150 / 225 / 300
Head source T (°C)	[0; 300]	200 / 250 / 300
Transfer line T (°C)	[0; 300]	200 / 250 / 300

Table 2: Parameters optimized during the classical optimization with their instrument-permitted range and the minimum, intermediary and maximum tested values

The results of this preliminary optimization, based on the integrated peak intensity of PFAS in their EICs, revealed that three parameters had a major influence on PFAS signal intensity: nebulizer, corona current, and dry gas temperature (see Figure 6). Two additional parameters, capillary voltage and transfer line temperature, showed smaller but noticeable effects.

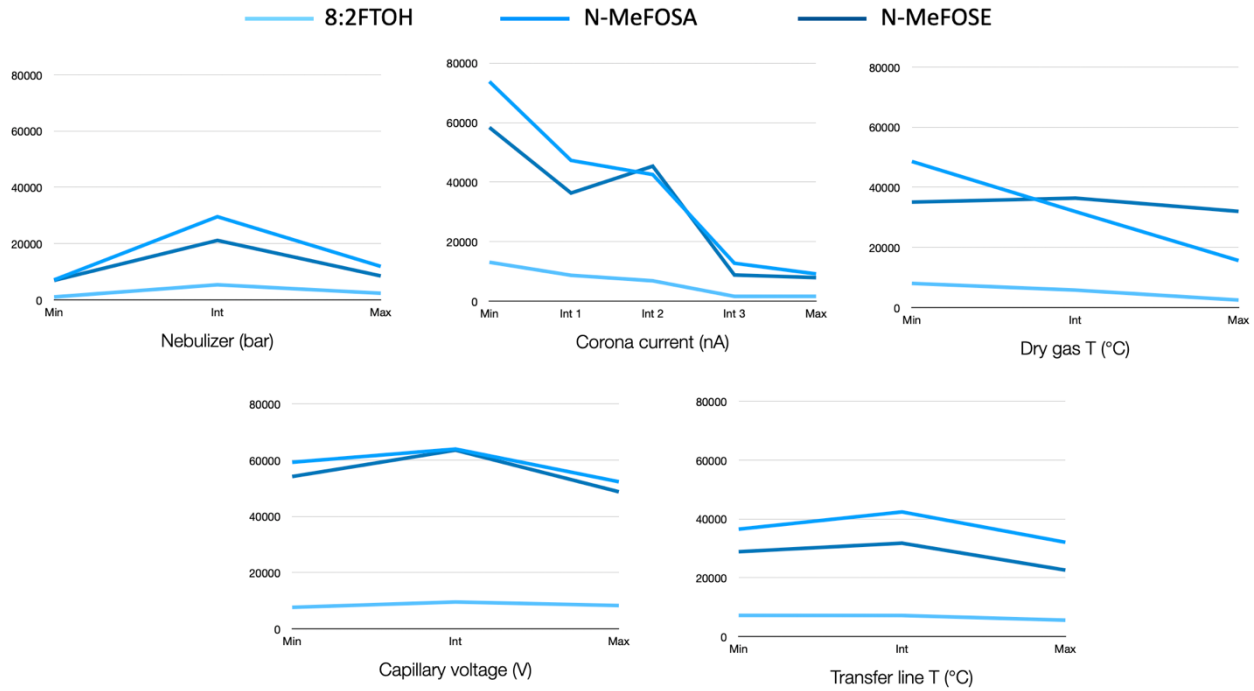

Figure 6: Intensity variation of 8:2FTOH, N-MeFOSA and N-MeFOSE during the classical optimization of nebulizer, corona current, dry gas T, capillary voltage and transfer line T

End plate offset, dry gas and head source temperature parameters were produced relatively constant signal intensities (see Figure 7). Hence, these parameters were not further included in the optimization and the values providing the highest consistent response were selected: end plate offset of 200 V, a dry gas of 1,5 l/min and a head source temperature of 250 °C.

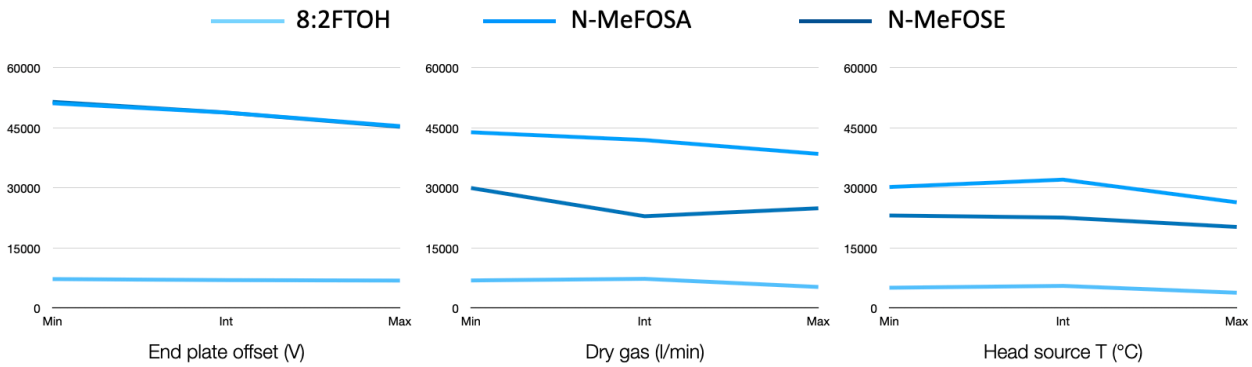

Figure 7: Intensity variation of 8:2FTOH, N-MeFOSA and N-MeFOSE during the classical optimization of end plate offset (where N-MeFOSA and N-MeFOSE lines overlap perfectly), dry gas and head source T

During the optimization, it was observed that the signal of 8:2FTOH was lower than that of N-MeFOSA and N-MeFOSE. Additionally, peak tailing was observed for all three standards (see Figure 8). To address this issue, approximately 25 cm of the column head was trimmed, the liner was cleaned with n-hexane and MeOH, and the initial oven temperature was decreased from 70 °C to 60 °C (it was increased to reduce run time but caused greater tailing).

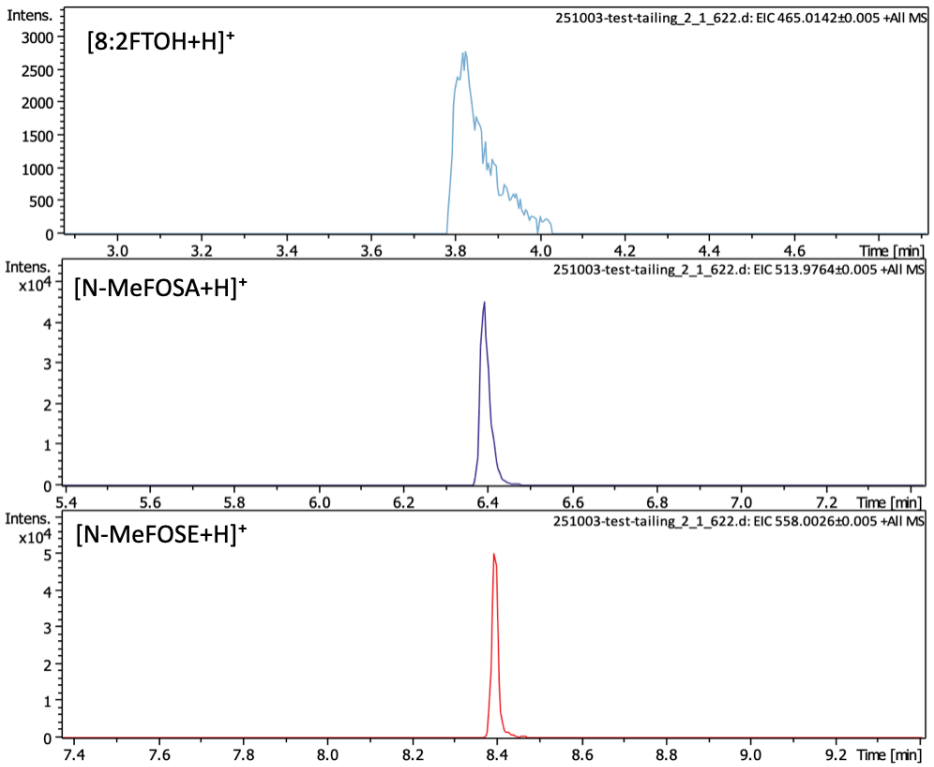

Figure 8: EICs of 8:2FTOH, N-MeFOSA, N-MeFOSE (initial GC condictions)

After these modifications, the EICs shown in Figure 9 were obtained. Although tailing was reduced, further improvement could potentially be achieved by using a more polar column (e.g., DB-17), applying programmed temperature vaporization (PTV) injection to reduce injector

temperature, or testing an alternative disactivated liner, as the current liner contains glass, Topaz, Frit with Top Taper Inlet Liner, which can cause adsorption. PFAS tend to adsorb strongly to glass surfaces, producing tailing effects [34].

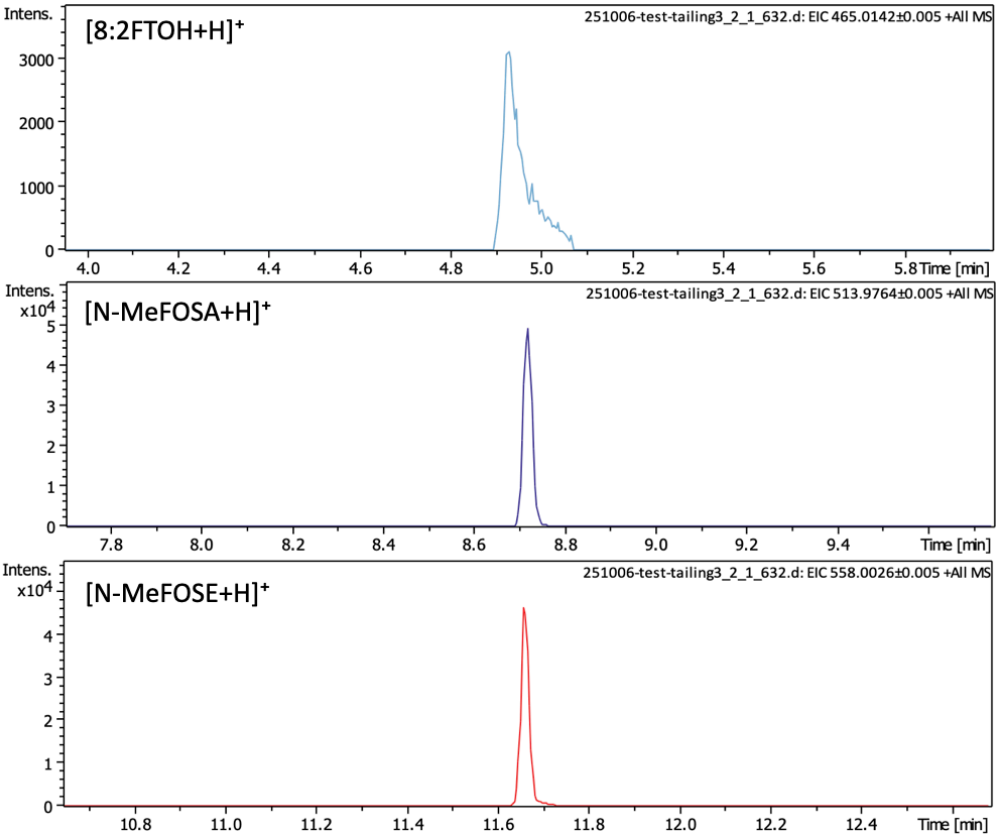

Figure 9: EICs of 8:2 FTOH, N-MeFOSA and N-MeFOSE after modification

The peak asymmetry of the PFAS was not considered problematic. The highest asymmetry factor was observed for 8:2 FTOH (≈1.8), measured at 50% of the peak height, and remained below the acceptable limit. Although this limit is not defined for PFAS, it is defined for dioxins in the European Union Reference Laboratory (EURL) guidance document for halogenated POPs [35]. For this reason, and to avoid unnecessary time expenditure, no further optimization of peak tailing was carried out.

b) First DOE

The DOE was then performed using the nebulizer pressure, dry gas temperature, corona current, capillary voltage, and transfer line temperature as factors within their defined domains based on the classical optimization (see Table 3), applying a CCD to evaluate the significance of each factor and their interactions. This design also allows exploration of parameter behaviour outside the experimental domain.

Parameters (unit)	Domain
Nebulizer pressure (bar)	[2,5;3,5]
Dry gas temperature (°C)	[200;250]
Corona current (nA)	[500;1500]
Capillary voltage (V)	[2500;3500]
Transfer line temperature (°C)	[225;275]

Table 3: Optimized parameters during DOE with the domain

The design consisted of 32 runs, which were not conducted in random order (see Table S1) because adjustments to the transfer line temperature must be made manually. The responses were based on the intensity of each standard integrated in the EICs.

Studentized residuals are a statistical diagnostic used in regression analysis. A studentized residual is calculated by dividing the residual (defined as the difference between the observed value and the predicted by the model) by an estimate of its standard deviation computed with the corresponding observation excluded from the model fitting. Studentized residuals are commonly used to detect outliers [36].

Studentized residuals showed that the model fit was acceptable within the 99 % confidence interval for all three compounds (see Figure 10). There is an exception in the studentized residuals of N-MeFOSE where an experiment is outside 99 % confidence. It corresponds to an experiment with a corona current value outside the domain specified for the DOE. This parameter leaves the aera of the response curve. Consequently, this design space was excluded in subsequent DOE experiments.

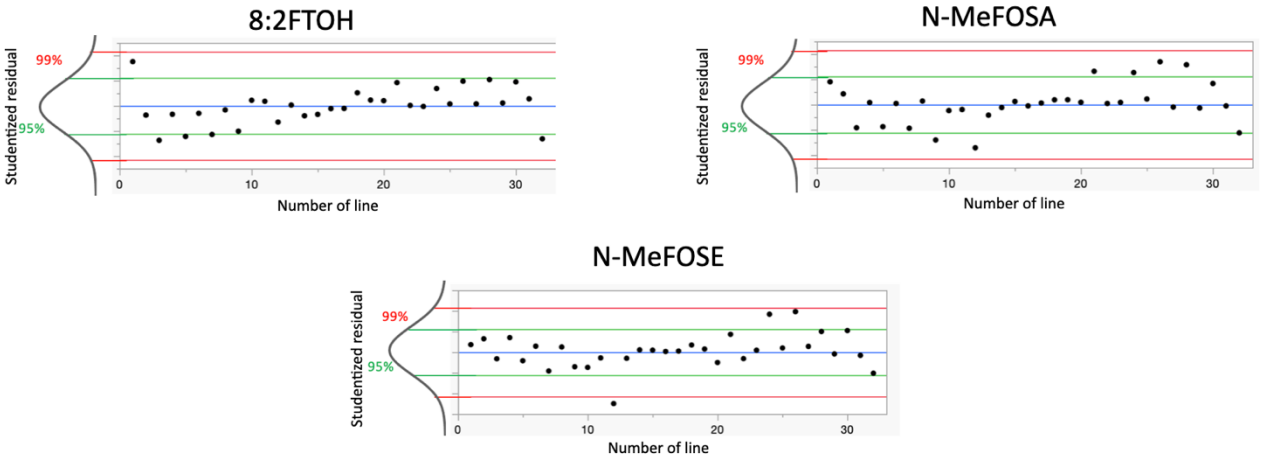

Figure 10: The studentized residuals for 8:2FTOH, N-MeFOSA and N-MeFOSE of the first DOE

The summary of effects ranks the main factors and their interactions in descending order according to their $-\log_{10}$(p-value), referred to as the *logWorth*. The p-value is calculated from the appropriate statistical distribution and represents the probability of observing a result as extreme as, or more extreme than, the one obtained under the null hypothesis (i.e., the absence of an effect) [37,38]. A small p-value indicates that the observed effect is unlikely to be due to random

chance alone and therefore provides evidence against the null hypothesis [37,38]. The logWorth transformation is used to improve interpretability and comparability among effects, with higher logWorth values corresponding to more statistically significant effects [39].

The summary of effects in Figure 11 indicates that nebulizer pressure and transfer line temperature factors had the strongest influence on signal intensity, followed by corona current.

Source	Logworth	P-value
Nebulizer(2,5,3,5)	4,872	0,00001
Transfer line T (°C)(225,275)	2,470	0,00339
Corona current(500,1500)	1,449	0,03555
Nebulizer*Nebulizer	1,373	0,04240
Corona current*Nebulizer	1,360	0,04360
Dry gas T (°C)*Dry gas T (°C)	1,234	0,05829
Capillary volatge (V)(2500,3500)	1,142	0,07207
Nebulizer*Capillary volatge (V)	0,961	0,10929
Capillary volatge (V)*Capillary volatge (V)	0,702	0,19883
Dry gas T (°C)(200,250)	0,664	0,21687
Transfer line T (°C)*Transfer line T (°C)	0,620	0,24005
Corona current*Corona current	0,566	0,27152
Corona current*Dry gas T (°C)	0,526	0,29816
Capillary volatge (V)*Transfer line T (°C)	0,487	0,32574
Dry gas T (°C)*Capillary volatge (V)	0,475	0,33477
Nebulizer*Dry gas T (°C)	0,446	0,35801
Dry gas T (°C)*Transfer line T (°C)	0,370	0,42634
Corona current*Transfer line T (°C)	0,366	0,43041
Nebulizer*Transfer line T (°C)	0,240	0,57533
Corona current*Capillary volatge (V)	0,214	0,61040

Figure 11: Summary of effects for the intensity of all PFAS of the first DOE

The response surface model for the three compounds showed that maximum signal was achieved when the transfer line temperature was set to its highest value and the nebulizer pressure to its lowest (see Figure 12).

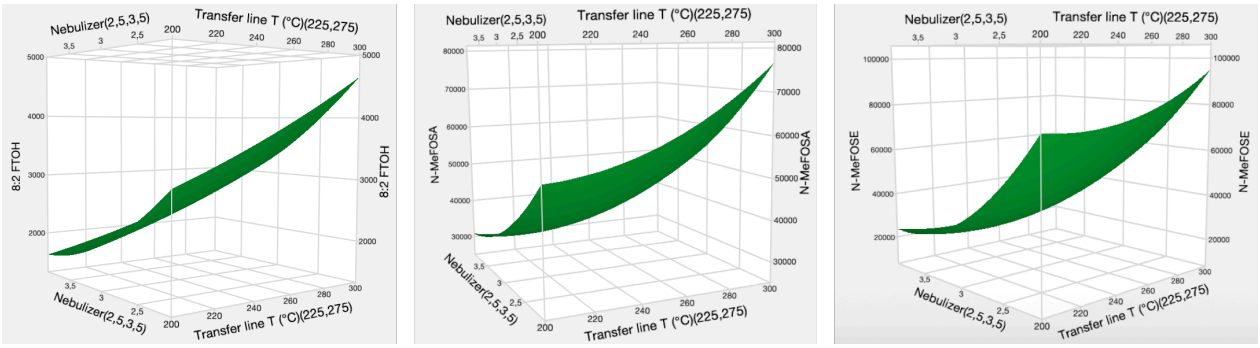

Figure 12: Response surface model for intensity of each 8:2FTOH, N-MeFOSA and N-MeFOSE vs nebulizer and transfer line T

The optimal source parameters were: corona current 1910 nA, nebulizer pressure 2.1 bar, dry gas temperature 180 °C, capillary voltage 2090 V, and transfer line temperature 300 °C. However, the dry gas temperature was increased to 250 °C to prevent condensation of compounds with higher boiling points. Increasing the dry gas temperature did not significantly affect signal intensity, as this parameter was not among the main factors influencing the response, as shown in the summary of effects in Figure 11.

After applying these optimal parameters, the signal of 8:2FTOH remained lower than that of N-MeFOSA and N-MeFOSE (see Figure 13). Therefore, a second optimisation was performed on corona current and capillary voltage to improve 8:2FTOH sensitivity. Firstly, two extreme corona current values (1000 nA and 5000 nA) were tested. The results, summarized in plot and normalized relative to the experiment that produced the highest 8:2FTOH signal, indicated that 8:2FTOH intensity was greatest at 1000 nA (see Figure 14). Secondly, four capillary voltages (1000 V, 2090 V, 3000 V, and 4000 V) were evaluated. The results, combined in plot using the same normalization method, showed that 8:2FTOH signal intensity was highest at the lowest capillary voltage (see Figure 14).

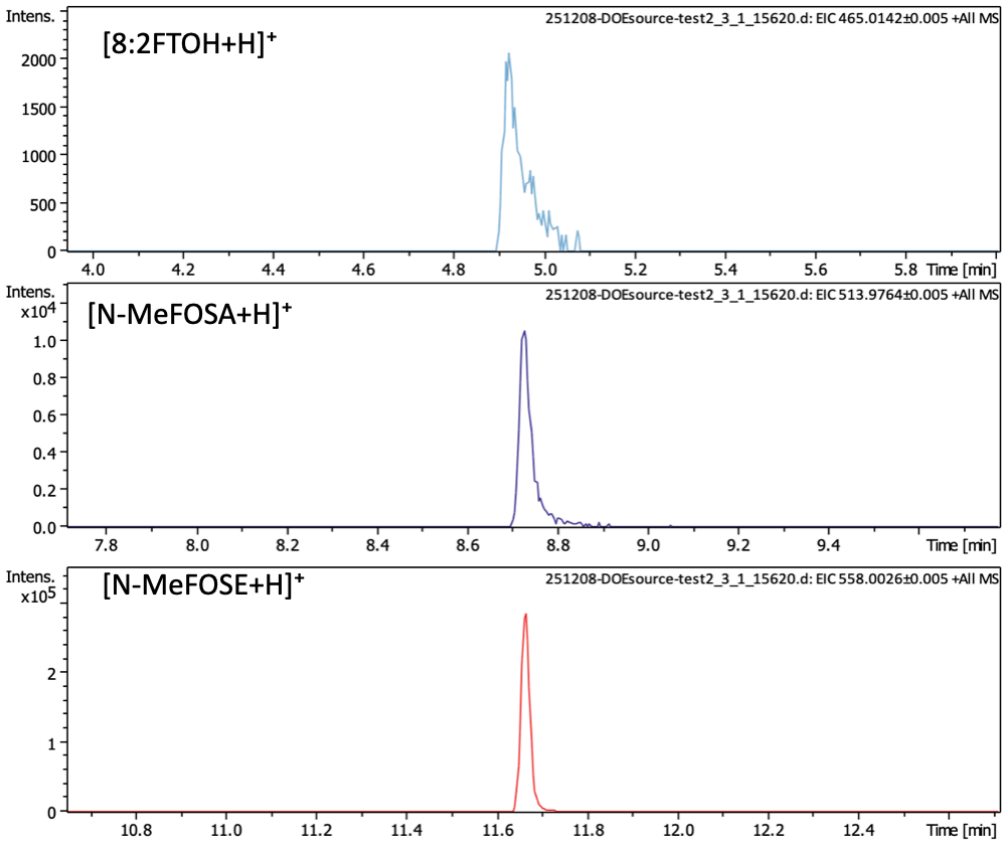

Figure 13: EICs of 8:2FTOH, N-MeFOSA and N-MeFOSE generated with the optimized parameters of source

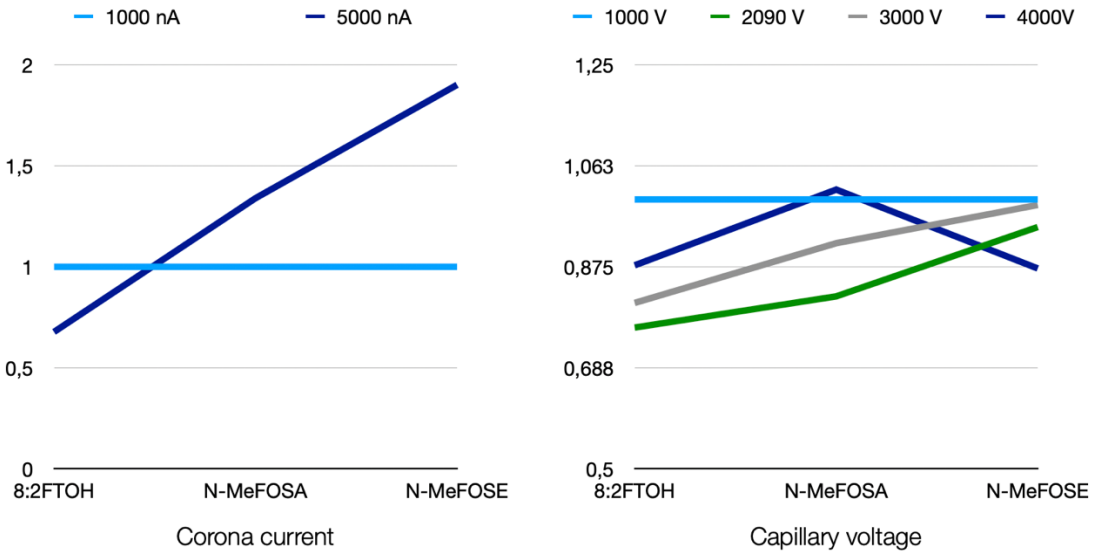

Figure 14: Plots normalized relative to the experiment that produced the highest 8:2FTOH signal for the corona current optimization (left) and capillary voltage optimization (right)

Consequently, a time segment was added to the method using the optimal parameters specifically for 8:2FTOH (see Table 4), with the time range defined according to the retention time of 8:2 FTOH. In addition, the capillary voltage optimization plot in Figure 14 shows that the signals of N-MeFOSA and N-MeFOSE are maximized at a capillary voltage of 1000 V. Therefore, this value was incorporated into the optimized APCI method (see Table 4).

Parameters	**APCI**					
End plate offset	**Capillary**	**Corona**	**Nebulizer pressure**	**Dry gas**	**Dry gas T**	**Time range**
200 V	1000V	1000 nA	2.1 Bar	1.5 L/min	250°C	[0;5,5]
End plate offset	**Capillary**	**Corona**	**Nebulizer pressure**	**Dry gas**	**Dry gas T**	**Time range**
200 V	1000V	1910 nA	2.1 Bar	1.5 L/min	250°C	[5,5;20]

Table 4: Optimized APCI parameters for 8:2FTOH, N-MeFOSA and N-MeFOSE

2. Optimization of trapped ion mobility mass spectrometry and time-of-flight parameters

Following optimization of the source parameters, the TIMS and time-of-flight (TOF) parameters were optimized. The same approach used previously was applied here: a classical one-factor-at-a-time optimization was performed prior to a DOE. Thirteen parameters were evaluated (see in Figure 15):

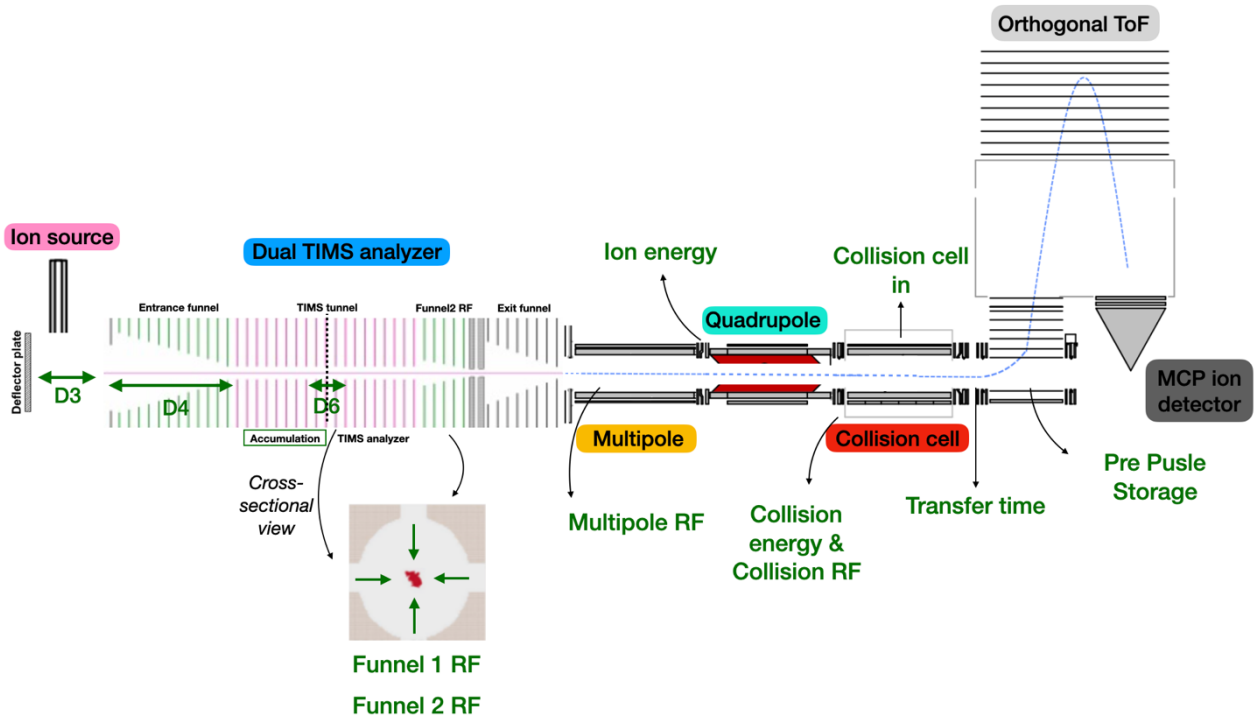

Figure 15: Schematic representation of timsTOF instrument with the optimized parameters in the DOEs [40]

Funnel1 and **Funnel2**, **Multipole** and **Collision RF** corresponding to the radial radio-frequency (RF) amplitudes applied by the electrodes to centralize the beam of ions and prevent them from hitting the electrodes
Transfer time, the time ions spend travelling between the collision cell and the TOF;
Pre-Pulse Storage, the delay before ions are pushed into the TOF;
Collision Energy (Collision E) and **Ion Energy (Ion E)**, corresponding to the potential differences between the quadrupole and collision cell, and between the multipole and quadrupole, respectively;
Δ3, Δ4, and Δ6, representing the potential differences between the deflector plate and the TIMS entrance (Δ3), at the entrance of Funnel1 (Δ4), and between the accumulation and analysis regions of the TIMS (Δ6);
Collision Cell In, an axial electric field gradient applied within the collision cell to accelerate ion transmission;
Accumulation time, the time during which ions are stored in the accumulation region of the TIMS before being analysed.

a) Classical optimization

Each parameter was tested individually at its minimum, intermediate, and maximum instrument-allowed values (see Table 5).

Parameters	Range	Min / Int / Max
Funnel1 RF (Vpp)	[0;500]	100 / 300 / 500
Funnel2 RF (Vpp)	[0;600]	100 / 350 / 600
Multipole RF (Vpp)	[0;1200]	200 / 700 / 1200
Collision RF (Vpp)	[0;4000]	500 / 2250 / 4000
Transfer time (μs)	[0;3000]	30 / 50 / 100 / 150
Pre Pulse Storage (μs)	[0;3000]	2 / 9 / 16
Collision E (eV)	[0;200]	2 / 8 / 14
Ion E (eV)	[0;200]	2 / 8 / 14
Δ3 (V)	[0;600]	20 / 100 / 200 / 300
Δ4 (V)	[0;600]	20 / 100 / 200 / 300
Δ6 (V)	[0;600]	20 / 100 / 200
Collision Cell In (V)	[0;300]	50 / 150 / 300
Accumulation time (ms)	[0;250]	82.5 / 165 / 250

Table 5: TIMS and TOF parameters optimized during the classical optimization with their instrument-permitted range and the minimum, intermediary and maximum tested values

The preliminary optimization, based on integrated PFAS peak areas obtained from mobility-filtered EICs, revealed that three parameters, Funnel 2 RF, multipole RF and Δ4, exhibited relatively constant responses across the investigated ranges (Figure 16). Consequently, these parameters were excluded from further optimization and fixed values of 200 Vpp, 300 Vpp, and 20 V were applied, respectively.

In addition, the accumulation time was fixed at an intermediate value. As the response plot in Figure 16 did not indicate signal saturation, this intermediate setting was selected to avoid potential saturation while maintaining sufficient sensitivity. This parameter will be further optimized in the final optimization step.

Optimizing the remaining ten parameters simultaneously within a single design of experiments approach would have been overly complex. Therefore, the optimization strategy was divided into two separate DOE studies, hereafter referred to as the “second DOE” and the “third DOE.” The second DOE included parameters that were interdependent, whereas the third DOE focused on parameters that were independent of one another.

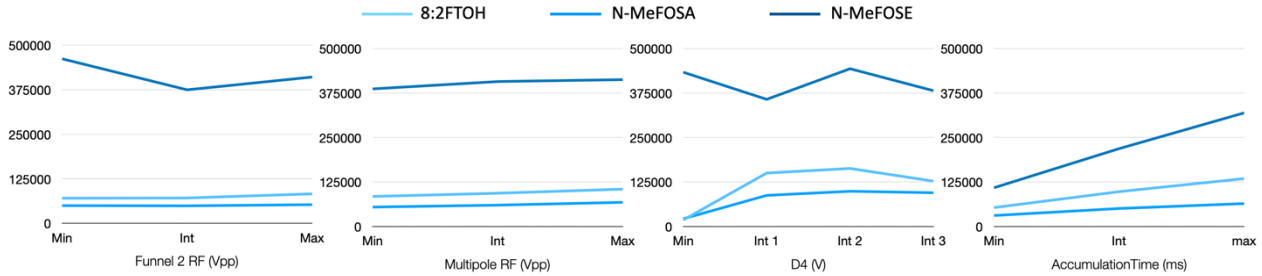

Figure 16: Area variation of 8:2FTOH, N-MeFOSA and N-MeFOSE during the classical optimization of Funnel2 RF, Multipole RF, Δ4 and Accumulation time

b) Second DOE

For the second DOE, the factors were Funnel1 RF, collision RF, transfer time, Δ3, and Δ6 within their defined domains based on the classical optimization (see Table 6). A BBD was selected instead of a CCD, like in first DOE, because values outside the defined domain had previously produced no detectable PFAS signal, as demonstrated during the classical optimisation. Furthermore, BBD evaluates intermediate parameter levels rather than only extreme values, making it more suitable for this experimental domain.

Parameters (unit)	Domain
Funnel1 RF (Vpp)	[100;450]
Collision RF (Vpp)	[1000;3000]
Transfer time (μs)	[40;70]
Δ3 (V)	[150;250]
Δ6 (V)	[50;150]

Table 6: Optimized parameters during the second DOE with the domain

The design involved 46 runs random but instead 54 runs were performed because replicates were added to enhance the quality of the design (see Table S2). The responses were based on the area of each standard integrated in extracted ion mobilograms (EIMs) and on the shape of the peak in mobility, the responses were also based on the IM power resolution (Rp) the weight of the Rp was higher than area.

The studentized residuals indicated that the model was acceptable within the 99% confidence interval for all three compounds (see Figure 17).

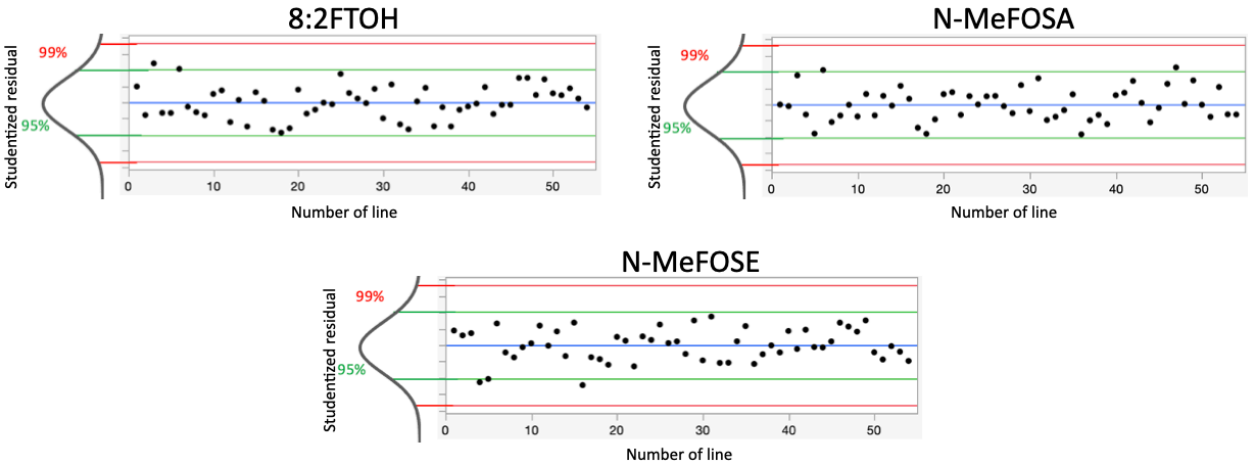

Figure 17: The studentized residuals for 8:2FTOH, N-MeFOSA and N-MeFOSE of the second DOE

The summary of effects in Figure 18 indicates that no single parameter has a dominant influence on the compound signal; instead, the interactions between parameters contribute most significantly. This suggests that the parameters are interdependent and therefore must be optimized simultaneously rather than individually.

Source	Logworth	P-value
Transfert Time*D3	1,475	0,03349
Funnel1RF*Funnel1RF	0,984	0,10379
Funnel1RF*D3	0,934	0,11635
Collision RF*Collision RF	0,689	0,20451
Collision RF*D3	0,680	0,20913
Collision RF*D6	0,563	0,27328
D3*D6	0,499	0,31665
Collision RF(1000,3000)	0,496	0,31881
Transfert Time(40,70)	0,446	0,35788
D6(50,150)	0,427	0,37387
Transfert Time*Transfert Time	0,407	0,39189
Transfert Time*D6	0,397	0,40112
Funnel1RF*Transfert Time	0,382	0,41486
Funnel1RF*Collision RF	0,289	0,51430
Funnel1RF*D6	0,285	0,51832
D6*D6	0,278	0,52693
Funnel1RF(100,450)	0,226	0,59480
D3*D3	0,202	0,62764
Collision RF*Transfert Time	0,158	0,69544
D3(150,250)	0,089	0,81502

Figure 18: Summary of effects for the area integrated in EIMs of all PFAS of the second DOE

The initially optimal parameters were a Funnel 1 RF of 100 Vpp, a collision RF of 1000 Vpp, a transfer time of 40 µs, and Δ3 and Δ6 set to 150 V. These parameters were tested, however, the resulting extracted ion mobilograms (EIMs) (see Figure 19) exhibited pronounced tailing. This effect was attributed to the low Funnel 1 RF value. When the Funnel 1 RF is insufficient, ions could be not adequately confined radially and can be affected by the parabolic gas velocity profile within the TIMS cell, leading to peak tailing [40, p85-87]. After additional adjustments, the parameters listed in Table 7 yielded acceptable mobility peak shapes for all compounds.

Nevertheless, the remaining tailing and the large N-MeFOSA peak have been further investigated and is discussed later (see in section 3) (see Figure 20).

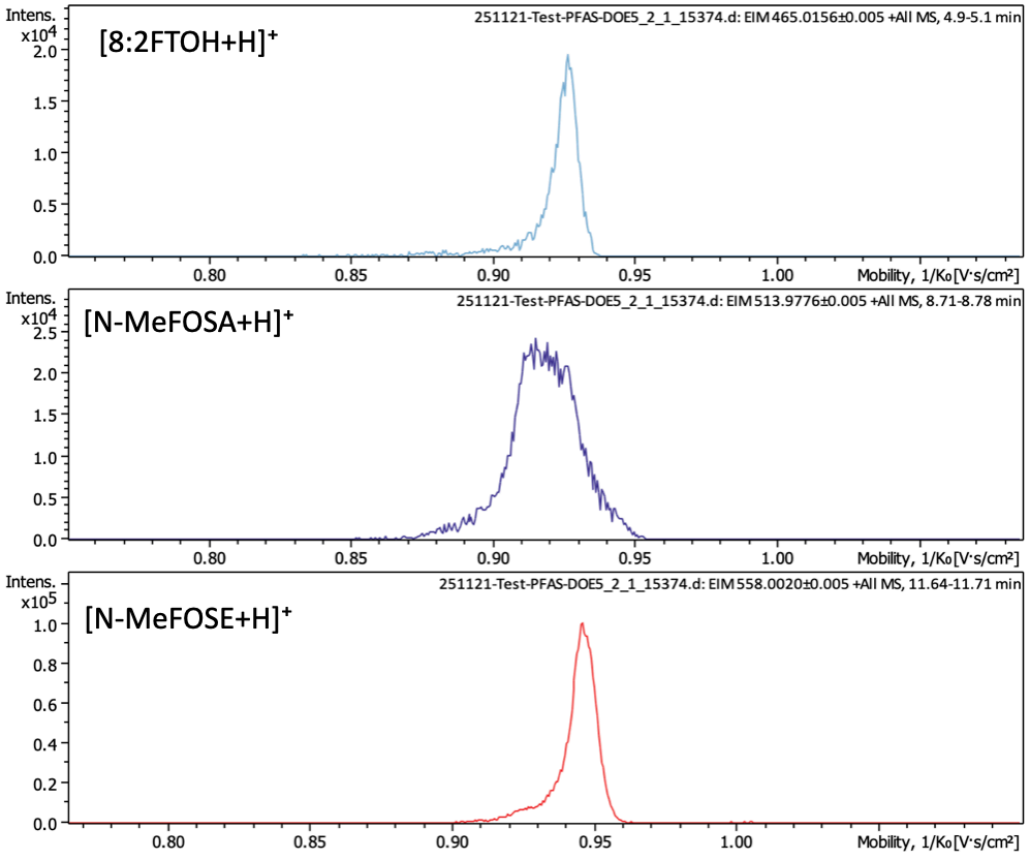

Figure 19: EIMs of 8:2FTOH, N-MeFOSA and N-MeFOSE generated with the optimized parameters determined by the second DOE

Funnel1 RF	Collision RF	Transfer time	Δ3	Δ6
255 Vpp	1000 Vpp	55 µs	150 V	150 V

Table 7 : Optimized parameters for 8:2FTOH, N-MeFOSA and N-MeFOSE

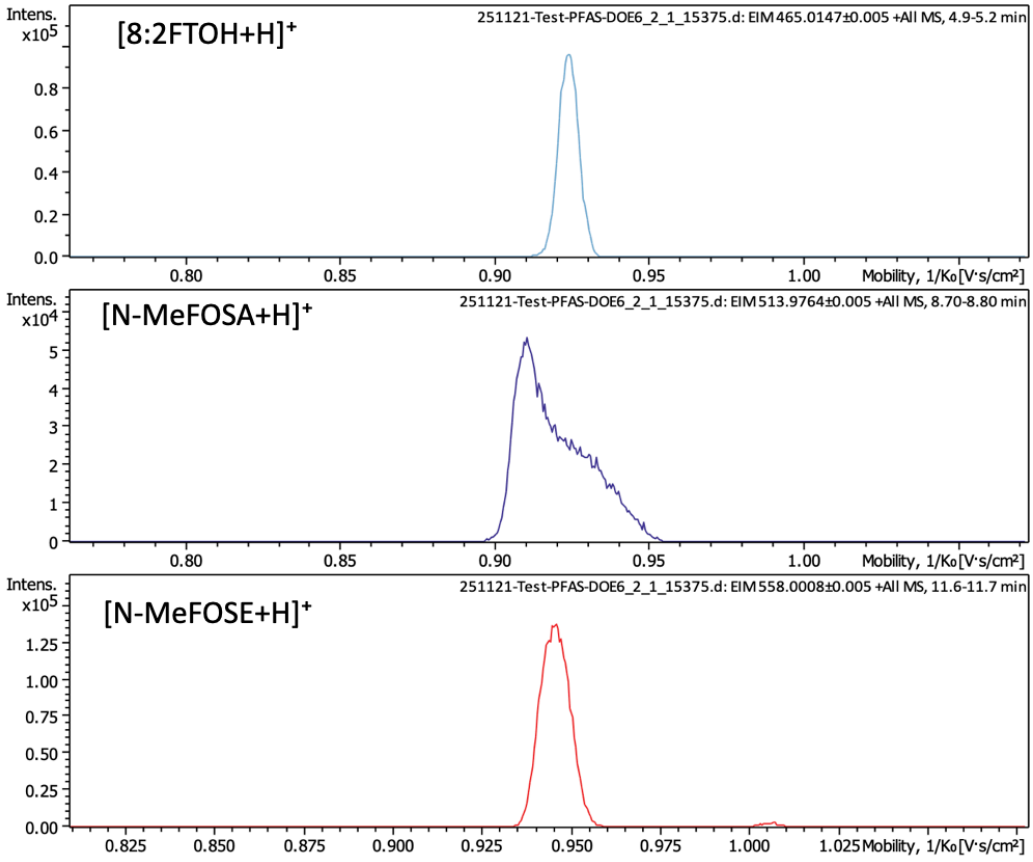

Figure 20: EIMs of 82FTOH, N-MeFOSA and N-MeFOSE generated with the optimized parameters based on additional adjustment

The response surface model (see Figure 21) shows that although Rp was more heavily weighted, the PFAS peak area remained most sensitive to intermediate values of Transfer Time and Funnel1 RF.

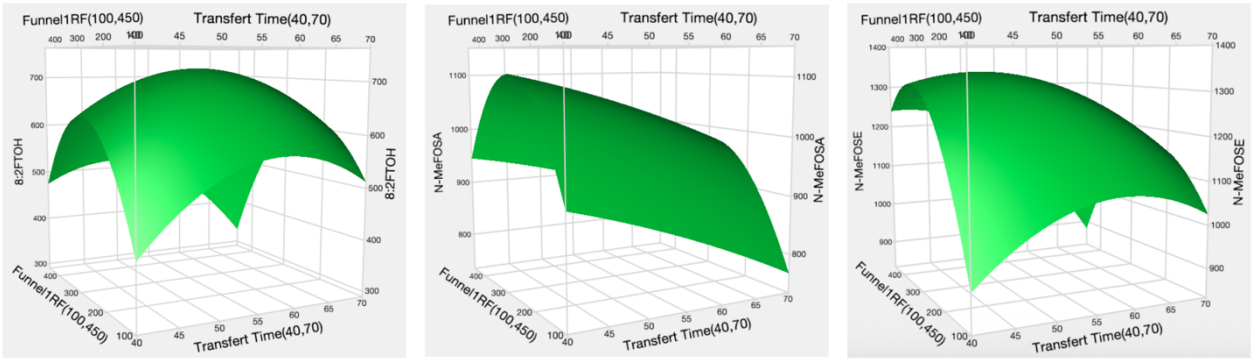

Figure 21: Response surface model for areas of each 8:2FTOH, N-MeFOSA and N-MeFOSE vs Funnel1 RF and transfer Time

c) Third DOE

The third DOE included Pre-Pulse Storage, Ion Energy (Ion E), and Collision Cell In as factors within their defined domains based on the classical optimization (see Table 8), and was also performed

using a BBD. This design consisted of 15 randomised runs (see Table S3). The responses evaluated were the same as those used in the second DOE.

Parameters	Domain
Pre pulse storage (μs)	[10;18]
Ion E (eV)	[6;10]
Collision Cell In (Vpp)	[100;200]

Table 8: Optimized parameters during the third DOE with their domain

The studentized residuals again indicated that the model fit within the 95% confidence interval (see Figure 22).

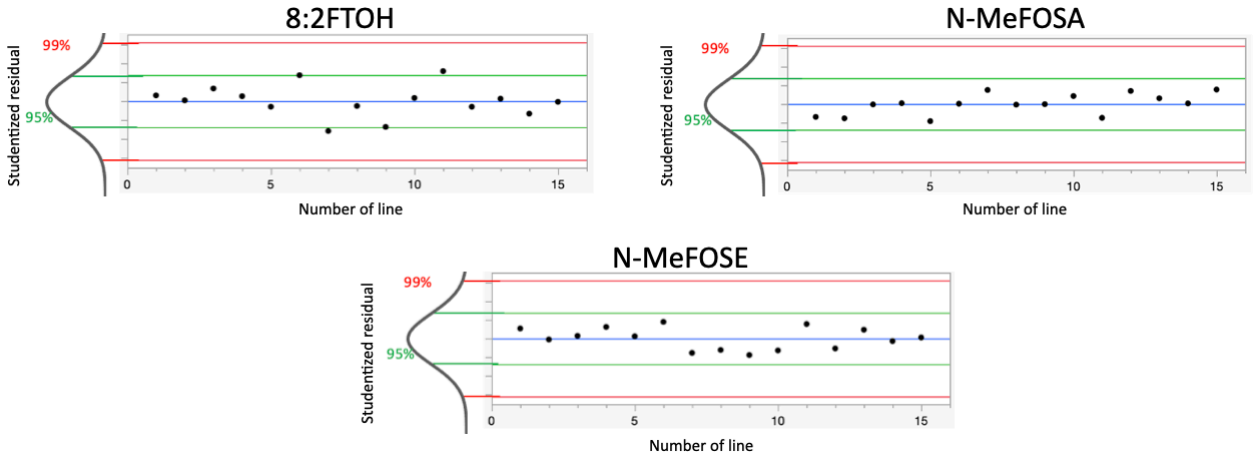

Figure 22: The studentized residuals for 8:2FTOH, N-MeFOSA and N-MeFOSE of the third DOE

The summary of effects in Figure 23 indicates these parameters are independent because it is the parameters or the interaction with themselves that impact the most the area of compounds.

Source	Logworth	P-value
PrePulseStorage*PrePulseStorage	4,918	0,00001
Ion E(6,10)	3,355	0,00044
CollisionCellIn(100,200)	2,935	0,00116
PrePulseStorage(10,18)	2,545	0,00285
CollisionCellIn*CollisionCellIn	2,185	0,00652
Ion E*Ion E	1,475	0,03351
Ion E*CollisionCellIn	0,833	0,14686
PrePulseStorage*Ion E	0,505	0,31250
PrePulseStorage*CollisionCellIn	0,386	0,41146

Figure 23: Summary of effects chart for the area integrated in EIMs of all PFAS of the third DOE

The optimal parameters determined by the third DOE were: pre pulse storage of 12 μs, ion energy of 10 eV and collision cell in of 200 V.

They were tested, and the resulting mobility peaks (Figure 24) showed high resolving power excepted for N-MeFOSA, which consistently exhibited lower Rp.

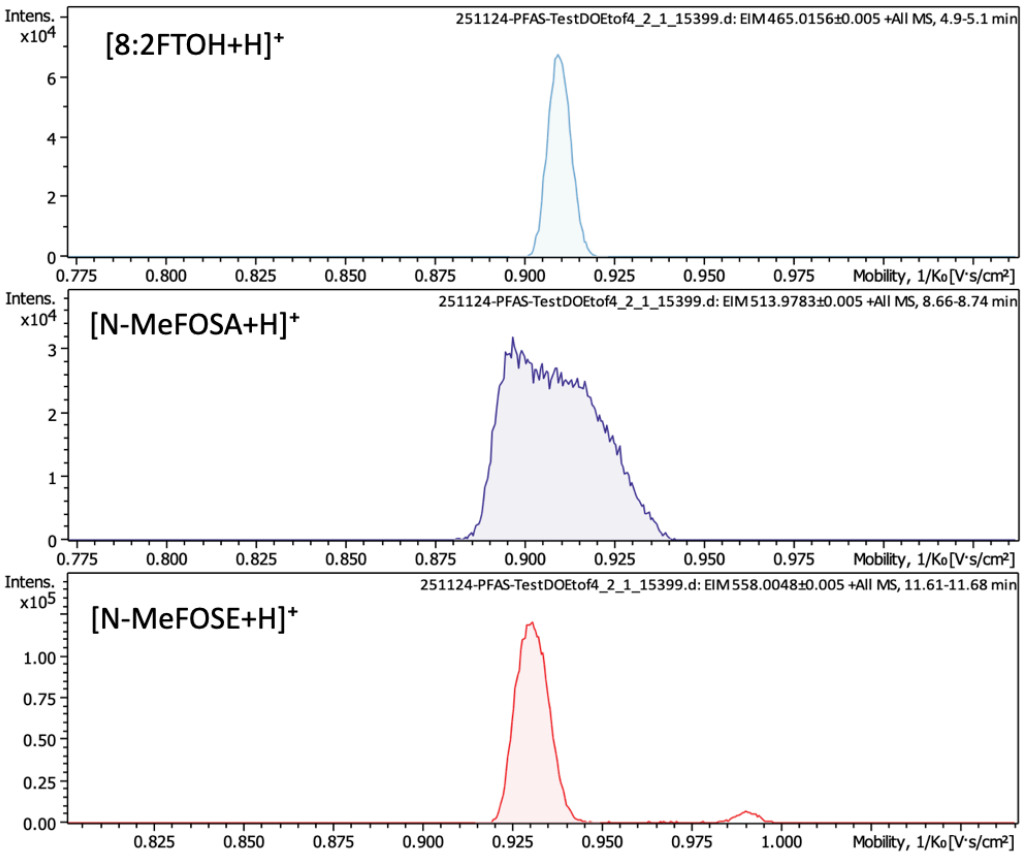

Figure 24: EIMs of 8 :2FTOH, N-MeFOSA and N-MeFOSE generated with the optimized parameters based on the third DOE

Before performing experiments aiming to investigate the origin of this larger mobility peak, the last parameter accumulation time, was optimized. Because this parameter is independent, it was optimised separately by varying its value from 5 to 250 ms while maintaining a fixed analysis (ramp) time of 250 ms. This experiment aimed to determine the accumulation time at which the TIMS cell becomes saturated.

The results, summarised in plots (see in Figure 25), show the integrated PFAS peak areas (from mobility-filtered EICs) normalized by their duty cycle (defined as Accumulation Time / Analysis Time).

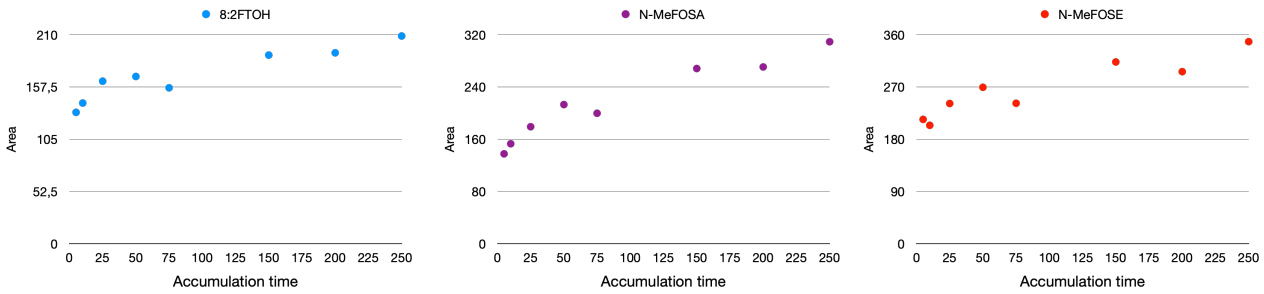

Figure 25: Plots of the intergraded PFAS peak areas normalized by their duty cycle

The plots of Figure 25 indicates that with an accumulation time between 150 and 175 ms, there are too many ions in the mobility cell resulting in its saturation. Therefore, an accumulation time of 165 ms was selected.

3. Hypothesis on the broadening of the ion mobility peak of N-MeFOSA

After the optimization, several tests were performed to understand and reduce the Rp of the N-MeFOSA mobilogram. One hypothesis was that the peak broadening could arise from the presence of dimers or trimers. However, these species may not have been visible in previous experiments due to the limited mass range (50-1000 m/z). To test this, an experiment was conducted using the optimized parameters but with an extended mass range (150-3000 m/z). No dimer or trimer species were detected in the mass spectra (see Figure 26).

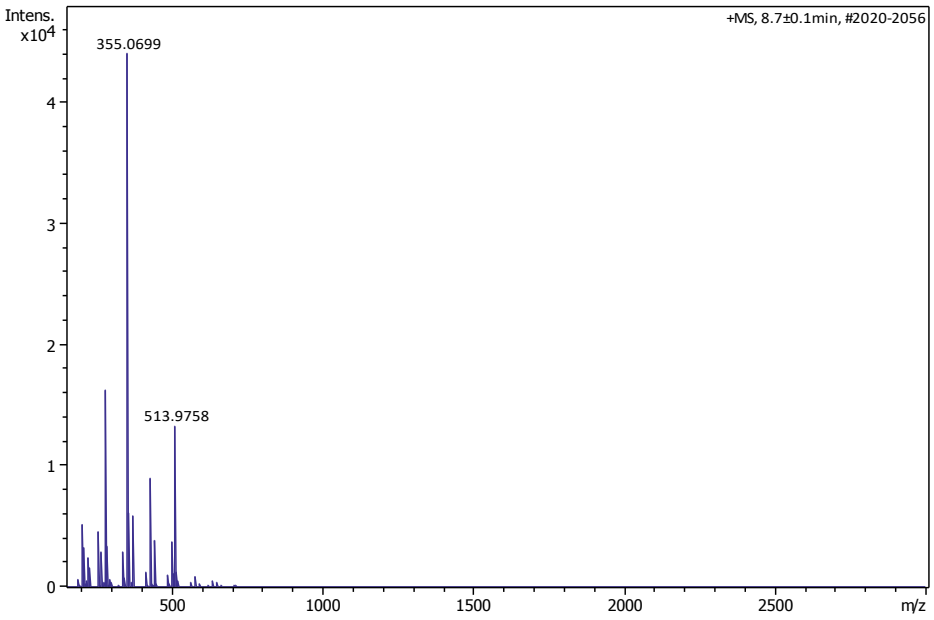

Figure 26: Mass spectrum of N-MeFOSA with a mass range (150-3000 m/z)

A second hypothesis was that the broadening could result from a high ion density in the TIMS cell, causing charge repulsion and therefore peak expansion, an effect known as *space-charge*. To investigate this, two analyses were performed using Ion Charge Control (ICC) set to 4M and then to 2M. ICC regulates the total number of ions allowed into the TIMS cell without altering the relative proportions of species. Thus, reducing the number of ions should reduce space-charge effects.

The EIMs of N-MeFOSA obtained under ICC conditions were compared with those acquired using the optimal parameters without ICC (see Figure 27). With ICC reduced to 2M, the mobility peak became slightly more focused. However, the Rp remained low in both cases.

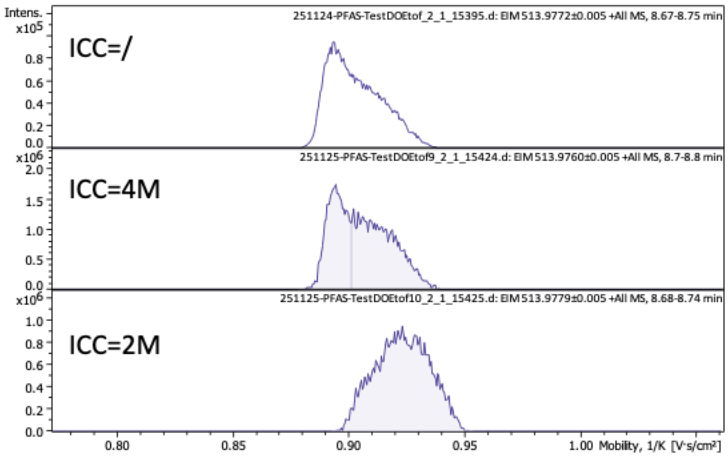

Figure 27: Comparison of N-MeFOSA EIMs without ICC (top), with an ICC of 4M (intermediary) and with an ICC of 2M (bottom)

A third hypothesis was that the observed broad peak originates from multiple protonation sites. Different protomers configuration were generated using the CREST (Conformer-Rotamer Ensemble Sampling Tool) software developed by the Grimme Lab [41]. Protonation sites were screened at the GFN2-xTB level in the gas phase. The resulting protomers were subsequently optimized using density functional theory (DFT) at the M06-2X/6-311++G(d,p) level of theory with the Gaussian 16 software package [42]. Following optimization, collision cross section (CCS) values were predicted using the trajectory method implemented in IMOS software (version 1.13) [43]. This method employs a 4-6-12 potential combined with an ion-quadrupole potential for nitrogen. This combination of geometry optimization and CCS calculation methods has previously been demonstrated by Schneiders *et al.* to be suitable for PFAS compounds [44].

Three protonation sites were identified (see Figure 28). The relative energy differences between these protomers were small, suggesting that they could coexist simultaneously. As these species exhibited similar CCS values due to an insufficient Rp, the corresponding peaks would not be separated. If the calculated CCS values are accurate, a resolving power of approximately 250 would be required to achieve peak separation between 185.08 Å² and 184.37 Å², which is relatively high.

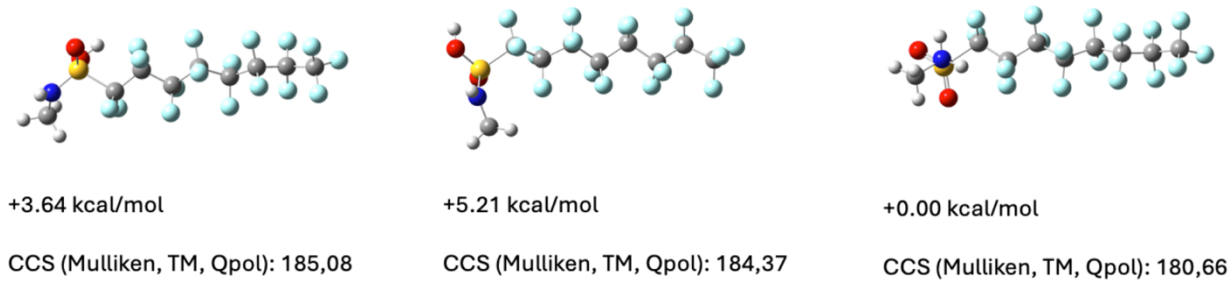

Figure 28: Three protomers of N-MeFOSA (red: oxygen atom, blue: nitrogen atom, dark gray: carbon atom, light gray: hydrogen atom, light blue: fluor atom and yellow: sulphur atom) with their relative energy (kcal/mol) and CCS value (Å²)

Overall, the broad ion mobility peak observed for N-MeFOSA could be attributed to a combination of space-charge effects and the presence of multiple protonation sites with similar CCS values. However, further theoretical calculations are required to confirm this hypothesis.

4. Fragmentation

The fragmentation of the three PFAS compounds was analyzed under both TIMS-off and TIMS-on conditions. For each PFAS, the mass spectrum was examined to identify fragment ions. To confirm that the observed fragments originated from the corresponding precursor ions, EICs were generated to check that fragment retention times matched those of their parent ions.

a) TIMSoff

The mass spectrum of 8:2 FTOH (Figure 29) indicates that the most intense ions correspond to a proton water adduct, $[M + H + H_2O]^+$. A second water adduct, $[M + H + 2H_2O]^+$, is also present with an intensity similar to that of the protonated molecule $[M + H]^+$. Fragmentation was limited: only one clear fragment, $[M - HF - H_2O]^{+\bullet}$, was observed, along with two additional suspected fragments that could not be confidently assigned. The EICs for each species (Figure 30) confirm that their retention times matched that of the parent ion.

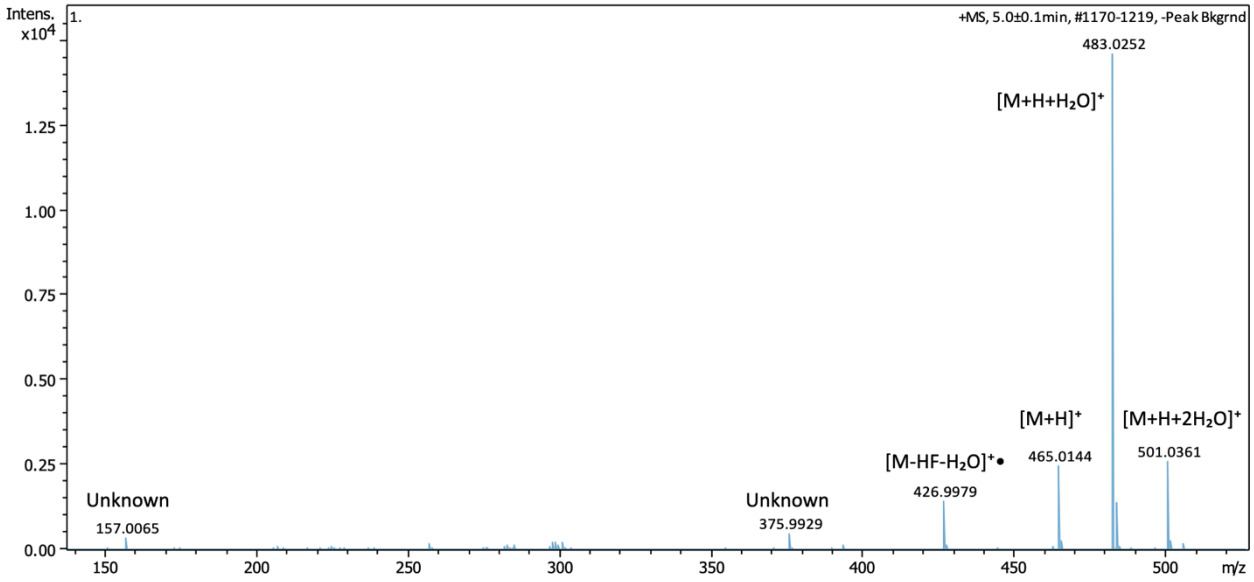

Figure 29: mass spectrum of 8 :2FTOH in TIMSoff

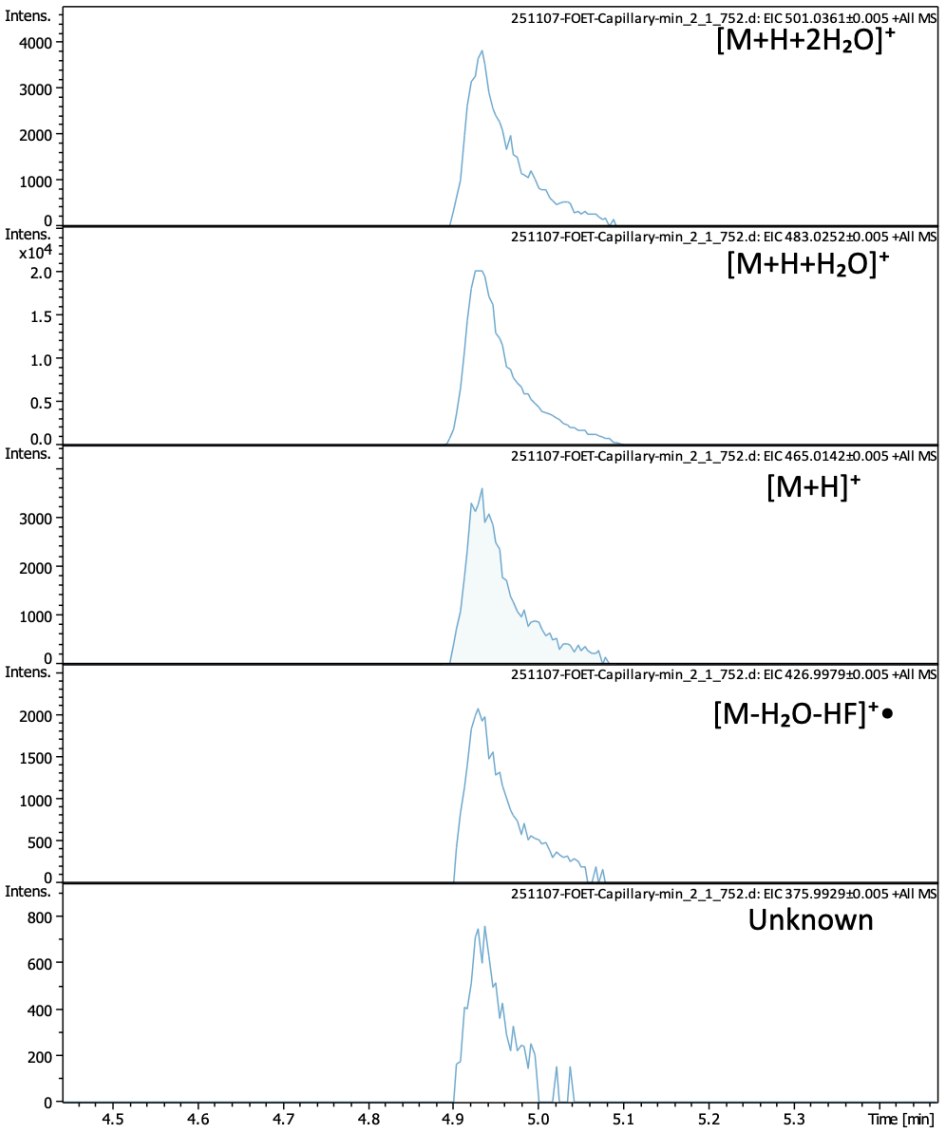

Figure 30: EICs of ***[M + H]⁺, [M + H + H₂O]⁺, [M + H +2 H₂O]⁺, [M – HF – H₂O]⁺• and two suspects***

For N-MeFOSA (Figure 31), the protonated molecule $[M + H]^+$ is the most intense signal and shows no significant fragmentation. However, three water adducts are present: $[M + H + H_2O]^+$, $[M + H + 2H_2O]^+$, and $[M + H + 3H_2O]^+$.

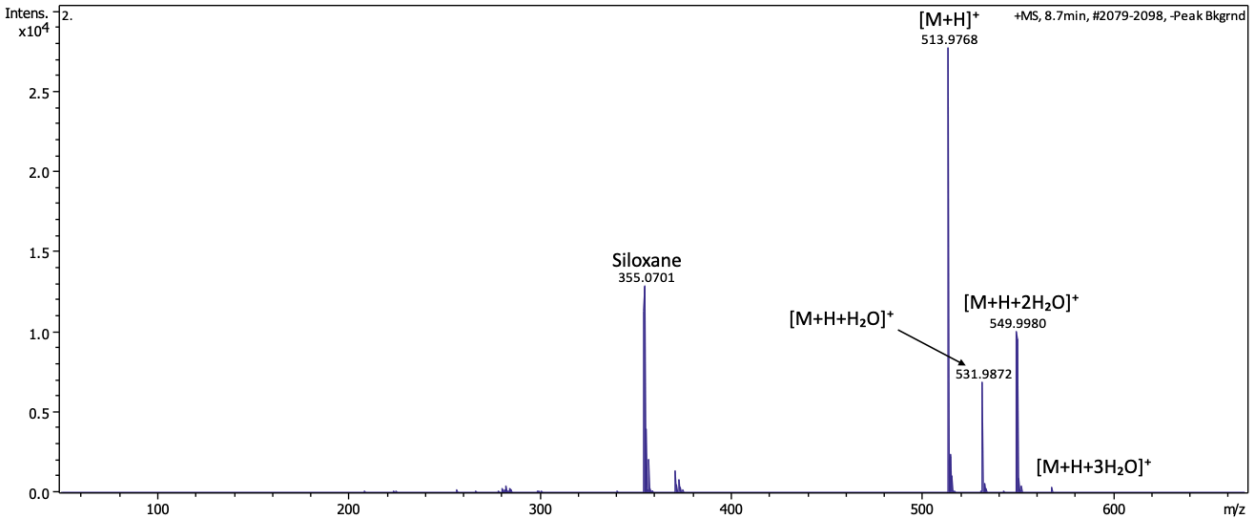

Figure 31: mass spectrum of N-MeFOSE in TIMSoff

The mass spectrum of N-MeFOSE (Figure 32) shows limited but detectable fragmentation, producing two fragments: $[M + H - H_2O]^+$ and $[M - COH_3]^{+\bullet}$. A water adduct was also observed.

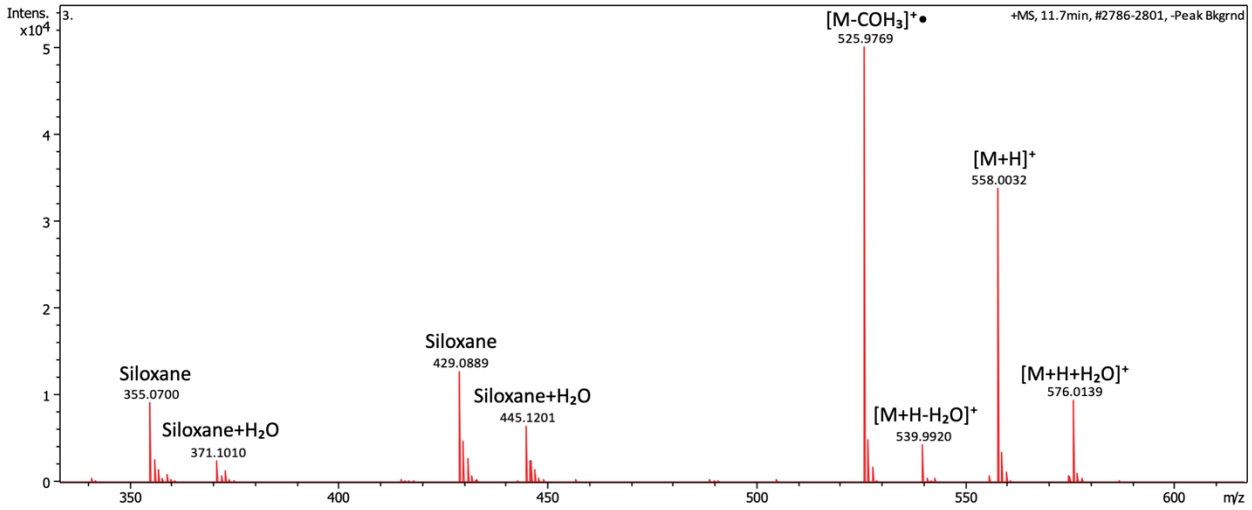

Figure 32: mass spectrum of N-MeFOSE in TIMSoff

Overall, fragmentation under TIMS-off conditions was minimal. This behavior is consistent with the use of an APCI ionization source, where extensive fragmentation is not typically observed and water adduct formation is common. The presence of water adducts originates from residual moisture in the nitrogen gas as indicated in the equation 10 of section experimental.

b) TIMSon

Mobility provides an additional dimension for identifying fragments. In this study, mobilograms were generated based on the mass spectra. A compound can fragment in two different regions:

(i) in the source and/or in the IM region ("before fragmentation"), or (ii) in the detector ("after fragmentation"). Fragments exhibit different CCS values depending on where fragmentation occurs. Species generated *before* fragmentation are analyzed directly as fragments and therefore usually display lower CCS values than the precursor. In contrast, species formed *after* fragmentation are analyzed as precursors and retain the CCS of the parent ion.

The mass spectrum of 8:2 FTOH (Figure 33) shows the same species observed under TIMS-off conditions, with the addition of one extra fragment, $[M - 2HF - H_2O]^{+\bullet}$. The measured CCS measured of 8:2 FTOH was of 189,1 $Å^2$, which is closer to the CCS in the literature: 191 $Å^2$ [13].

The mobilogram (Figure 34) indicates that the water adduct exhibits the same CCS as the parent ion. For the fragment $[M - HF - H_2O]^{+\bullet}$, two mobility peaks are observed. The peak with the higher CCS aligns with the CCS of the parent ion indicating the origin of this fragment and corresponding to an after-fragmentation species, whereas the peak with the lower CCS corresponds to a before-fragmentation species. For the fragment $[M - 2HF - H_2O]^{+\bullet}$, one peak is observed that corresponds to the before-fragmentation species.

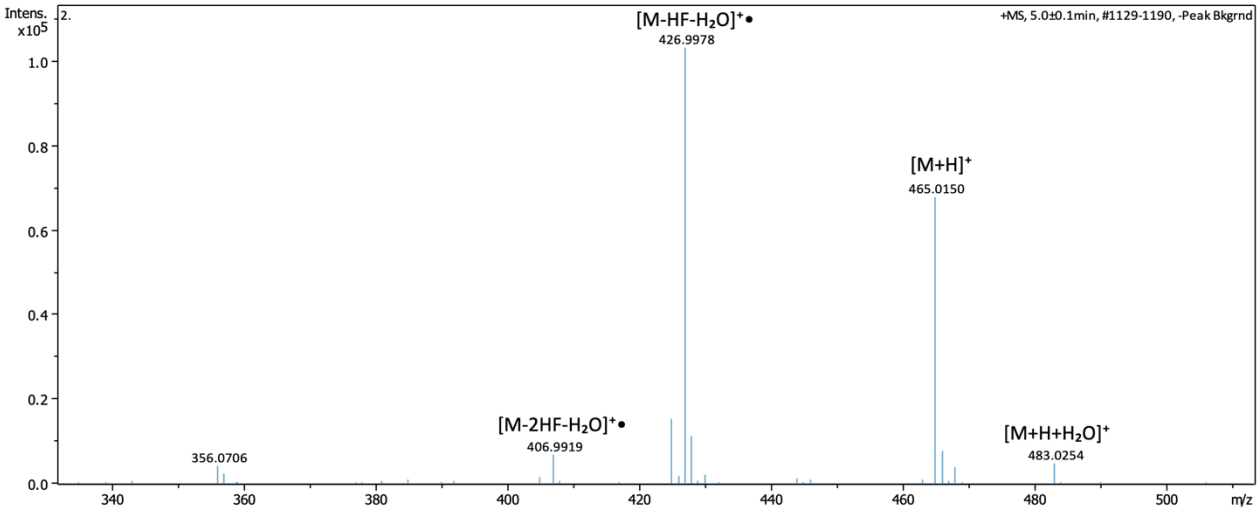

Figure 33: Mass spectrum of 8:2FTOH in TIMSon

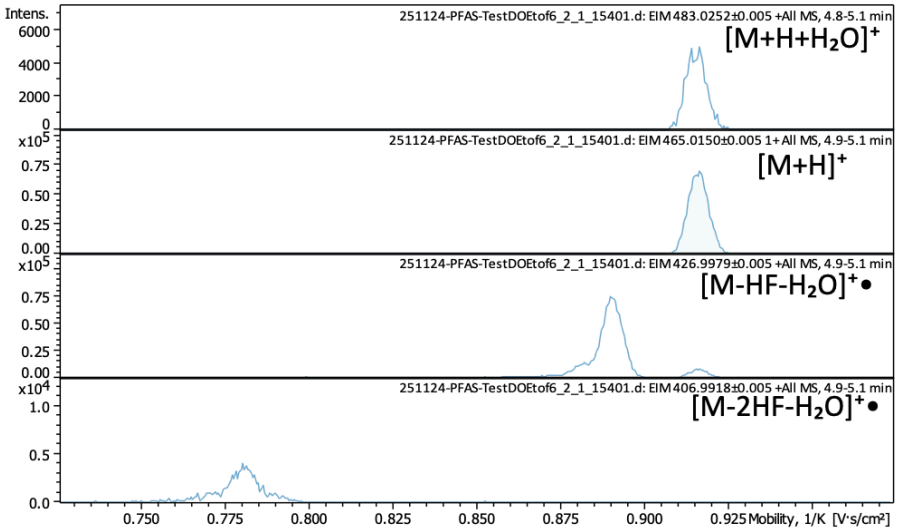

Figure 34: Mobilogram of 8:2FTOH, these fragments and adducts

For N-MeFOSA (Figure 35), the protonated molecule $[M + H]^+$ remains the most intense signal. One additional fragment was detected, $[M\text{-}SO_2+H]^+$ [41]. Water adducts are less abundant compared with TIMS-off conditions. The adduct shows the same CCS as the parent ion (Figure 36). For $[M\text{-}SO_2+H]^+$, a lower-CCS signal is present and could correspond to a before-fragmentation species. The CCS measured of N-MeFOSA was of 186,2 $\pm$ 3,1 $Å^2$ with the range determined at half of the maximum intensity.

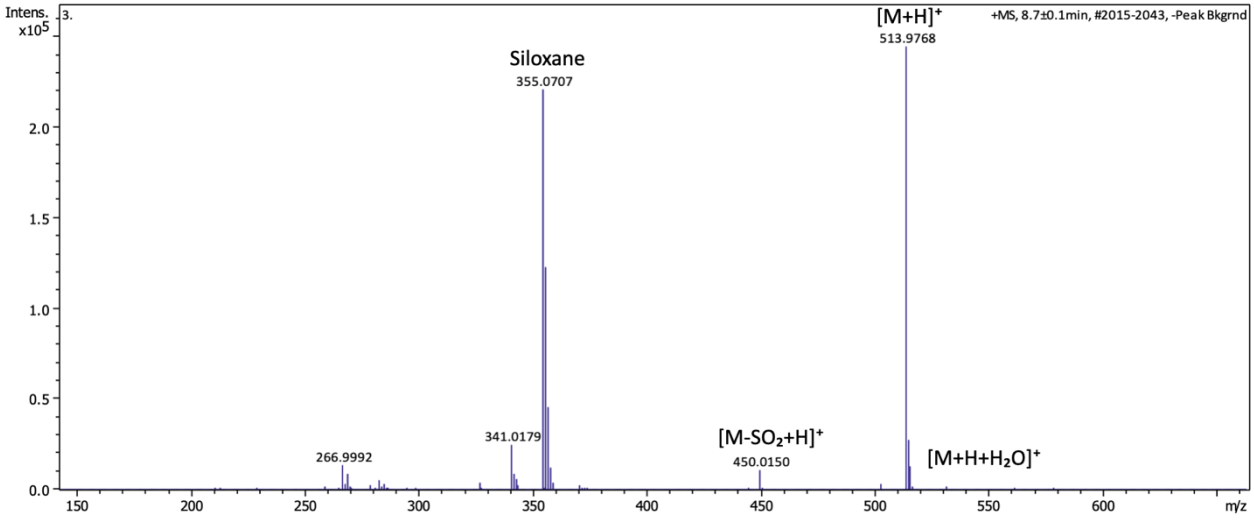

Figure 35: Mass spectrum of N-MeFOSA in TIMSon

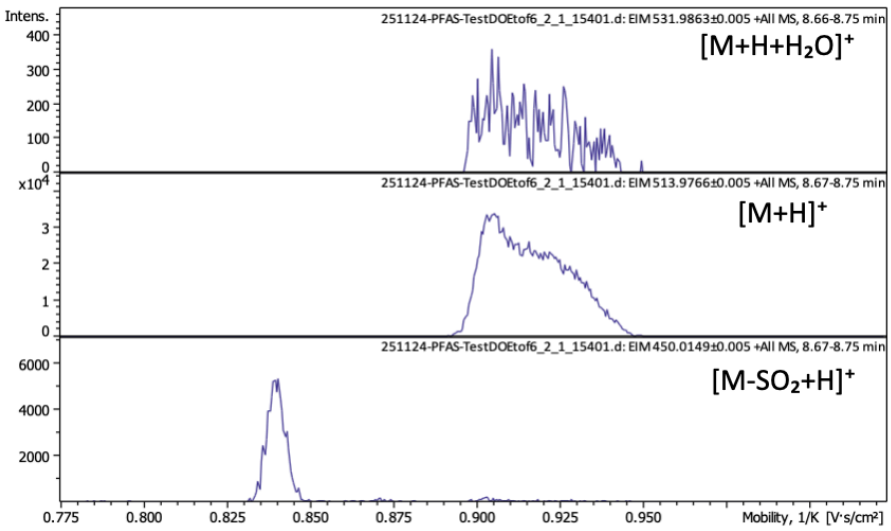

Figure 36: Mobilogram of N-MeFOSA, this fragment and adduct

The mass spectrum of N-MeFOSE (Figure 37) also exhibits the same species observed under TIMS-off conditions, with water adducts again being less abundant. One additional fragment was detected, but its structure could not be resolved.

The CCS measured of N-MeFOSE was of 192,9 $Å^2$. In the literature, a value CCS of 197,6 $Å^2$ was determinate in a cIMS [11]. The error percentage between these two values is 2,4% that is slightly higher than the limited value 2% [45,46] but remained acceptable.

Two peaks are observed in the mobilogram (Figure 38) for the $[M + H - H_2O]^+$ fragment. The peak with the higher CCS aligns with the CCS of the parent ion and thus corresponds to an after-fragmentation species. The lower-CCS peak corresponds to a before-fragmentation species. For the $[M - COH_3]^{+\bullet}$ fragment, one peak is observed that could correspond to a before-fragmentation species.

For the suspect compound, its mobilogram also contains two peaks. One aligns with the lower-CCS peak of $[M - COH_3]^{+\bullet}$, suggesting it may be a fragment of this species. The second peak, with a lower CCS, could correspond to a before-fragmentation species.

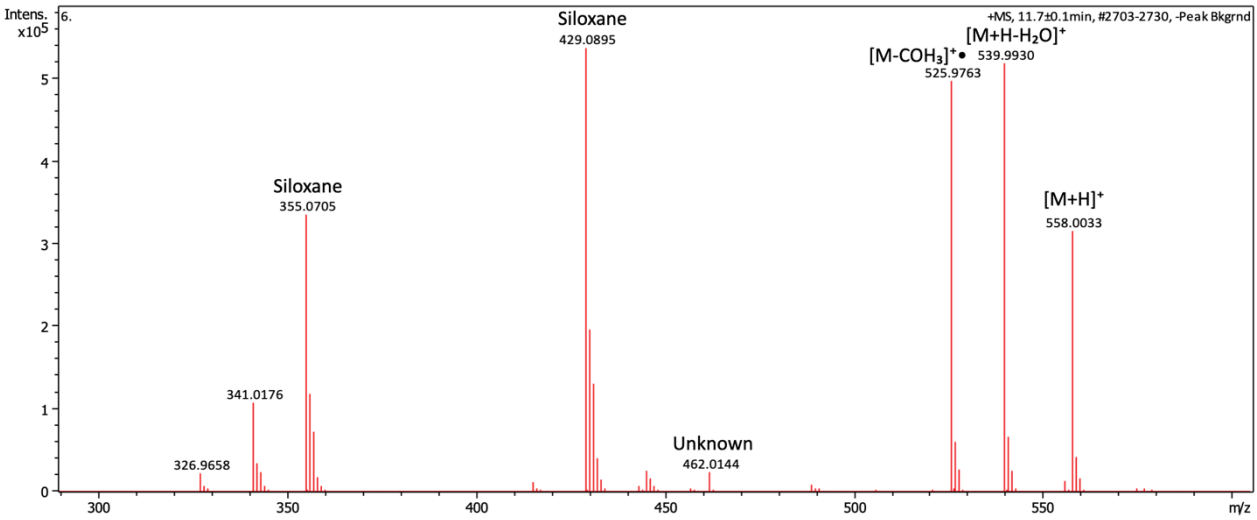

Figure 37: Mass spectrum of N-MeFOSE in TIMSon

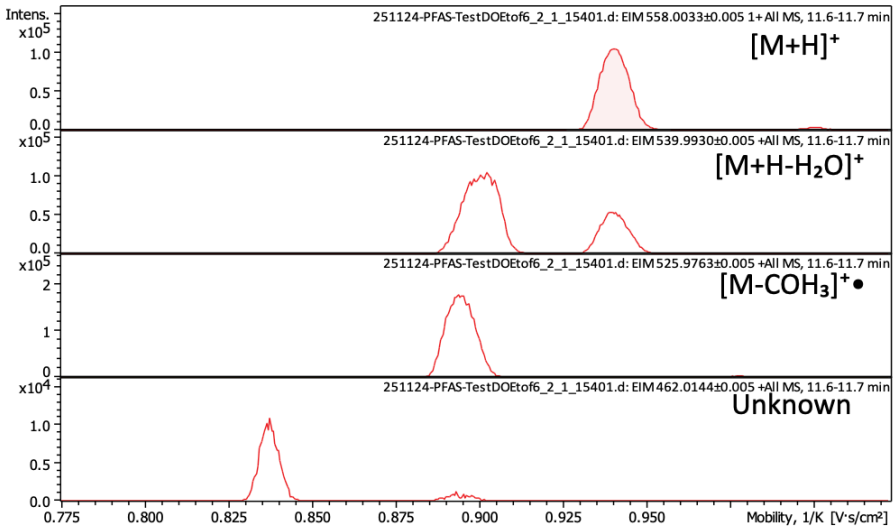

Figure 38: Mobilogram of N-MeFOSE and these fragments

Overall, fragmentation was slightly more pronounced under TIMS-on conditions, while water adducts were less abundant. This reduction in water adducts may suggest degradation or dissociation of the adducts due to the higher energy and increased residence time within the TIMS device.

E. Intermediate conclusion and perspectives

In this study, a method was developed for the analysis of three volatile PFAS-perfluorooctyl ethanol, *N*-methylperfluoro-1-octanesulfonamide, and 2-(*N*-methylperfluoro-1-octanesulfonamido) ethanol, using a GC-APCI-TIMS-TOFMS instrument, along with the identification of their fragmentation patterns. Through a combination of classical optimization and DOE, the source, TIMS, and TOF parameters were successfully optimized.

During this optimization, a broad ion mobility peak was observed for *N*-MeFOSA. This behavior may be attributed to a combination of space-charge effects and the presence of multiple protonation sites with similar CCS values. However, further theoretical calculations are required to confirm this hypothesis.

Fragmentation was found to be slightly more pronounced under TIMS-on conditions, whereas water adducts were less abundant. This decrease in water adduct formation may indicate degradation or dissociation of the adducts due to the higher energy and increased residence time within the TIMS device.

Future studies could investigate the use of deactivated liners to reduce chromatographic tailing, as well as the development of a PTV injection method to lower injector temperatures.

F. References

[1] Kanan, Sofian, and Fatin Samara. 'Dioxins and Furans: A Review from Chemical and Environmental Perspectives'. Trends in Environmental Analytical Chemistry 17 (1 January 2018): 1–13. https://doi.org/10.1016/j.teac.2017.12.001.

[2] Nuttall, William J., Richard H. Clarke, and Bartek A. Glowacki. 'Stop Squandering Helium'. Nature 485, no. 7400 (May 2012): 573–75. https://doi.org/10.1038/485573a.

[3] Cutillas, Víctor, Guillermo García-Gallego, María Murcia-Morales, Carmen Ferrer, and Amadeo R. Fernández-Alba. 'Beyond Helium: Hydrogen as a Carrier Gas in Multiresidue Pesticide Analysis in Fruits and Vegetables by GC-MS/MS'. Analytical Methods 16, no. 11 (2024): 1564–69. https://doi.org/10.1039/D3AY02119J.

[4] Fulara. 'Methods for Determination of Polybrominated Diphenyl Ethers in Environmental Samples – Review - 2012 - Journal of Separation Science - Wiley Online Library'. Accessed 23 April 2025. https://analyticalsciencejournals.onlinelibrary.wiley.com/doi/full/10.1002/jssc.201200100.

[5] Fang, Jing, Hongzhi Zhao, Yanhao Zhang, Minghua Lu, and Zongwei Cai. 'Atmospheric Pressure Chemical Ionization in Gas Chromatography-Mass Spectrometry for the Analysis of Persistent Organic Pollutants'. Trends in Environmental Analytical Chemistry 25 (1 March 2020): e00076. https://doi.org/10.1016/j.teac.2019.e00076.

[6] Siddhantakar, Ankesh, Jair Santillán-Saldivar, Thomas Kippes, Guido Sonnemann, Armin Reller, and Steven B. Young. 'Helium Resource Global Supply and Demand: Geopolitical Supply Risk Analysis'. Resources, Conservation and Recycling 193 (1 June 2023): 106935. https://doi.org/10.1016/j.resconrec.2023.106935.

[7] Eurofins Scientific. 'Dioxins, Furans & dL-PCBs'. Accessed 7 January 2026. https://www.eurofins.com.au/environment-testing/speciality-services/dioxins-furans-dl-pcbs/.

[8] 'Fichier:PCB structure general.svg — Wikipédia'. June 2009. https://commons.wikimedia.org/wiki/File:PCB_structure_general.svg.

[9] Fang, Jing, Hongzhi Zhao, Yanhao Zhang, Minghua Lu, and Zongwei Cai. 'Atmospheric Pressure Chemical Ionization in Gas Chromatography-Mass Spectrometry for the Analysis of Persistent Organic Pollutants'. *Trends in Environmental Analytical Chemistry* 25 (March 2020): e00076. https://doi.org/10.1016/j.teac.2019.e00076.

[10] 'Perfluoroalkyl and Polyfluoroalkyl Substances in the Environment: Terminology, Classification, and Origins'. https://doi.org/10.1002/ieam.258.

[11] Whitehead, Heather D., and Graham F. Peaslee. 'Directly Fluorinated Containers as a Source of Perfluoroalkyl Carboxylic Acids'. Environmental Science & Technology Letters 10, no. 4 (2023): 350–55. https://doi.org/10.1021/acs.estlett.3c00083.

[12] Casey, Jonathan S, Stephen R Jackson, Jeff Ryan, and Seth R Newton. 'The Use of Gas Chromatography – High Resolution Mass Spectrometry for Suspect Screening and Non-Targeted Analysis of per- and Polyfluoroalkyl Substances'. Journal of Chromatography A 1693 (March 2023): 463884. https://doi.org/10.1016/j.chroma.2023.463884.

[13] MacNeil, Amber, Xiaolei Li, Roshanak Amiri, et al. 'Gas Chromatography-(Cyclic) Ion Mobility Mass Spectrometry: A Novel Platform for the Discovery of Unknown Per-/Polyfluoroalkyl Substances'. Analytical Chemistry 94, no. 31 (2022): 11096–103. https://doi.org/10.1021/acs.analchem.2c02325.

[14] Fábio Barbosa Machado Torres et al., 'Brazilian Overview of Per- and Polyfluoroalkyl Substances Listed as Persistent Organic Pollutants in the Stockholm Convention', Chemosphere 291 (March 2022): 132674, https://doi.org/10.1016/j.chemosphere.2021.132674.
[15] Convention, Stockholm. 'Information on the 16 Chemicals Added to the Stockholm Convention'. BRSMeas. Accessed 7 January 2026. https://chm.pops.int/?tabid=2511.
[16] Jahnke, Annika, Lutz Ahrens, Ralf Ebinghaus, Urs Berger, Jonathan L. Barber, and Christian Temme. 'An Improved Method for the Analysis of Volatile Polyfluorinated Alkyl Substances in Environmental Air Samples'. Analytical and Bioanalytical Chemistry 387, no. 3 (2007): 965–75. https://doi.org/10.1007/s00216-006-1008-y.
[17] Drumheller, Paul D., Nadine Ding, Joyce Y. Wong, Dawn Beraud, and Pierce J. Vatterott. 'PFAS Regulations and the Potential Impacts on Patient Care'. Heart Rhythm, July 2025, S1547527125025196. https://doi.org/10.1016/j.hrthm.2025.05.058.
[18] 'Ineris-229262_2816719_PFAS_usages_essentiels_en.Pdf'. n.d. Accessed 8 January 2026. https://www.ineris.fr/sites/default/files/contribution/Documents/Ineris-229262_2816719_PFAS_usages_essentiels_en.pdf.
[19] Schlummer, Martin, Ludwig Gruber, Dominik Fiedler, Markus Kizlauskas, and Josef Müller. 'Detection of Fluorotelomer Alcohols in Indoor Environments and Their Relevance for Human Exposure'. Environment International 57–58 (July 2013): 42–49. https://doi.org/10.1016/j.envint.2013.03.010.
[20] Cahuas, Liliana, Derek J. Muensterman, Mitchell L. Kim-Fu, Patrick N. Reardon, Ivan A. Titaley, and Jennifer A. Field. 'Paints: A Source of Volatile PFAS in Air–Potential Implications for Inhalation Exposure'. Environmental Science & Technology 56, no. 23 (2022): 17070–79. https://doi.org/10.1021/acs.est.2c04864.
[21] Riedel, Theran P., Johnsie R. Lang, Mark J. Strynar, Andrew B. Lindstrom, and John H. Offenberg. 'Gas-Phase Detection of Fluorotelomer Alcohols and Other Oxygenated Per- and Polyfluoroalkyl Substances by Chemical Ionization Mass Spectrometry'. Environmental Science & Technology Letters 6, no. 5 (2019): 289–93. https://doi.org/10.1021/acs.estlett.9b00196.
[22] Kapuscinski, Richard B. 'Research Needs Regarding the Vapor Intrusion Potential of Volatile Per- and Polyfluoroalkyl Substances'. Environmental Science & Technology, 23 February 2024, acs.est.3c06227. https://doi.org/10.1021/acs.est.3c06227.
[23] Zuccaro, Philip, James Licato, Emily A. Davidson, David C. Thompson, and Vasilis Vasiliou. 'Assessing Extraction-Analysis Methodology to Detect Fluorotelomer Alcohols (FTOH), a Class of Perfluoroalkyl and Polyfluoroalkyl Substances (PFAS), in Artificial Turf Fibers and Crumb Rubber Infill'. Case Studies in Chemical and Environmental Engineering 7 (June 2023): 100280. https://doi.org/10.1016/j.cscee.2022.100280.
[24] Zango, Zakariyya Uba, Baranitharan Ethiraj, Fahad S. Al-Mubaddel, et al. 'An Overview on Human Exposure, Toxicity, Solid-Phase Microextraction and Adsorptive Removal of Perfluoroalkyl Carboxylic Acids (PFCAs) from Water Matrices'. Environmental Research 231 (August 2023): 116102. https://doi.org/10.1016/j.envres.2023.116102.
[25] Ruyle, Bridger J., Colin P. Thackray, Craig M. Butt, et al. 'Centurial Persistence of Forever Chemicals at Military Fire Training Sites'. Environmental Science & Technology 57, no. 21 (2023): 8096–106. https://doi.org/10.1021/acs.est.3c00675.
[26] Garg, Anushka, Nagaraj P. Shetti, Soumen Basu, Mallikarjuna N. Nadagouda, and Tejraj M. Aminabhavi. 'Treatment Technologies for Removal of Per- and Polyfluoroalkyl Substances (PFAS)

in Biosolids'. Chemical Engineering Journal 453 (February 2023): 139964. https://doi.org/10.1016/j.cej.2022.139964.
[27] Belova, Lidia, Noelia Caballero-Casero, Alexander L. N. Van Nuijs, and Adrian Covaci. 'Ion Mobility-High-Resolution Mass Spectrometry (IM-HRMS) for the Analysis of Contaminants of Emerging Concern (CECs): Database Compilation and Application to Urine Samples'. Analytical Chemistry 93, no. 16 (2021): 6428–36. https://doi.org/10.1021/acs.analchem.1c00142.
[28] Dodds, James N., Zachary R. Hopkins, Detlef R. U. Knappe, and Erin S. Baker. 'Rapid Characterization of Per- and Polyfluoroalkyl Substances (PFAS) by Ion Mobility Spectrometry–Mass Spectrometry (IMS-MS)'. Analytical Chemistry 92, no. 6 (2020): 4427–35. https://doi.org/10.1021/acs.analchem.9b05364.
[29] Ahmed, Ezaz, K.M. Mohibul Kabir, Huixin Wang, Dan Xiao, John Fletcher, and William A. Donald. 'Rapid Separation of Isomeric Perfluoroalkyl Substances by High-Resolution Differential Ion Mobility Mass Spectrometry'. Analytica Chimica Acta 1058 (June 2019): 127–35. https://doi.org/10.1016/j.aca.2019.01.038.
[30] Labad, Francesc, and Sandra Pérez. 'Qualitative and Quantitative Analysis of Highly-Polar Contaminants in Atlanta Urban Water'. Analytica Chimica Acta 1369 (October 2025): 344349. https://doi.org/10.1016/j.aca.2025.344349.
[31] Discovery, JMP Statistical. 'Design of Experiments'. Accessed 7 January 2026. https://www.jmp.com/en/statistics-knowledge-portal/design-of-experiments.
[32] Kasemiire, Alice, Hermane T. Avohou, Charlotte De Bleye, et al. 'Design of Experiments and Design Space Approaches in the Pharmaceutical Bioprocess Optimization'. European Journal of Pharmaceutics and Biopharmaceutics 166 (September 2021): 144–54. https://doi.org/10.1016/j.ejpb.2021.06.004.
[33] reserved, Mettler-Toledo International Inc all rights. 'Design of Experiments (DoE)'. Accessed 7 January 2026. https://www.mt.com/be/nl/home/applications/L1_AutoChem_Applications/L2_ReactionAnalysis/design-of-experiments-doe.cmp.sea_01010703.html.
[34] Folorunsho, Omotola, Jishnu Pandamkulangara Kizhakkethil, Anna Bogush, and Ivan Kourtchev. 'Effect of Short-Term Sample Storage and Preparatory Conditions on Losses of 18 per- and Polyfluoroalkyl Substances (PFAS) to Container Materials'. Chemosphere 363 (September 2024): 142814. https://doi.org/10.1016/j.chemosphere.2024.142814.
[35] 'Guidance%20Document%20PFAS%20V2.0%20(Incl.%20Annex%20V2.0).Pdf?G-66352cfe'. n.d. Accessed 8 January 2026. https://eurl-pops.eu/user/pages/05.news/48.Guidance-Document-PFAS/Guidance%20Document%20PFAS%20V2.0%20(incl.%20Annex%20V2.0).pdf?g-66352cfe.
[36] Discovery, JMP Statistical. 'Multiple Regression Residual Analysis and Outliers'. Accessed 7 January 2026. https://www.jmp.com/en/statistics-knowledge-portal/what-is-multiple-regression/mlr-residual-analysis-and-outliers.
[37] JMP User Community. 'How to Get a P-Value on Descriptive Statistics? How to Get Cramer's V Statistic?' 6 July 2010. https://community.jmp.com/t5/Discussions/How-to-get-a-p-value-on-descriptive-statistics-How-to-get-Cramer/td-p/2038.
[38] SurveyMonkey. 'Calculateur rapide de votre valeur p'. Accessed 7 January 2026. https://fr.surveymonkey.com/learn/research-and-analysis/p-value-calculator/.

[39] JMP User Community. 'What Does logWorth Measure That Is Not Included in the Anova Table of a Fit Model Analysis?' 13 September 2022. https://community.jmp.com/t5/Discussions/What-does-logWorth-measure-that-is-not-included-in-the-anova/td-p/544036.
[40] Muller, Hugo. Advancing the Analysis of Halogenated Contaminants Using a GC-APCI-TIMS-TOFMS Platform: Development and Optimization for Targeted and Non-Targeted Approaches. ULiège - University of Liège [Science], Liège, Belgium, 3 September 2025. https://orbi.uliege.be/handle/2268/335926.
[41] Pracht, Philipp, Fabian Bohle, and Stefan Grimme. 'Automated Exploration of the Low-Energy Chemical Space with Fast Quantum Chemical Methods'. Physical Chemistry Chemical Physics 22, no. 14 (2020): 7169–92. https://doi.org/10.1039/C9CP06869D.
[42] Frisch, M. J.; Trucks, G. W.; Schlegel, H. B.; Scuseria, G. E.; Robb,M.A.;Cheeseman,J.R.;Scalmani,G.;Barone,V.;Petersson,G.A.;Nakatsuji,H.;Li,X.;Caricato,M.; Marenich,A.V.;Bloino,J.;Janesko,B.G.;Gomperts,R.;Mennucci,B.;Hratchian,H.P.;Ortiz,J.V.;Izmaylov,A.F.;Sonnenberg,J.L.;WilliamsYoung,D.;Ding,F.;Lipparini,F.;Egidi,F.;Goings,J.;Peng,B.;Petrone,A.;Henderson,T.;Ranasinghe,D.;Zakrzewski,V.G.;Gao,J.;Rega,N.;Zheng,G.;Liang,W.;Hada,M.;Ehara, M.;Toyota,K.;Fukuda,R.;Hasegawa,J.;Ishida,M.;Nakajima,T.;Honda,Y.;Kitao,O.;Nakai,H.;Vreven,T.;Throssell, K.; Montgomery, J. A., Jr.; Peralta, J. E.; Ogliaro, F.; Bearpark,M.J.;Heyd,J.J.;Brothers,E.N.;Kudin,K.N.;Staroverov,V. N.; Keith, T. A.; Kobayashi, R.; Normand, J.; Raghavachari, K.; Rendell, A. P.; Burant, J. C.; Iyengar, S. S.; Tomasi, J.; Cossi, M.; Millam, J. M.; Klene, M.; Adamo, C.; Cammi, R.; Ochterski, J. W.; Martin,R.L.;Morokuma,K.;Farkas,O.;Foresman,J.B.;Fox,D.J.Gaussian 16,RevisionC.01;Gaussian,Inc.:WallingfordCT,2016.
[43] Larriba, Carlos, and Christopher J. Hogan. 'Ion Mobilities in Diatomic Gases: Measurement versus Prediction with Non-Specular Scattering Models'. The Journal of Physical Chemistry A 117, no. 19 (2013): 3887–901. https://doi.org/10.1021/jp312432z.
[44] Schneiders, Aurore L., Johann Far, Lidia Belova, et al. 'Structural Characterization of Dimeric Perfluoroalkyl Carboxylic Acid Using Experimental and Theoretical Ion Mobility Spectrometry Analyses'. Journal of the American Society for Mass Spectrometry 36, no. 4 (2025): 850–61. https://doi.org/10.1021/jasms.5c00007.
[45] Celma, Alberto, Juan V. Sancho, Emma L. Schymanski, et al. 'Improving Target and Suspect Screening High-Resolution Mass Spectrometry Workflows in Environmental Analysis by Ion Mobility Separation'. *Environmental Science & Technology* 54, no. 23 (2020): 15120–31. https://doi.org/10.1021/acs.est.0c05713.
[46] Goscinny, Séverine, Laure Joly, Edwin De Pauw, Vincent Hanot, and Gauthier Eppe. 'Travelling-Wave Ion Mobility Time-of-Flight Mass Spectrometry as an Alternative Strategy for Screening of Multi-Class Pesticides in Fruits and Vegetables'. *Journal of Chromatography A* 1405 (July 2015): 85–93. https://doi.org/10.1016/j.chroma.2015.05.057.

G. Supporting information

DOE	Corona current (nA)	Nebulizer pressure (bar)	Dry gas T (°C)	Capillary voltage (V)	Transfer line T (°C)	I (8:2FTOH)	I (N-MeFOSA)	I (N-MeFOSE)
1	1000	3	225	3000	200	2643	43202	37993
2	500	2,5	200	2500	225	2573	44005	55285
3	1500	3,5	200	2500	225	1438	26849	23452
4	1500	2,5	250	2500	225	2895	47659	78789
5	500	3,5	250	2500	225	1557	26443	27465
6	1500	2,5	200	3500	225	2617	48228	54238
7	500	3,5	200	3500	225	1722	30240	27577
8	500	2,5	250	3500	225	2627	39483	45686
9	1500	3,5	250	3500	225	2136	30492	27999
10	1000	3	225	2090	250	2582	40281	37309
11	1000	3	179,5	3000	250	2558	41203	40301
12	1000	2,09	225	3000	250	3327	48760	57071
13	400	3	225	3000	250	2306	29974	24096
14	1000	3	225	3000	250	2256	38888	35224
15	1000	3	225	3000	250	2297	41510	34984
16	1000	3	225	3000	250	2471	39580	33908
17	1000	3	225	3000	250	2477	40866	34261
18	1000	3	225	3000	250	2943	42224	39166
19	1000	3	225	3000	250	2734	42259	35911
20	1910	3	225	3000	250	2792	40655	36040
21	1000	3,91	225	3000	250	2506	39708	31927
22	1000	3	270,5	3000	250	2522	37402	45731
23	1000	3	225	3910	250	3062	44581	39657
24	1500	2,5	200	2500	275	3870	70193	83897
25	500	3,5	200	2500	275	2261	38188	36163
26	500	2,5	250	2500	275	2691	45361	66987
27	1500	3,5	250	2500	275	2388	36809	34355
28	500	2,5	200	3500	275	3720	54718	53107
29	1500	3,5	200	3500	275	2738	39072	36249

30	1500	2,5	250	3500	275	4323	59544	78124
31	500	3,5	250	3500	275	2723	37288	37291
32	1000	3	225	3000	300	2733	46558	38780

Table S1: Values of corona current, nebulizer, dry gas T, capillary voltage and transfer line T parameters and responses for the first DOE

DOE	Funnel1 RF (Vpp)	Collision RF (App)	Transfer Time (μs)	Δ3 (V)	Δ6 (V)	A (8:2FTOH)	A (N-MeFOSA)	A (N-MeFOSE)	FWHM (8:2FTOH)	FWHM (N-MeFOSA)	FWHM (N-MeFOSE)	Rp (8:2FTOH)	Rp (N-MeFOSA)	Rp (N-MeFOSE)
1	275	2000	55	200	100	650	833	1170	0,008	0,012	0,011	121	78	83
2	100	3000	55	200	100	155	885	1117	0,009	0,013	0,01	104	72	90
3	450	1000	55	200	100	1261	1399	1626	0,008	0,011	0,012	115	80	78
4	275	2000	70	150	100	708	1020	741	0,007	0,01	0,011	125	95	82
5	100	2000	70	200	100	417	488	707	0,055	0,05	0,049	15	17	17
6	275	2000	55	200	100	1119	1502	1666	0,008	0,013	0,011	121	70	83
7	100	1000	55	200	100	758	917	1553	16,467	16,908	17,271	1	1	1
8	100	2000	40	200	100	88	387	678	0,037	0,046	0,044	23	18	19
9	275	3000	55	200	50	582	1253	1528	0,008	0,021	0,012	119	42	80
10	450	2000	70	200	100	566	814	1294	0,007	0,012	0,012	124	74	80
11	275	1000	55	200	50	1043	1339	1813	0,007	0,012	0,011	122	75	82
12	450	2000	40	200	100	227	715	1278	0,009	0,013	0,011	103	70	81
13	275	2000	55	200	100	957	1463	1858	0,008	0,012	0,012	119	73	77
14	275	3000	55	200	150	177	1027	1072	0,007	0,014	0,01	129	65	90
15	450	3000	55	200	100	526	1155	1543	0,008	0,012	0,012	118	73	75
16	275	2000	55	250	50	442	1012	179	0,007	0,012	0,01	130	77	90
17	275	2000	40	250	100	109	608	1047	0,008	0,015	0,01	115	60	89
18	275	2000	40	150	100	229	734	1420	0,008	0,014	0,011	117	62	82
19	275	2000	55	150	150	300	1038	1110	0,007	0,012	0,01	134	73	89
20	275	2000	55	150	50	1006	1231	1650	0,008	0,013	0,011	120	71	81
21	275	2000	55	250	150	183	1080	1120	0,007	0,012	0,01	133	73	91
22	275	2000	70	250	100	220	418	672	0,007	0,012	0,009	136	76	102
23	275	1000	55	200	150	313	982	1276	0,007	0,012	0,01	125	73	90
24	100	2000	55	200	50	562	731	1254	0,049	0,046	0,055	17	19	16
25	275	1000	55	150	100	1251	1238	1778	0,008	0,013	0,011	119	68	84
26	450	2000	55	200	50	850	1215	1610	0,007	0,012	0,012	123	77	79
27	450	2000	55	250	100	462	926	1291	0,007	0,011	0,011	128	84	87
28	275	3000	55	150	100	695	1072	1505	0,008	0,012	0,011	115	74	82

29	275	2000	55	200	100	1030	1421	1866	0,008	0,012	0,012	117	72	80
30	100	2000	55	200	150	188	652	721	0,042	0,047	0,047	20	18	18
31	275	2000	55	200	100	1003	1403	1819	0,008	0,014	0,011	117	66	82
32	275	2000	70	200	150	221	749	923	0,007	0,012	0,01	130	75	97
33	275	3000	55	250	100	330	940	1195	0,007	0,014	0,011	128	64	88
34	275	2000	70	200	50	530	669	1102	0,007	0,011	0,011	124	81	89
35	275	1000	70	200	100	742	800	1299	0,007	0,012	0,011	124	76	88
36	275	3000	40	200	100	140	560	944	0,009	0,017	0,01	101	52	92
37	275	3000	70	200	100	375	673	1056	0,007	0,012	0,011	125	73	89
38	275	2000	40	200	50	268	757	1414	0,009	0,014	0,011	104	62	86
39	275	1000	55	250	100	571	913	1329	0,007	0,012	0,011	122	77	89
40	275	1000	40	200	100	146	769	1359	0,009	0,013	0,011	106	68	88
41	450	2000	55	200	150	373	1324	1403	0,007	0,011	0,012	124	79	81
42	275	2000	55	200	100	1060	1464	1802	0,008	0,012	0,011	117	77	82
43	275	2000	40	200	150	86	753	995	0,008	0,013	0,01	111	71	90
44	100	2000	55	150	100	854	1012	1537	0,051	0,054	0,053	16	16	16
45	100	2000	55	250	100	399	699	1125	0,049	0,054	0,053	17	16	17
46	450	2000	55	150	100	1269	1444	1820	0,008	0,012	0,012	112	76	76
47	275	2000	55	200	100	1172	1644	1791	0,008	0,012	0,011	116	73	83
48	100	3000	55	200	100	480	845	1150	0,048	0,053	0,05	18	16	17
49	450	1000	55	200	100	1383	1596	1918	0,008	0,012	0,012	112	78	78
50	275	2000	70	150	100	656	725	974	0,007	0,011	0,01	123	84	94
51	100	2000	70	200	100	403	492	708	0,056	0,053	0,049	15	16	18
52	275	2000	55	200	100	1161	1555	1689	0,008	0,013	0,011	116	70	83
53	100	1000	55	200	100	807	857	1171	0,053	0,053	0,051	16	16	17
54	100	2000	40	200	100	153	531	680	0,039	0,049	0,045	22	17	19

Table S1: Values of funnel1 RF, collision RF transfer time $\Delta 3$ and $\Delta 6$ parameters and responses for the second DOE

DOE	Pre Pulse Storage (µs)	IonE (eV)	Collision Cell In (V)	A (8:2 FTOH)	A (N-MeFOSA)	A (N-MeFOSE)	Rp (8:2 FTOH)	Rp (N-MeFOSA)	Rp(N-MeFOSE)	FWHM (8:2 FTOH)	FWHM (N-MeFOSA)	FWHM (N-MeFOSE)
1	18	10	150	404	834	813	131	42	98	0,007	0,022	0,01
2	10	8	100	464	810	819	118	69	99	0,008	0,013	0,01
3	18	8	100	316	919	1037	113	67	94	0,008	0,014	0,01
4	14	6	100	744	1272	1381	118	78	91	0,008	0,012	0,01

5	14	8	150	842	1403	1412	130	81	93	0,007	0,011	0,01
6	10	10	150	576	953	684	133	82	105	0,007	0,011	0,009
7	14	10	100	556	1387	839	125	76	100	0,007	0,012	0,009
8	14	10	200	806	1314	1014	133	83	100	0,007	0,011	0,009
9	18	6	150	460	998	1217	120	75	94	0,008	0,012	0,01
10	14	8	150	872	1570	1309	130	80	98	0,007	0,011	0,01
11	14	6	200	873	1352	1690	122	82	91	0,008	0,011	0,01
12	10	6	150	602	925	1059	125	87	96	0,007	0,01	0,01
13	14	8	150	869	1555	1461	127	80	93	0,007	0,011	0,01
14	10	8	200	575	956	1082	130	88	96	0,007	0,01	0,01
15	18	8	200	491	1024	1224	131	81	94	0,007	0,011	0,01

Table S2: Values of pre pulse storage, ion E, collision cell in parameters and responses of the third DOE

VI. Chapter 2: Comparison of the performance of GC-APCI-TIMS-TOFMS and GC-EI-sector HRMS instruments to quantify trace levels of PBBs, PBDDs, PBDFs, PXDDs, PXDFs and PXBs in food samples

A. Introduction

1. Context

TEQFood (TF) is a project funded by the FPS public Health, Food chain safety and Environment and conducted by the University of Liège (ULiège) in collaboration with Sciensano. The objectives of this project were to determine the concentrations of polychlorinated dibenzo-p-dioxins and dibenzofurans (PCDD/Fs), polybrominated dibenzo-p-dioxins and dibenzofurans (PBDD/Fs), polychlorobiphenyls (PCBs), and mixed halogenated biphenyls (PXBs) in food available on the Belgian market; to estimate the dietary intake of these compounds by the Belgian population; to compare the obtained results with those of a previous study on selected persistent organic pollutants (POPs); and finally, to identify the most suitable analytical approach for assessing the concentrations of PCDD/Fs, PBDD/Fs, PCBs, and PXBs in food [1].

2. Previous study

Regarding the latter objective, a study was conducted to evaluate the capability of a modern ion mobility-mass spectrometry (IM-MS) system (timsTOF Pro 2, Bruker) to quantify trace levels of dioxins and PCBs in food samples, and to compare its performance with that of gas chromatography coupled to high-resolution sector mass spectrometry (GC-HRMS), which remains the reference technique for trace quantification of dioxins and PCBs in food samples [2].

In this study, three food samples were analyzed using a gas chromatography-atmospheric pressure chemical ionization-trapped ion mobility spectrometry-time-of-flight mass spectrometry (GC-APCI-TIMS-TOFMS) instrument. The results demonstrated that the performance of the GC-APCI-TIMS-TOFMS method was comparable to, or slightly below, that of the GC-HRMS method for the determination of PCDD/Fs and PCBs. Moreover, it was demonstrated that ion mobility step enabled an enhancement in compound identification, through the use of collision cross-section (CCS) values, which provide an additional identification parameter in targeted analyses, and to enhance peak capacity, as ion mobility improves the separation of co-eluting, isobaric, and isomeric compounds [2].

Moreover, IM-MS enables non-targeted analysis (NTA), unlike Gas chromatography coupled to electron ionization sector high-resolution mass spectrometry (GC-EI-sector HRMS), which is restricted to predefined targets. This capability is particularly valuable for the detection of unknown pollutants and allows the simultaneous analysis of multiple contaminant classes within a single analytical run [2].

3. POPs

The continuation of this work concerns other POPs that have been less studied, despite their recognition as environmental contaminants for many years [1].

Polybrominated biphenyls (PBBs) (Figure 1) are legacy brominated flame retardants (BFRs) as well as by-products arising from the synthesis and degradation of polybrominated diphenyl ethers (PBDEs). They exhibit the four characteristic properties of POPs, as described in Chapter 1, which justifies their inclusion in the Stockholm Convention since 2009 [3].

Polybrominated dibenzo-p-dioxins and dibenzofurans (PBDD/Fs) (Figure 1) are unintentionally generated during processes such as waste incineration, industrial manufacturing, environmental degradation, and as impurities in BFR formulations [4,5,6]. They are currently not subject to specific regulatory control, and only a limited number of toxicological studies have been conducted. Nevertheless, available data indicate that their toxicological properties are comparable to those of their polychlorinated analogues [5].

Similarly, mixed halogenated dioxins and furans (PXDDs and PXDFs, where X represents mixed chlorine and bromine substitutions) (Figure 1), as well as mixed halogenated biphenyls (PXBs) (Figure 1), are produced during the incineration of materials containing both chlorinated and brominated compounds. These compounds are likewise unregulated, and toxicological investigations suggest that their toxicity is of a similar magnitude to that of the corresponding polychlorinated analogues [4,5].

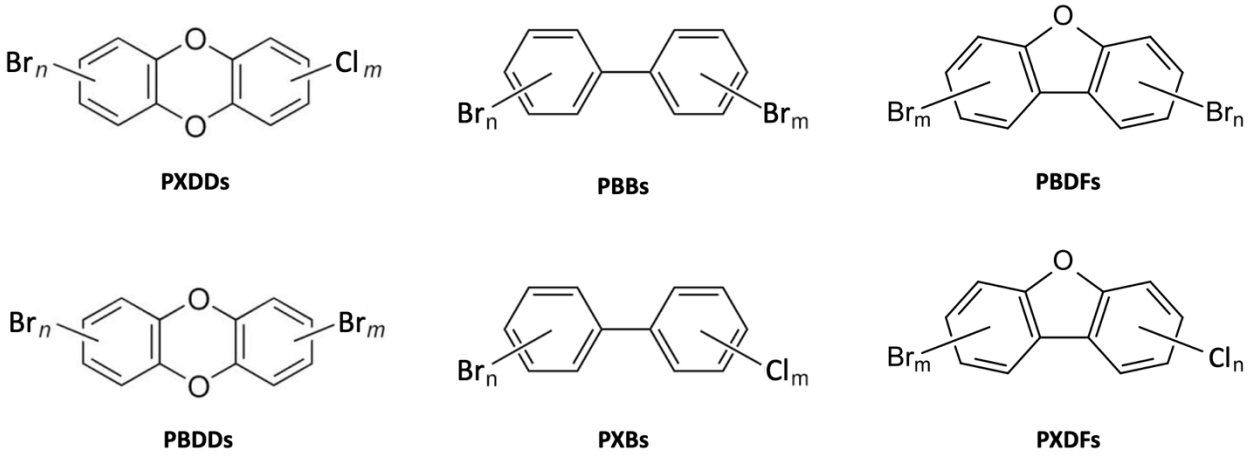

Figure 1: Chemical structures of PXDD/Fs, PBBs, PXBs and PBDD/Fs

Overall, considerably fewer studies have focused on mixed halogenated compounds than on brominated dioxins and furans, underscoring the need for further research to elucidate environmental fate, quantification in environmental and food matrices, and toxicological significance.

B. Objectives

The objectives of this chapter are divided into two main parts.

Part 1 aims to optimize the parameters on a timsTOF Flex instrument using volatile siloxanes compounds originating from the GC column bleed. These optimised parameters will be compared to those previously obtained on a timsTOF Pro 2 instrument, which contains a different IM cell. A secondary objective will be to determine the IM resolving power (Rp) on the Flex instrument using the sliding windows in ion mobility (SWIM) approach and to compare it with that obtained on the Pro2 instrument.

Part 2 aims to compare the quantification results of emerging (brominated and mixed) POPs obtained using the GC-APCI-TIMS-TOFMS method with those obtained using the reference GC-EI-sector HRMS method on various food matrices prepared in the frame of TEQfood project. The second objective of this part will be to perform a suspect screening analysis on the analyses TEQfood sampled in order to the presence of additional halogenated pollutants.

C. Materials and methods

1. Chemicals

All congeners of PBDD/Fs, PBBs, PXDD/Fs, and PXBs (listed in Table S1, in Supplementary Information (SI)) were quantified using their own 13C-labelled internal standards, or corresponding 13C-labelled analogues when the specific standard was not available, according to the isotope dilution method. Both native and 13C-labelled standards were purchased from Wellington (Ontario, Canada).

For calibration, five-level calibration curves were prepared, with concentration details provided in Table S2 (SI). All solvents used were of the highest purity, suitable for the analysis of trace contaminants (Biosolve, Dieuze, France).

2. Sample preparation

Five samples were selected from previous studies based on their concentrations of PBDD/F and PBB congeners. These samples included beef meat (internal code E2222), chicken meat (E2159), free-range chicken eggs (E2242), herring (E2386), and organic eggs (E2241).

Sample preparation procedures followed those described by Muller et al [2].
To reconstitute the pollutants in solution, 8 µL of nonane were added to the dioxin fractions (except for the beef meat sample, where 40 µL of nonane were added) and 20 µL to the PCB fractions. All samples were then placed in an ultrasonic bath for 30 min.

3. Instrumentation

a) GC-APCI-TIMS-TOFMS

Measurements were performed on a commercial timsTOF Flex mass spectrometer (Bruker, Bremen) equipped with a Scion 456-GC connected to an APCI source for sample introduction and ionization (GC- APCI II, Bruker, Bremen).

For the dioxin fraction, the samples were injected manually in programmated temperature vaporization (PTV) mode (injection temperature 80°C, 5 µL) and for the PCB fraction, injections were conducted automatically in splitless mode (injection temperature 275 °C, 1 µL). The GC column was a low polarity Rxi-5Sil MS column (30 m × 0.25 mm × 0.25 µm, Restek). Helium (grade 6.0, Air Liquide, Belgium) was used as the carrier gas.

Ion mobility separations were performed by trapped ion mobility.

b) GC-EI-sector HRMS

Measurements were carried out using an Autospec sector mass spectrometer (Waters, Manchester, UK) coupled to an Agilent 7890 gas chromatograph (Agilent Technologies, Palo Alto, CA, USA) [7]. Two different GC columns were used depending on the analyzed fraction.

For the dioxin fraction, a 50 m J&W VF-5ms column was employed, and samples were injected automatically in PTV mode (injection temperature: 80 °C; injection volume: 5 µL). For the PCB fraction, a 25 m Trajan HT8 column was used, and samples were injected automatically in splitless mode (injection temperature: 275 °C; injection volume: 2 µL) [2].

EI at 35 eV was used, and HRMS analyses were performed in single ion monitoring (SIM) mode.

4. Methods

For GC-timsMS analysis, data were processed using DataAnalysis software (Bruker, version 5.3). Parameter optimization on the timsTOF Flex instrument was based on the signal intensity of five siloxane extracted ion chromatograms (EICs). For sample analysis, peak integration was based on the area of the ion mobility peaks. Internal recalibration of *m/z* and ion mobility was performed using siloxanes originating from column bleed prior to data acquisition and data processing.

D. Results and discussion

The previous study was performed using a timsTOF Pro 2 mass spectrometer (Bruker, Bremen), whereas the present study was conducted using a timsTOF Flex mass spectrometer (Bruker, Bremen). The primary difference between these two instruments lies in the size of the TIMS cell, which is larger in the timsTOF Flex. Consequently, the method developed in the previous study required adaptation for use with the timsTOF Flex instrument.

Part 1

1. Parameter optimization on a timsTOF Flex instrument

For the adaptation of the method, the siloxanes originating from GC-column bleeding were used because as they are widely available ions possessing a large range of masses and ion mobilities. Five characteristic ions were monitored: 223 m/z, 281 m/z, 355 m/z, 429 m/z and 503 m/z.

This adaptation was carried out through classical parameter optimization on the GC-APCI-TIMS-TOFMS system. The injector and GC oven temperatures were fixed at 140 °C, and the helium flow at 1 mL/min. Thirteen parameters were optimized: Funnel1 RF, Funnel2 RF, multipole RF, collision RF, transfer time, pre pulse storage, collision energy, ion energy, Δ3, Δ4, Δ6, collision cell in, and accumulation time (described in Chapter 1, Section D.2 "Optimization of TIMS and TOF Parameters"). Each parameter was varied individually, with its value increased every 40 s and finally returned to its initial value to stabilize the signal (see Table 1).

Parameters	Initial	Final	Step
Funnel1 RF (Vpp)	100	500	50
Funnel2 RF (Vpp)	100	600	100
Multipole RF (Vpp)	200	1200	200
Collision RF (Vpp)	500	4000	500
Transfer time (µs)	30	150	20
Pre Pulse storage (µs)	2	14	2
Collision E (eV)	2	14	2
Ion E (eV)	2	16	2
Δ3 (V)	20	400	20
Δ4 (V)	20	400	20
Δ6 (V)	20	200	20
Collision Cell In (V)	50	300	50

Table 1: Initial and final parameter value optimized during the classical optimization with their corresponding step of increasing

The optimal parameter values were selected based on the EIC intensity of each siloxane. As an example, the optimization of the multipole RF is presented here.

The EICs of the siloxanes were examined (Figure 2). The signal of the first siloxane (223 m/z) decreased at multipole RF values above 800 V, and the signal of the second (281 m/z) decreased above 1000 V. Therefore, the optimal value was determined to lie between 200 V and 600 V. The lowest value that ensured a stable signal was favoured, and the optimal multipole RF was set to 200 V.

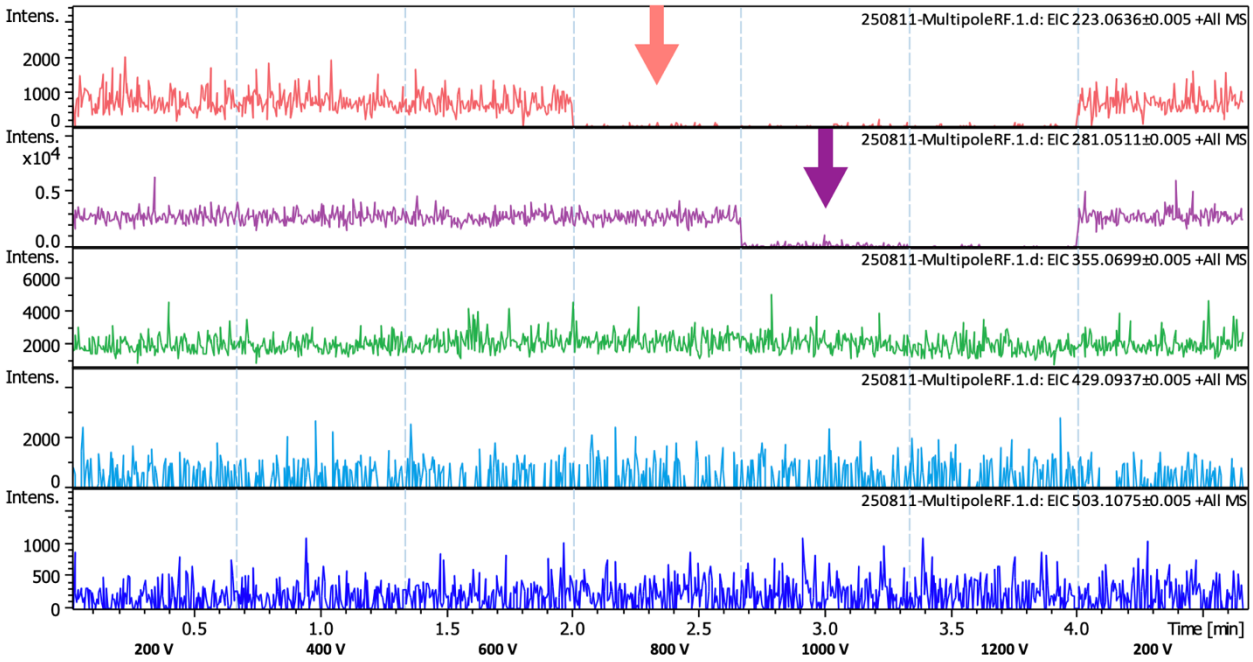

Figure 2: EICs corresponding to the siloxanes for the optimization of multipole RF parameter varying from 200 V to 1200 V and ending to initial value (200 V)

All parameter values obtained from the classical optimization are summarized in Table 2 and compared with the Pro2 optimal settings. The main difference was that RF amplitudes were slightly higher in the Flex method compared to the Pro2 method. This is consistent with the fact that the TIMS cell is larger in the timsTOF Flex instrument.

Parameters	Pro2	Flex
Funnel1 RF (Vpp)	250	350
Funnel2 RF (Vpp)	200	200
Multipole RF (Vpp)	200	250
Collision RF (Vpp)	800-1200	1000-1500
Transfert time (µs)	55	55
Pre Pulse storage (µs)	7-11	8-10
Collision E (eV)	8-10	6-10
Ion E (eV)	8-10	6-10
Δ3 (V)	50	100
Δ4 (V)	20	20

Δ6 (V)	100	100
Collision Cell In (V)	190	150

Table 2: comparison of Pro2 and Flex parameters values

Accumulation time was optimized by varying it from 5 to 250 ms while keeping the total analysis time constant at 250 ms, and performing the experiment at four oven temperatures: 140 °C, 200 °C, 280 °C and 300 °C. The plots showed that the three highest-mass siloxanes began to saturate at 300 °C around an accumulation time of 150 ms (see in Figure 3). By comparison, the Pro2 cell saturated around 100 ms. As with the RF behavior, this difference is attributed to the larger cell volume of the Flex instrument.

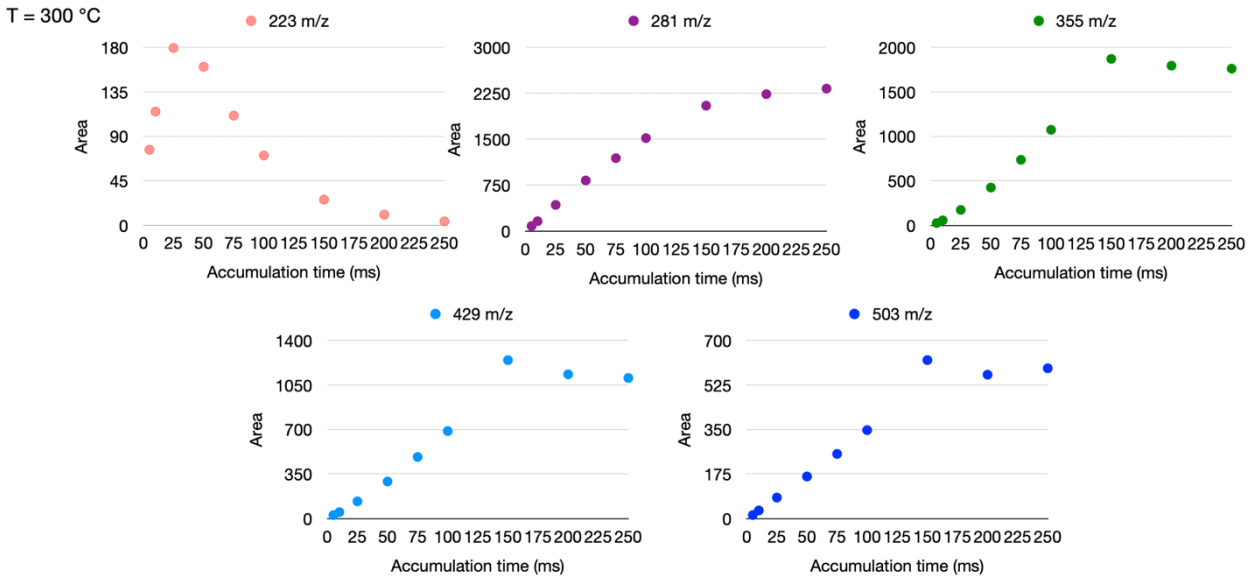

Figure 3: Plots of the areas of the five siloxanes normalized by the duty cycle vs accumulation time (ms)

2. Evaluation of IM resolving power

Rp of the Flex TIMS cell was evaluated and compared to the Rp of the Pro2 using the SWIM method and a standard mixture of PCDDs, PCDFs and PCBs (listed in Figure S1, SI).

For the Pro2, the mean resolving power obtained by Muller *et al.* in 2023 from a triplicate experiment was 207.

For the Flex, Rp was measured using the same method. The experiment yielded an Rp of 148, significantly lower than that of the Pro2 (see in first plot of Figure 4). When the optimized parameters were applied, the resolving power further decreased to 133 (see in second plot of Figure 4). This decrease may be explained by the higher RF values: stronger radial confinement compresses the ion packet, increasing lateral diffusion and therefore decreasing Rp.

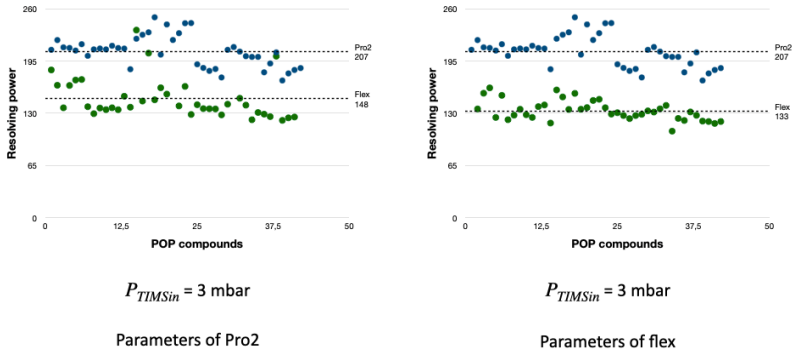

Figure 4: Plots of the Rp comparison between the Pro2 (blow) and Flex (green)

To verify the current performance of the Pro2, a new Rp measurement was carried out. The Rp had significantly decreased to 166 (first plot of the Figure 5). This drop may be due to fouling of the TIMS cell or an instrument malfunction that occurred in 2025.

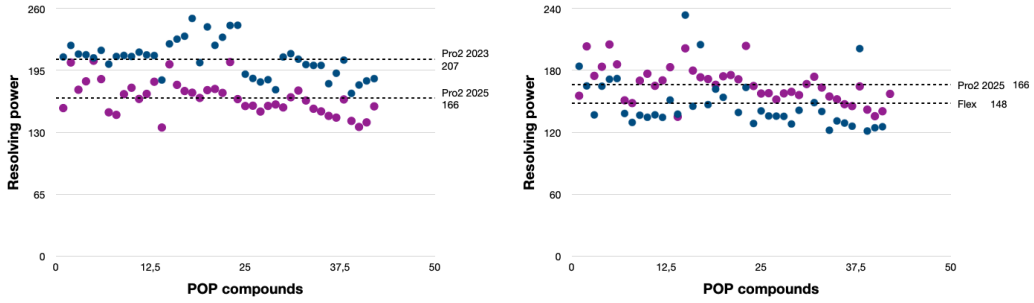

Figure 5: Plots of the Rp comparison between the Pro2 2023 (blow) and Pro2 2025 (purple) in the first plot and the Pro2 2025 (purple) and Flex (blow) in the second plot

This updated Rp was compared to that of the Flex (second plot of the Figure 5). Although the Pro2 performance had declined, its resolving power remained higher than that of the Flex. This difference could be explained by the larger TIMS cell of the Flex and the fact that, in this instrument, the TIMS cell is coupled to a Matrix-Assisted Laser Desorption/Ionization (MALDI) ion source, which may influence the pression inside the cell and in consequently, its resolving power.

Part 2

1. Calibration

A five-point calibration was performed using a calibration mix containing 8 PBBs, 11 PBDDs, 13 PBDFs, 8 PXBs, 4 PXDDs, and 7 PXDFs (listed in Table S1, SI). Concentrations ranged from approximately 1 pg/µL to 100 pg/µL to assess the linearity of the method using the GC-APCI-timsTOF Flex instrument (listed in Table S2, SI).

The relative response factor (RRF) was determined at each calibration level based on the integrated peak areas of the compounds in their extracted ion mobilograms (EIMs), and the mean RRF was calculated from the five calibration points. Subsequently, the relative standard deviation

(RSD, %) of the mean RRF and the absolute error relative to the mean RRF were calculated. To ensure acceptable linearity, the meanRSD was required to remain below 10%, and the absolute error relative to the mean RRF was required not to exceed 20%, as shown in Figure 6. When the 20% threshold was exceeded, the corresponding calibration point was excluded from the calculation of the mean RRF, as illustrated in Figure 7, where the first calibration point was omitted.

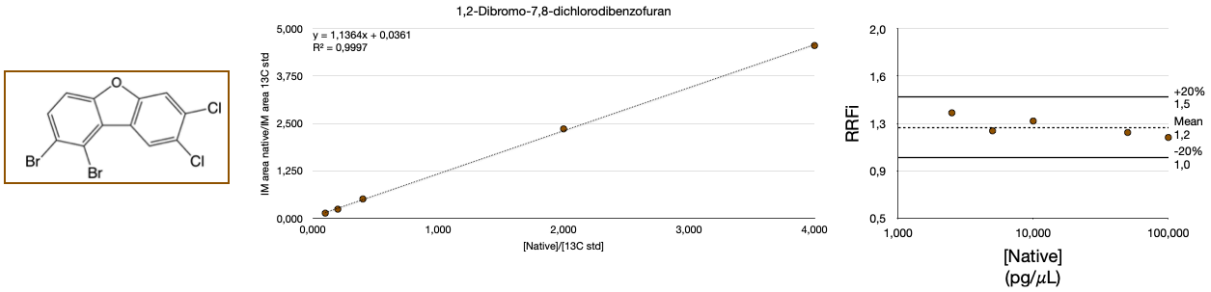

Figure 6: Calibration curve and determination of RRF for the 1,2-Dibromo-7,8-Dichlorodibenzofuran

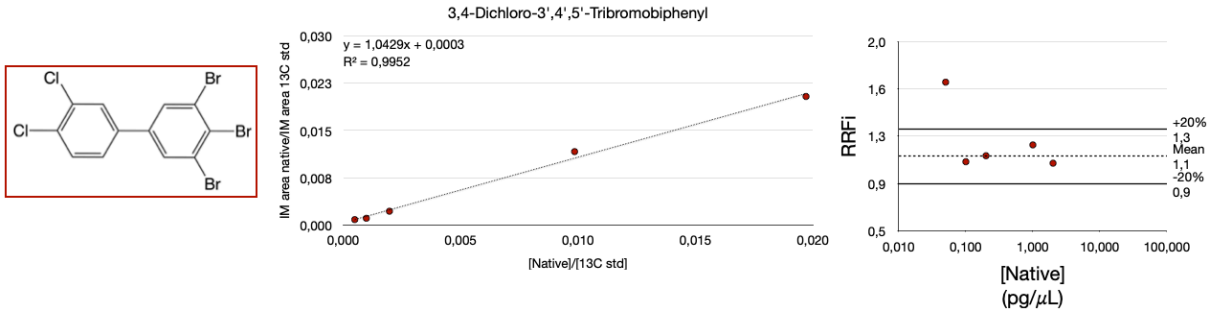

Figure 7: Calibration curve and determination of RRF for the 3,4-Dichloro-3',4',5'-Tribromobiphenyl

To validate the RRF values determined using GC-APCI-TIMS-TOFMS (timsTOF Flex, Bruker), they were compared with values previously obtained in 2024 using GC-APCI-TIMS-TOFMS (timsTOF Pro2, Bruker) (see Table S3, SI). Overall, the values of RRF were similar and the same issues observed in the previous calibration were also present in the new calibration. In particular, the same interference issue prevented the calculation of RRFs for 2,3,7,8-TBDF and 4'-monobromo-3,3',4,5-tetrachlorobiphenyl. Because these compounds eluted at the same retention time as other compounds, it was not possible to correctly integrate the chromatographic peak area to generate the mobilogram, as shown in Figure 8. Consequently, the calculated RRFs were inaccurate. This observation is consistent with the fact that the same GC column was used for both the timsTOF Flex and timsTOF Pro2 instruments.

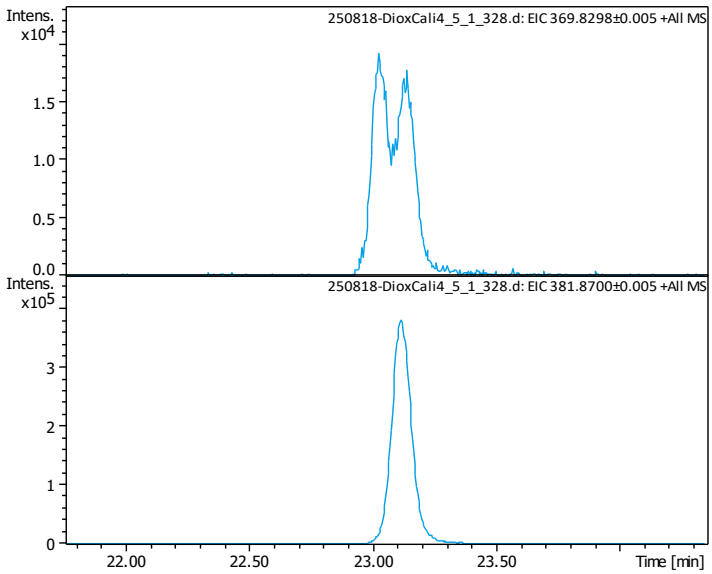

Figure 8: EIC of 4'-Monobromo-3,3',4,5-Tetrachlorobiphenyl (top) and 13C-labelled corresponding compound (bottom)

Hexabromodibenzo-p-dioxins (HxBDDs) were also not detected, which may indicate that they were not present in the calibration mixture. An additional issue was observed for 2,3,7,8-TBDD: the native concentration had to be increased by a factor of 10 to obtain a plausible RRF. Even after this adjustment, the mean RRF value (3.75) remained significantly higher than the value obtained in 2024 (0.89). Finally, 4'-monobromo-3,3',4,5,5'-pentachlorobiphenyl was also not detected, and the cause of this absence could not be determined.

2. Sample analysis

a) Targeted analysis of dioxin fraction

During sample preparation, each sample was divided into two fractions: dioxins and PCBs. For the dioxin fraction, three matrices (beef meat (E2222), chicken meat (E2159), and free-range chicken eggs (E2242)) were analyzed. The results of these analyses are summarized in Table 3 and highlight three main observations:

1. **Higher concentrations observed with GC-APCI-TIMS-TOFMS:**

The concentrations quantified by GC-APCI-TIMS-TOFMS were consistently higher than those obtained by GC-EI-sector HRMS. This discrepancy could be attributed to the low signal intensity obtained with the TIMS instrumentation (on the order of 10^3), which resulted in greater peak area calculation uncertainty (Table 3). Another possible explanation could lie in the quantification approach: concentrations were determined based on mobility peak integration. However, Muller *et al.* [7] demonstrated that concentration determination was more accurate when based on integrating chromatographic peaks filtered by ion mobility.

It should be noted that this trend was observed for all compounds except two DiBDF congeners, for which concentrations measured by GC-APCI-TIMS-TOFMS were lower than those obtained by sector HRMS. This behavior may be explained by the higher volatility of these compounds, leading to partial losses during storage or sample handling, as also suggested for PBB3 (see below).

2. **Non-detection of low-level pollutants:**
Certain pollutants detected by sector HRMS were not detected by GC-APCI-TIMS-TOFMS. Nevertheless, their concentrations were relatively low (below 1 pg/g fat). For instance, 4-MoBDF (Table 3) was quantified at 0.18 pg/g fat by sector HRMS. This is likely due to the lower sensitivity of the GC-APCI-TIMS-TOFMS instrument compared to the GC-EI-sector HRMS combined with the fact that half of the sample extract had already been consumed during the sector HRMS analysis. Moreover, the samples were diluted by a factor of 1,4 (except for the beef meat sample, which was diluted by a factor of 3) to reconstitute the pollutants in solution, as described in the *Materials and Methods* section. Therefore, the concentrations were most likely below the LOQ.
3. **Undetected high-concentration compounds:**
Four compounds (1-MoBDD, 7B23CDD, 2B378CDD, and PBB3) were not detected, despite having been previously identified by GC-EI-sector HRMS analyses at relatively high concentrations (up to 100 pg/g fat).

For 1-MoBDD, this could be explained based on the results from the calibration curve, as the first three calibration points were not detected, that suggesting a relatively high LOQ for this compound. The signal was only observed from the fourth calibration point, corresponding to a concentration of 50 pg/µL (equivalent to 13.16 pg/g fat). Although the concentration measured by sector HRMS in sample E2159 exceeded this value, the additional dilution factor of 1.4 applied prior to GC-APCI-TIMS-TOFMS analysis likely reduced the analyte concentration below the LOQ.

For the remaining compounds, measured concentrations were above the LOQ. However, PBB3 is a highly volatile compound and may have been partially lost during storage or during the additional sample preparation steps following the initial sector HRMS analysis. The mixed dioxins were present at relatively low levels in the samples, which may explain why 7B23CDD and 2B378CDD were not detected in the Flex method.

	E2159		E2242		E2222	
Composite sample	**Flex**	**Sector**	**Flex**	**Sector**	**Flex**	**Sector**
PBDD/Fs	**pg/g fat**	**pg/g fat**	**pg/g fat**	**pg/g fat**	**pg/g fat**	**pg/g fat**
4-MoBDF	12,92 (3051%)	0,41	22,38 (6300%)	0,35	/	0,18
24-DiBDF	4,55 (34%)	6,95	2,9 (98%)	150,44	2,68 (31%)	3,92
28-DiBDF	28,65 (35%)	44,50	31,88 (95%)	639,86	17,01 (26%)	23,01
138-TrBDF	11,67 (6042%)	0,19	10,05 (3500%)	0,28		
247-TrBDF	9,64 (6785%)	0,14	17,03 (8900%)	0,19		
2468-TeBDF					5,92 (29500%)	0,02
123478-HxBDF	7,04 (4600%)	0,15				
1234678-HpBDF	/	0,18				
1-MoBDD	/	26,31	/	8,53	/	12,84
12478-PeBDD	/	0,19				
PBBs	**pg/g fat**	**pg/g fat**	**pg/g fat**	**pg/g fat**	**pg/g fat**	**pg/g fat**
PBB-3	/	2,73	/	0,86	/	2,66
PBB-15	42,73 (138%)	17,90	61,512 (5000%)	1,20	26,17 (156%)	10,19
PXDD/Fs	**pg/g fat**	**pg/g fat**	**pg/g fat**	**pg/g fat**	**pg/g fat**	**pg/g fat**
7-MoB-23-DiCDD	/	76,55	/	127,87	/	30,13
2-MoB-378-TrCDD	/	3,02	/	18,16	/	2,53
PXBs	**pg/g fat**	**pg/g fat**	**pg/g fat**	**pg/g fat**	**pg/g fat**	**pg/g fat**
34-B-3'4'-CB (77)	/	0,02				
4'-B-33'45-CB (126)	/	0,01				
4'-B-33'455'-CB (126)	/	0,01				
3'4'5'-B34-CB (126)	/	0,02				

Table 3: Concentration of targeted compounds in dioxin fraction of chicken meat (E2159), free-range chicken eggs (E2242) and beef meat (E2222) samples with the relative difference between sector and flex in parentheses and the colored cases that correspond to undetected high-concentration compounds in Flex

b) Suspect screening analysis of dioxin fraction

A suspect screening analysis of these samples was also conducted. Each additional peak was scrutinized for mass accuracy, isotopic pattern, and CCS to ensure that the signals were correctly attributed. As highlighted in Table S4, SI, the pollutants were tentatively identified through suspect screening were predominantly PBDFs, including TriBDF and PeBDF congeners, as well as DiBB and MoBrTetraClB compounds.

c) Targeted analysis of PCB fraction

For the PCB fraction, five matrices were analyzed: beef meat (E2222), chicken meat (E2159), free-range chicken eggs (E2242), haring (E2386), and organic eggs (E2241). The results are summarized in Table 4. Overall, all pollutants detected by GC-EI-sector HRMS were also identified by GC-APCI-TIMS-TOFMS, with two exceptions:

1. **PBB153 in organic eggs (E2241) and 4'B-233'4-CB(105) in haring (E2386):**

This discrepancy could be explained similarly to the second observation made for the dioxin results. The concentration of PBB153 and 4'B-233'4-CB(105) measured by GC-EI-sector HRMS was low (0,35 pg/g fat and 0,2 pg/g fat, respectively), and likely falls below the sensitivity threshold of

the GC-APCI-TIMS-TOFMS instrument. Furthermore, these samples were also diluted by a factor of 1,2 to reintroduce the pollutants into solution, as described in the Materials and Methods section.

2. **PBB18 in beef meat (E2222):**

This result appears inconsistent, as the concentration determined by GC-EI-sector HRMS was relatively high (52.83 pg/g fat). However, this congener is very volatile and could have been lost.

	E2159		E2242		E2222		E2241		E2386	
Composite sample	**Flex**	**Sector**	**Flex**	**Sector**	**Flex**	**Sector**	**Flex**	**Sector**	**Flex**	**Sector**
PBBs	**pg/g fat**	**pg/g fat**	**pg/g fat**	**pg/g fat**	**pg/g fat**	**pg/g fat**	**pg/g fat**	**pg/g fat**	**pg/g fresh weight**	**pg/g fresh weight**
PBB-18					/	52,83				
PBB-52									108,3 (3000%)	3,49
PBB-101									37,13 (4000%)	0,89
PBB-153	0,40 (90%)	0,21	0,44 (16%)	0,38	0,93 (51%)	1,90	/	0,35	6,97 (1000%)	0,65
PBB-206	/	6,82	/		/		/		/	
PBB-209	/	23,18	/	27,38	/		/		/	
PXBs	**pg/g fat**	**pg/g fat**	**pg/g fat**	**pg/g fat**	**pg/g fat**	**pg/g fat**	**pg/g fat**	**pg/g fat**	**pg/g fresh weight**	**pg/g fresh weight**
4'-B-2345-CB (114)	6,60 (178%)	2,37	9,52 (6250%)	0,15	2,60 (830%)	0,28	5,08 (150%)	2,03	4,612 (430%)	0,87
4'-B-233'4-CB (105)									/	0,20

Table 4: Concentration of targeted compounds in dioxin fraction of chicken meat (E2159), free-range chicken eggs (E2242) and beef meat (E2222), haring (E2386), and organic eggs (E2241) samples with the relative difference between sector and flex in parentheses and the colored cases that correspond to undetected compounds in Flex

In general, the concentrations quantified using GC-APCI-TIMS-TOFMS (Table 4) were systematically higher than those obtained with GC-EI-sector HRMS, in some cases by up to two orders of magnitude. This overestimation may again be attributed to the low signal intensity (on the order of 10^3), which increases the uncertainty associated with quantification.

Additionally, in the GC-APCI-TIMS-TOFMS analyses, PBB206 and PBB209 were not detected due to limitations in the GC temperature program used on the TIMS instrument, which was not optimized for these higher-molecular-weight congeners.

d) Suspect screening analysis of PCB fraction

A suspect screening analysis of these samples was also conducted. Each additional peak was carefully examined for mass accuracy, isotopic pattern, and CCS in order to ensure correct signal attribution. The pollutants tentatively identified through suspect screening were predominantly PBDEs. Overall, a similar PBDE pattern was observed in all samples, sometimes with significant signal intensities. The most contaminated sample was haring (E2386), in which 34 PBDEs, 20 PBBs, and 4 PXBs were tentatively detected (see the list in Table S5, SI).

3. Benefits of the additional IM separation

Nonetheless, TIMS adds a supplementary separation dimension that allows co-eluting compounds to be distinguished. For example, DiBDFs (325.8760 m/z) and PeCB (325.8799 m/z) are isomers that co-eluted but were successfully separated based on their differing CCS values (see Figure S1, SI).

In the dioxin fraction, since the injections were performed manually, the retention times differed from those in the calibration. However, CCS values could be used as an additional criterion to confirm the identity of a specific targeted or suspect compound. Overall, the GC-APCI-TIMS-TOFMS system demonstrated its suitability for suspect screening, as many additional compounds beyond the targeted analytes were detected, particularly, in PCB Fraction.

E. Intermediate conclusion and perspectives

This study evaluated the performance of the GC-APCI-timsTOF Flex-MS system for the analysis of PBDD/Fs, PBBs, PXDD/Fs, and PXBs in various food matrices and compared it with the reference GC-EI-sector HRMS method. Overall, GC-APCI-TIMS-TOFMS showed lower sensitivity, leading to the non-detection of some congeners present at very low concentrations. In addition, quantified concentrations were often over-estimated.

However, the technique offers significant advantages: the additional separation provided by ion mobility improves the resolution of co-eluting compounds and adds an extra identification parameter through CCS values. Most importantly, GC-APCI-TIMS-TOFMS proved highly effective for suspect screening, enabling the tentative detection of numerous additional compounds, particularly PBDEs in PCB fraction.

Thus, while methodological improvements are required to reach sensitivity levels comparable to GC-EI-sector HRMS, GC-APCI-TIMS-TOFMS represents a promising tool for expanded and screening POP analysis in food. Future work should focus on optimizing quantification using mobility-filtered chromatographic peaks, performing a more comprehensive method validation and establishing additional calibration curves (particularly for PBDEs).

F. References

[1] Health, FPS Public. 'Occurrence and Exposure to Dioxins, Furans and Halogenated Biphenyls in Foodstuffs | FPS Public Health'. Accessed 8 January 2026. https://www.health.belgium.be/en/research/occurrence-exposure-dioxins-furans-halogenated-biphenyls-foodstuffs.

[2] Muller, Hugo B., Georges Scholl, and Gauthier Eppe. 'Gas Chromatography–Trapped Ion Mobility Mass Spectrometry: A Highly Specific and Ultra-Sensitive Platform for Quantifying Sub-Ppt Levels of Dioxins and PCBs in Food'. *Chemosphere* 385 (September 2025): 144557. https://doi.org/10.1016/j.chemosphere.2025.144557.

[3] Falandysz, Jerzy, Frankie Smith, and Alwyn R. Fernandes. 'Dioxin-like Polybrominated Biphenyls (PBBs) and Ortho-Substituted PBBs in Edible Cod (Gadus Morhua) Liver Oils and Canned Cod Livers'. *Chemosphere* 248 (June 2020): 126109. https://doi.org/10.1016/j.chemosphere.2020.126109.

[4] Pratt, Iona, Wayne Anderson, Dominique Crowley, et al. 'Brominated and Fluorinated Organic Pollutants in the Breast Milk of First-Time Irish Mothers: Is There a Relationship to Levels in Food?' *Food Additives & Contaminants: Part A* 30, no. 10 (2013): 1788–98. https://doi.org/10.1080/19440049.2013.822569.

[5] Zacs, Dzintars, Jekaterina Rjabova, Alwyn Fernandes, and Vadims Bartkevics. 'Brominated, Chlorinated and Mixed Brominated/Chlorinated Persistent Organic Pollutants in European Eels (Anquilla Anquilla) from Latvian Lakes'. *Food Additives & Contaminants: Part A* 33, no. 3 (2016): 460–72. https://doi.org/10.1080/19440049.2015.1136436.

[6] Fromme, Hermann, Veronika Fuchs, Michael Albrecht, et al. 'Polychlorinated Dioxins and Dibenzofurans (PCDD/F), Polybrominated Dioxins and Dibenzofurans (PBDD/F), Polychlorinated Biphenyls (PCB), Polybrominated Diphenyl Ethers (PBDE), and per- and Polyfluoroalkyl Substances (PFAS) in German Breast Milk Samples (LUPE 8)'. *Science of The Total Environment* 825 (June 2022): 154066. https://doi.org/10.1016/j.scitotenv.2022.154066.

[7] Focant, Jean-François, Catherine Pirard, Gauthier Eppe, and Edwin De Pauw. 'Recent Advances in Mass Spectrometric Measurement of Dioxins'. *Journal of Chromatography A* 1067, (2005): 265–75. https://doi.org/10.1016/j.chroma.2004.10.095.

G. Supporting information

PBBs	PBDDs	PBDFs	PXBs	PXDD/Fs
PBB 3	1-MoBDD	4-MoBDF	4'-Bromo-2,3',4,5-Tetrachlorobiphenyl	7-Bromo-2,3-dichlorodibenzo-p-dioxin
PBB 15	2,3,7-TriBDD	2,4-DiBDF	4'-Bromo-2,3,3',4-Tetrachlorobiphenyl	2-Bromo-3,7,8-trichlorodibenzo-p-dioxin
PBB 18	1,3,7,8-TBDD	2,8-DiBDF	4'-Bromo-3,3',4,5-Tetrachlorobiphenyl	2-Bromo-1,3,7,8-tetrachlorodibenzo-p-dioxin
PBB 52	1,2,3,4-TBDD	1,3,8-TriBDF	4'-Bromo-2,3,3',4,5-Pentachlorobiphenyl	2,3-Dibromo-7,8-dichlorodibenzo-p-dioxin
PBB 101	2,3,7,8-TBDD	2,4,7-TriBDF	4'-Bromo-3,3',4,5,5'-Pentachlorobiphenyl	8-Bromo-2,3-dichlorodibenzofuran
PBB 153	1,2,4,7,8-PeBDD	2,3,4-TriBDF	3,4-Dibromo-3',4'-Dichlorobiphenyl	8-Bromo-2,3,4-trichlorodibenzofuran
PBB 180	1,2,3,7,8-PeBDD	2,4,6,8-TBDF	3,4-Dibromo-3',4',5'-Trichlorobiphenyl	3-Bromo-2,7,8-trichlorodibenzofuran
PBB 194	1,2,3,4,7,8-HxBDD + 1,2,3,6,7,8-HxBDD	1,2,7,8-TBDF	3,4-Dichloro-3',4',5'-Tribromobiphenyl	4-Bromo-2,3,7,8-tetrachlorodibenzofuran
PBB 206	1,2,3,7,8,9-HxBDD	2,3,7,8-TBDF		1,2-Dibromo-7,8-dichlorodibenzofuran
PBB 209	1,2,3,4,6,7,8-HpBDD	1,2,3,7,8-PeBDF		2,3-Dibromo-7,8-dichlorodibenzofuran
	OBDD	2,3,4,7,8-PeBDF		1,3-Dibromo-2,7,8-trichlorodibenzofuran
		1,2,3,4,7,8-HxBDF		
		1,2,3,4,6,7,8-HpBDF		

Table S1: List of targeted compounds for the TF analysis

Content	Cali					13C	
	C1 [pg/µl]	C2 [pg/µl]	C3 [pg/µl]	C4 [pg/µl]	C5 [pg/µl]	Content	C [pg/µl]
3-MoBB	0,2500	0,5000	2,0000	10,0000	20,0000	4B-3,3,4,5-CB	48,85

15-DiBB	0,2500	0,5000	2,0000	10,0000	20,0000	4B-3,3,4,5-CB	48,85
18-TriBB	0,2500	0,5000	2,0000	10,0000	20,0000	52-BB	50
52-TBB	0,2500	0,5000	2,0000	10,0000	20,0000		50
101-PBB	0,5000	1,0000	4,0000	20,0000	40,0000	52-BB	50
153-HBB	0,5000	1,0000	4,0000	20,0000	40,0000		100
180-HpBB	0,5000	1,0000	4,0000	20,0000	40,0000	153-BB	100
194-OBB	0,5000	1,0000	4,0000	20,0000	40,0000		100
206-NoBB	1,2500	2,5000	10,0000	50,0000	100,0000	194-BB	100
209-DBB	1,2500	2,5000	10,0000	50,0000	100,0000		250
1-MoBDD	2,500	5,000	10,000	50,000	100,000	2,3,7,8-TBDD	4,95
2,3,7-TriBDD	2,500	5,000	10,000	50,000	100,000	2,3,7,8-TBDD	4,95
1,3,7,8-TBDD	2,500	5,000	10,000	50,000	100,000	2,3,7,8-TBDD	4,95
1,2,3,4-TBDD	2,500	5,000	10,000	50,000	100,000	2,3,7,8-TBDD	4,95
2,3,7,8-TBDD	0,0125	0,0250	0,0500	0,2500	0,4999		4,95
1,2,4,7,8-PBDD	2,500	5,000	10,000	50,000	100,000	1,2,3,7,8-PBDD	5
1,2,3,7,8-PBDD	0,0250	0,0501	0,1001	0,5005	1,0010		5
1,2,3,4,7,8-HBDD	0,0750	0,1500	0,2999	1,4995	2,9990	1,2,3,4,7,8-HBDD	12,55
1,2,3,6,7,8-HBDD	0,0750	0,1500	0,3000	1,5000	3,0000		12,5
1,2,3,7,8,9-HBDD	0,0751	0,1501	0,3002	1,5010	3,0020		25,05
OBDD	0,1250	0,2499	0,4998	2,4990	4,9980		37,5
4-MoBDF	2,500	5,000	10,000	50,000	100,000	2,3,7,8-TBDF	5
2,4-DiBDF	2,500	5,000	10,000	50,000	100,000	2,3,7,8-TBDF	5
2,8-DiBDF	2,500	5,000	10,000	50,000	100,000	2,3,7,8-TBDF	5

1,3,8-TriBDF	2,500	5,000	10,000	50,000	100,000	2,3,7,8-TBDF	5
2,4,7-TriBDF	2,500	5,000	10,000	50,000	100,000	2,3,7,8-TBDF	5
2,3,4-TriBDF	2,500	5,000	10,000	50,000	100,000	2,3,7,8-TBDF	5
2,4,6,8-TBDF	0,0250	0,0500	0,1000	0,5000	1,0000	2,3,7,8-TBDF	5
1,2,7,8-TBDF	2,500	5,000	10,000	50,000	100,000	2,3,7,8-TBDF	5
2,3,7,8-TBDF	0,0250	0,0500	0,1000	0,5000	1,0000		5
1,2,3,7,8-PBDF	0,0500	0,1000	0,2000	1,0000	2,0000	2,3,4,7,8-PBDF	5
2,3,4,7,8-PBDF	0,0500	0,1000	0,2000	1,0000	2,0000		5
1,2,3,4,7,8-HBDF	0,0750	0,1500	0,3000	1,5000	3,0000		12,5
1,2,3,4,6,7,8-HpBDF	0,0938	0,1875	0,3750	1,8750	3,7500		25
OBDF	0,1250	0,2500	0,4999	2,4995	4,9990		37,5
4B-2,3,4,5-CB	0,0250	0,0500	0,0999	0,4995	0,9990		50,5
4B-2,3,3,4-CB	0,0250	0,0501	0,1001	0,5005	1,0010		49,8
4B-3,3,4,5-CB	0,0251	0,0502	0,1003	0,5015	1,0030		48,85
4B-2,3,3,4,5-CB	0,0249	0,0498	0,0995	0,4975	0,9950		49,8
4B-3,3,4,5,5-CB	0,0250	0,0500	0,1000	0,5000	1,0000		46,85
3,4B-3,4-CB	5,000	10,000	20,000	100,000	200,000	4B-3,3,4,5-CB	48,85
3,4B-3,4,5-CB	5,030	10,060	20,120	100,600	201,200	4B-3,3,4,5-CB	48,85
3,4,5B-34CB	0,0500	0,1001	0,2001	1,0005	2,0010		101,55
7-B-2,3-CDD	2,425	4,850	9,700	48,500	97,000	2,3-B-7,8-CDD	25

2-B-3,7,8-CDD	2,380	4,760	9,520	47,600	95,200	2,3-B-7,8-CDD	25
2-B-1,3,7,8-CDD	2,375	4,750	9,500	47,500	95,000	2,3-B-7,8-CDD	25
2,3-B-7,8-CDD	2,500	5,000	10,000	50,000	100,000	2,3-B-7,8-CDD	25
8-B-2,3-CDF	2,500	5,000	10,000	50,000	100,000		25
8-B-2,3,4-CDF	2,500	5,000	10,000	50,000	100,000	3-B-2,7,8-CDF	25
3-B-2,7,8-CDF	2,500	5,000	10,000	50,000	100,000		25
4-B-2,3,7,8-CDF	2,500	5,000	10,000	50,000	100,000		25
1,2-B-7,8-CDF	2,500	5,000	10,000	50,000	100,000	2,3-B-7,8-CDF	25
2,3-B-7,8-CDF	2,500	5,000	10,000	50,000	100,000		25
1,3-B-2,7,8-CDF	2,500	5,000	10,000	50,000	100,000		25

Table S2: Details of level concentration of calibration PBDD/Fs, PBBs, PXDD/Fs, and PXBs where the pollutants in gray boxes correspond to the PCB fraction and the rest correspond to dioxin fraction

PBBs	RRF (2024)	RRF (2025)	**PBDFs**	RRF (2024)	RRF (2025)	**PXBs**	RRF (2024)	RRF (2025)
PBB 3	0,69	0,42	4-MoBDF	1,95	1,21	4'-Bromo-2,3',4,5-Tetrachlorobiphenyl	1,13	1,37
PBB 15	0,84	0,94	2,4-DiBDF	2,46	1,67	4'-Bromo-2,3,3',4-Tetrachlorobiphenyl	1,1	1,10
PBB 18	0,9	1,10	2,8-DiBDF	2,15	1,61	4'-Bromo-3,3',4,5-Tetrachlorobiphenyl	/	5,14
PBB 52	0,94	1,05	1,3,8-TriBDF	0,89	0,76	4'-Bromo-2,3,3',4,5-Pentachlorobiphenyl	0,99	1,12
PBB 101	0,88	1,35	2,4,7-TriBDF	1,35	1,15	4'-Bromo-3,3',4,5,5'-Pentachlorobiphenyl	/	/
PBB 153	0,84	1,13	2,3,4-TriBDF	1,30	1,15	3,4-Dibromo-3',4'-Dichlorobiphenyl	0,91	0,91

PBB 180	0,27	0,39	2,4,6,8-TBDF	1,34	1,23	3,4-Dibromo-3',4',5'-Trichlorobiphenyl	0,86	0,78
PBB 194	0,73	0,98	1,2,7,8-TBDF	1,06	1,10	3,4-Dichloro-3',4',5'-Tribromobiphenyl	/	1,09
PBB 206	/		2,3,7,8-TBDF	/	7,61	**PXDDs**	RRF (2024)	RRF (2025)
PBB 209	/		1,2,3,7,8-PeBDF	0,82	1,04	7-Bromo-2,3-dichlorodibenzo-p-dioxin	1,51	1,50
PBDDs	RRF (2024)	RRF (2025)	2,3,4,7,8-PeBDF	1,01	1,05	2-Bromo-3,7,8-trichlorodibenzo-p-dioxin	1,21	1,19
1-MoBDD	2,05	1,48	1,2,3,4,7,8-HxBDF	0,90	0,85	2-Bromo-1,3,7,8-tetrachlorodibenzo-p-dioxin	1,19	1,24
2,3,7-TriBDD	1,31	1,24	1,2,3,4,6,7,8-HpBDF	0,76	0,77	2,3-Dibromo-7,8-dichlorodibenzo-p-dioxin	1,04	1,06
1,3,7,8-TBDD	1,12	1,18				**PXDFs**	RRF (2024)	RRF (2025)
1,2,3,4-TBDD	1,11	1,09				8-Bromo-2,3-dichlorodibenzofuran	0,96	1,07
2,3,7,8-TBDD	0,89	3,75				8-Bromo-2,3,4-trichlorodibenzofuran	1,17	1,00
1,2,4,7,8-PeBDD	1,66	1,45				3-Bromo-2,7,8-trichlorodibenzofuran	1,02	1,07
1,2,3,7,8-PeBDD	1,97	1,91				4-Bromo-2,3,7,8-tetrachlorodibenzofuran	1,0	0,98
1,2,3,4,7,8-HxBDD + 1,2,3,6,7,8-HxBDD						1,2-Dibromo-7,8-dichlorodibenzofuran	1,24	1,22
1,2,3,7,8,9-HxBDD						2,3-Dibromo-7,8-dichlorodibenzofuran	1,0	1,01
1,2,3,4,6,7,8-HpBDD	1,44	0,94				1,3-Dibromo-2,7,8-trichlorodibenzofuran	0,99	0,98
OBDD	/							

Table S3: Comparaison of RRF values in 2025 and 2024

E2159			
Pollutant	GC retention time (min)	Measured mass (Da)	CCS ($Å^2$)
MoBrTClBs	15.75	369.828	162.6
MoBrTClBs	16.65	369.829	167.3
TriBDE	14.75	405.802	161.9
TriBDE	15.25	405.802	162.1
TBDE	19.1	485.71	169.7
TBDE	19.85	485.711	169.2
TBDE	20.65	485.71	170.6
PeBDE	23.75	563.62	175.6
PeBDE	25.25	563.621	177.8
HxBDE	28.7	643.529	182.2
HxBDE	30.1	643.529	185
HpBDE	34.15	721.442	189.3
E2242			
Pollutant	GC retention time (min)	Measured mass (Da)	CCS ($Å^2$)
TriBDE	15.25	405.803	162.3
TriBDE	14.4	405.801	158.8
TBDE	19.1	485.71	169.8
TBDE	19.85	485.711	169.5
TBDE	20.65	485.71	171.6
PeBDE	23.8	563.62	175.6
PeBDE	25.2	563.62	177.6
HxBDE	28.45	643.529	183.1
HxBDE	30.15	643.529	185.5
HpBDE	34.1	721.441	189.2
E2241			
Pollutant	GC retention time (min)	Measured mass (Da)	CCS ($Å^2$)
TriBDE	14.35	405.802	157
TriBDE	15.35	405.802	161.9

TBDE	19.1	485.712	169.2
TBDE	19.85	485.711	169.6
TBDE	20.7	485.71	171.7
PeBDE	23.85	563.62	176
PeBDE	25.2	563.62	177.6
HxBDE	28.45	643.53	183.2
HxBDE	30.1	643.53	185
HpBDE	34.1	721.44	189.3
E2222			
Pollutant	GC retention time (min)	Measured mass (Da)	CCS ($Å^2$)
MoBDE	10.35	247.984	142
TriBDE	14.35	405.802	157.6
TriBDE	15.3	405.803	162.1
TriBDE	19.85	405.802	162.3
TBDE	19.15	485.711	169.6
TBDE	19.85	485.711	169.5
PeBDE	23.8	563.62	175.5
PeBDE	25.25	563.621	177.3
HBDE	28.45	643.527	182.9
HBDE	30.15	643.527	184.8
E2386			
Pollutant	GC retention time (min)	Measured mass (Da)	CCS ($Å^2$)
TBB	16.9	469.717	163.9
TBB	17.15	469.715	164.2
TBB	18.00	469.715	169.3
TBB	18.35	469.715	166.9
PBB	21.8	547.626	173.1
PBB	22.55	547.626	172.8
PBB	20.65	547.627	168.1
PBB	20.35	547.626	170.8
PBB	21.2	547.625	169.3

HxBB	23.65	627.535	175.8
HxBB	24.5	627.535	174.7
HxBB	26.1	627.534	178.7
HxBB	26.95	627.535	176.3
HxBB	25.35	627.537	172.7
HxBB	25.55	627.534	178.1
HxBB	26.5	627.535	176.3
HxBB	28.2	627.535	180.6
HpBB	29.8	705.446	182.1
HpBB	31.65	705.449	184.1
HpBB	31.9	705.447	184.1
BrTClBs	15.7	369.828	162.2
BrTClBs	16.8	369.829	163.8
BrTClBs	17.55	405.787	169
BrTClBs	17.9	405.788	170
MoBDE	10.35	247.983	142
TriBDE	14	405.802	162.8
TriBDE	14.4	405.802	164;7
TriBDE	14.6	405.801	163;6
TriBDE	14.75	405.802	162.2
TriBDE	15	405.802	165.2
TriBDE	15.3	405.802	167.4
TBDE	18.4	485.711	169.3
TBDE	18.6	485.711	173.6
TBDE	18.8	485.71	164.5
TBDE	18.95	485.71	174.4
TBDE	19.1	485.71	169.7
TBDE	20	485.71	169.8
TBDE	20.4	485.71	173
TBDE	20.65	485.71	170.4
PBDE	22.2	563.621	175.3

PBDE	22.35	563.621	178.5
PBDE	23.3	563.621	173
PBDE	23.4	563.62	176.8
PBDE	23.65	563.621	175.3
PBDE	24.25	563.621	176.4
PBDE	24.4	563.621	181.1
PBDE	20.65	563.621	173.9
PBDE	24.9	563.621	174
PBDE	25.2	563.621	177.4
PBDE	25.5	563.621	175.1
PBDE	26.3	563.621	178.8
HxBDE	27.65	643.53	179.7
HxBDE	28.4	643.53	183.4
HxBDE	29.2	643.529	175.8
HxBDE	29.45	643.529	181.1
HxBDE	30.1	643.529	185.6
HpBDE	33.1	721.44	185.1
HpBDE	33.7	721.44	183.3

Table S4: List of suspected compounds tentatively identified in dioxin fraction of chicken meat (E2159), free-range chicken eggs (E2242) and beef meat (E2222) samples

E2159			
Pollutant	GC retention time (min)	Measured mass (Da)	CCS ($Å^2$)
DiBB	11.1	311.897	149.5
DiBB	11.25	311.896	145.8
DiBB	11.4	311.896	149.7
DiBDF	14.2	325.876	147.3
DiBDF	14	325.876	146.8
DiBDF	13.6	325.875	147.1
DiBDF	13.5	325.876	145.5
TriBDF	21.25	403.787	157.3

TriBDF	20.25	403,788	154.7
TriBDF	20.7	403.787	155.7
TBDF	28.95	483.696	165.1
PeBDF	38.5	561.603	171.4
MoBr,TetraClB	18.75	369.827	164
DiBr-DiCl-DF	23.15	393.802	172.1
MoBrtetraClDF	22.9	383.811	165.1
E2242			
Pollutant	GC retention time (min)	Measured mass (Da)	CCS ($Å^2$)
DiBB	11.1	311.896	150.2
DiBDF	14	325.874	147.1
DiBDF	13.6	325.874	145.3
DiBDF	13.7	325.875	145.9
TriBDF	20.75	403.787	156
TriBDF	21.35	403.787	157.7
TBDF	29	483.694	166.3
PeBDF	38.55	561.605	172.3
MoBrTetraClB	18.8	369.828	163.4
MoBrTetraClB	17.35	369.828	162
Cl-TriBr-B	30	459.728	169.8
E2222			
Pollutant	GC retention time (min)	Measured mass (Da)	CCS ($Å^2$)
DiBB	11.1	311.895	149
DiBDF	13,6	325.874	145.2
TriBDF	21.3	403.785	156.6
TriBDF	20.7	403.786	156
TDBF	29	483.695	165.2
MoBrTetraClB	19.3	369.829	162.9

Table S5: List of suspected compounds tentatively identified in PCB fraction of chicken meat (E2159), free-range chicken eggs (E2242), beef meat (E2222), haring (E2386), and organic eggs (E2241) samples

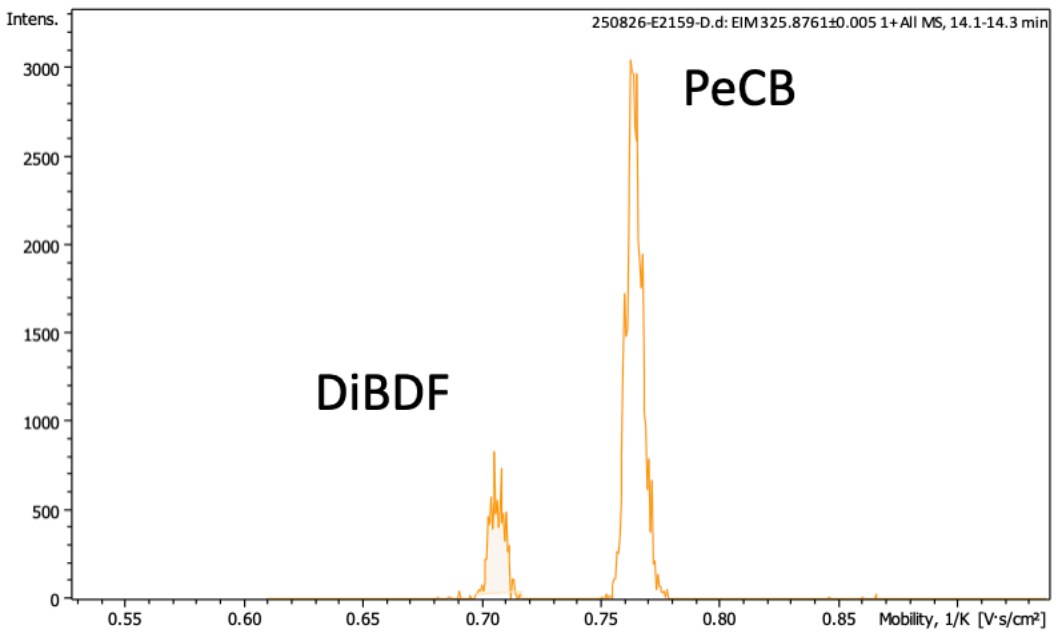

Figure S1: Extracted ion mobilogram (EIM) of dibromodibenzofuran (DiBDF) and pentacholrobiphenly (PeCB) in the chicken meat sample (E2159)

VII. Chapter3: Combining targeted and suspect screening to investigate pollutants sorbed on microplastics using a GC-APCI-TIMS-TOFMS device

A. Introduction

The industrial production of plastics began in 1907 [1], and since then, it has increased exponentially, as illustrated in Figure 1. Global plastic production reached approximately 400 million tons (Mt) in 2022 [3]. After their use, plastics may follow several pathways. While recycling is possible, only 8.9% of plastic waste was recycled in 2022 [4]. The remainder ends up in landfills, incineration facilities, or is improperly disposed of, ultimately accumulating in aquatic environments, including the oceans [5].

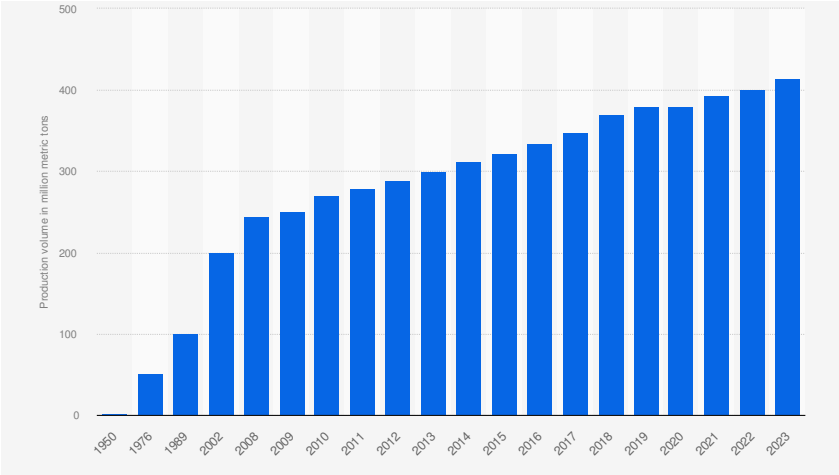

Figure 1: Annual production of plastics worldwide from 1950 to 2023 (in million metric tons) [2]

In marine environments, plastic pollution originates from two main sources. The primary source consists of large plastic items used in daily life, such as personal care products (e.g., hand and facial cleansers), cosmetic packaging, and household containers [6,7]. These macro-plastics can undergo degradation through processes such as photodegradation and mechanical abrasion by waves, leading to the formation of microplastics as secondary emission source [6].

Three main categories of plastic particles are found in the ocean. The first category is macro-plastics, defined as plastic debris with a size greater than 5 mm [6,7,8]. Over time, these degrade into microplastics, which are particles smaller than 5 mm and above 1 µm [6,7,8]. Further degradation leads to nanoplastics, with dimensions below 1 µm [6,7,8]. Several studies suggest that nanoplastics may be the more toxic form plastic due to their high surface-to-volume ratio, which enhances their capacity to adsorb environmental contaminants [6,7,8]. Additionally, some researchers propose an intermediate size category known as mesoplastics, which includes plastic particles ranging from 5 mm to 25 mm in size [8,9].

These plastic particles have the ability to adsorb a wide range of compounds and organisms, including persistent organic pollutants (POPs) such as polybrominated diphenyl ethers (PBDEs), polychlorinated biphenyls (PCBs), heavy metals, microorganisms, and many others [10]. The adsorption of these substances onto microplastics is governed by dynamic partition equilibrium between water and the surface of microplastics directed by different interactions, including hydrophobic interactions, electrostatic forces, Van der Waals forces, π-π stacking, and hydrogen bonding [10]. The exact nature of these interactions depends on several factors: the properties of the pollutants (e.g., functional groups), the characteristics of the microplastic particles (e.g., particle size, crystallinity, surface charge), and environmental parameters such as salinity, pH, temperature, and the presence of dissolved organic matter (DOM) [11].

For POPs, the main absorption mechanisms involved in the interaction with microplastics are hydrophobic interactions, due to their high hydrophobicity [11].

Since microplastics degrade slowly, they can spread widely in the ocean. As a result, this increases the mobility of absorbed POPs in the aquatic environment [11]. In addition, the ingestion of microplastics by plants and marine mammals can lead to the bioaccumulation and biomagnification of POPs throughout the trophic chain.

Currently, there are two main types of analytical approaches for the characterization of the contaminants adsorbed on microplastics: targeted and non-targeted approaches [10]. Non-targeted approaches have recently gained increased momentum due to the possibility to more comprehensive characterize the chemical risk associated with the release of microplastics into the environment [10]. Common analytical methods include gas chromatography coupled with mass spectrometry for the analysis of hydrophobic compounds, and liquid chromatography coupled with mass spectrometry for the analysis of hydrophilic compounds [10]. These two methods are complementary, and enable to obtain a larger spectrum of the types of contaminants adsorbed on microplastics.

B. Objective

The objective of this chapter involves the investigation of pollutants absorbed on MPs using a gas chromatography-atmospheric pressure chemical ionization-trapped ion mobility spectrometry-time-of-flight mass spectrometry (GC-APCI-TIMS-TOFMS) platform.

Through targeted analyses using PCB and PBDE standards, as well as suspect screening based on a predefined list of potentially present POPs, the objective of this part will be to characterize the diversity and concentrations of halogenated pollutants present in microplastics and macroplastics collected from two different rivers in Madagascar and Belgium.

C. Materials and methods

1. Sample preparation

The chemical analysis of POPs adsorbed onto microplastics of Madagascar and Sambre and macroplastics of Sambre was performed by GC-APCI-TIMS-TOFMS [1] using the isotope dilution method. Sample preparation was carried out as follows: 78 mg of the Madagascar microplastic mixture, 1.4 mg of the Sambre microplastic mixture and 291 mg of the Sambre macroplastic mixture were placed in separate glass vials and spiked with 2 ng of a ^{13}C standard mixture of indicator polychlorinated biphenyls (PCBs 28, 52, 101, 138, 153 and 180) and 2 ng of a ^{13}C standard mixture of polybrominated diphenyl ethers (PBDEs 28, 47, 99, 100, 153, 154 and 183). The samples were left for several hours to allow the standards to equilibrate with the microplastic surfaces. Subsequently, 2 mL of trace-contaminant-grade n-hexane was added to the Madagascar microplastic sample, 0.04 mL to the Sambre microplastic sample, and 5 mL to the Sambre macroplastic sample (Biosolve, Dieuze, France). The suspensions were vortexed for 30 seconds and then left to stand, enabling the extraction of the target contaminants from the plastics.

After 20 h, 100 µL of the supernatants were carefully transferred individually onto a sodium sulfate (Na_2SO_4) column previously conditioned with n-hexane. The analytes were eluted with 2 mL of n-hexane and collected in test tubes. This step served to remove residual water and filter out any remaining plastic fragments. The eluates were subsequently concentrated to ~200 µL in a hot water bath (40 °C) under a gentle stream of nitrogen (N_2). The concentrates were quantitatively transferred to GC vials containing 100 µL of keeper solvent (n-nonane) and further reduced to 100 µL under a nitrogen stream. Finally, 2 ng of ^{13}C PCB 80 recovery standard was added. The vials were sealed and stored at 4 °C until analysis. Procedural blanks were prepared in parallel following the exact same protocol.

2. GC-APCI-TIMS-TOFMS instrument

Measurements were performed on a commercial timsTOF Pro 2 mass spectrometer (Bruker, Bremen) equipped with a Scion 456-GC connected to an APCI source for sample introduction and ionization (GC- APCI II, Bruker, Bremen).
Injections were conducted in splitless mode (injection temperature 275 °C, 1 µL). The GC column was a low polarity Rxi-5Sil MS column (30 m × 0.25 mm × 0.25 µm, Restek). Helium (grade 6.0, Air Liquide, Belgium) was used as the carrier gas. Ion mobility separations were performed by TIMS.

3. Methods

For GC–timsMS analysis, data were processed using DataAnalysis software (Bruker, version 5.3). For sample analysis, peak integration was based on the area of the ion mobility peaks. Internal recalibration of *m/z* and ion mobility was performed using siloxanes originating from column bleed prior to data acquisition and data processing.

D. Results and discussions

1. Targeted analysis of sorbed POPs in microplastics and macroplastics samples

a) Targeted analysis of microplastics Madagascar sample

Targeted analysis (TA) enabled the quantification of selected PBDE and PCB congeners, as shown in Figure 2 for the first sample. The concentrations of the selected PCBs were one to two orders of magnitude higher than those of the corresponding PBDEs. All the targeted congeners of PCBs and PBDEs were detected, except for PBDE congeners 28 and 100.

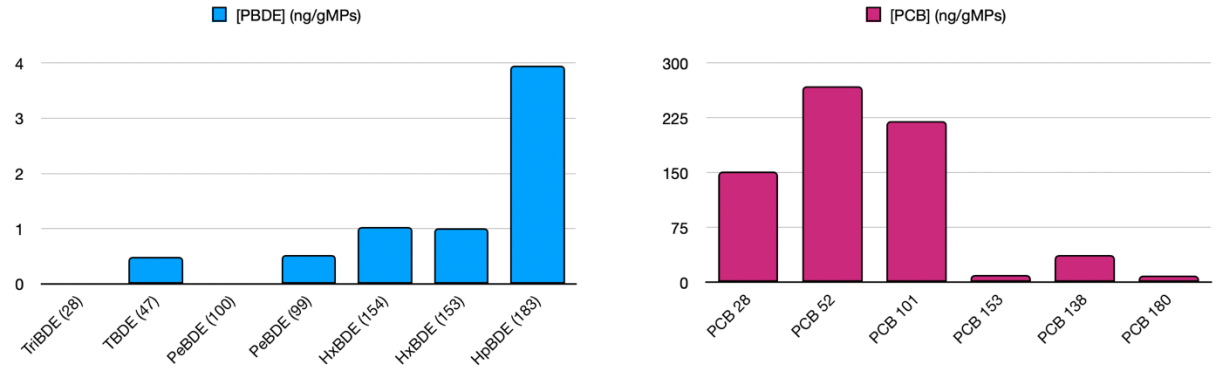

Figure 2: the concentrations of PCBs and PBDEs of Madagascar microplastics selected to TA

b) Targeted analysis of microplastics and macroplastics Sambre samples

The second samples, originating from the river Sambre in Belgium, included two samples: one of microplastics and one of macroplastics.

Targeted analysis of microplastic samples enabled the quantification of selected PBDE and PCB congeners, as shown in Figure 3. The concentrations of the selected PCBs were approximately two orders of magnitude higher than those of the PBDEs. All targeted PCB congeners were detected, whereas only one PBDE congener, BDE-47, was identified. Similar results were obtained for the macroplastic sample (Figure 4).

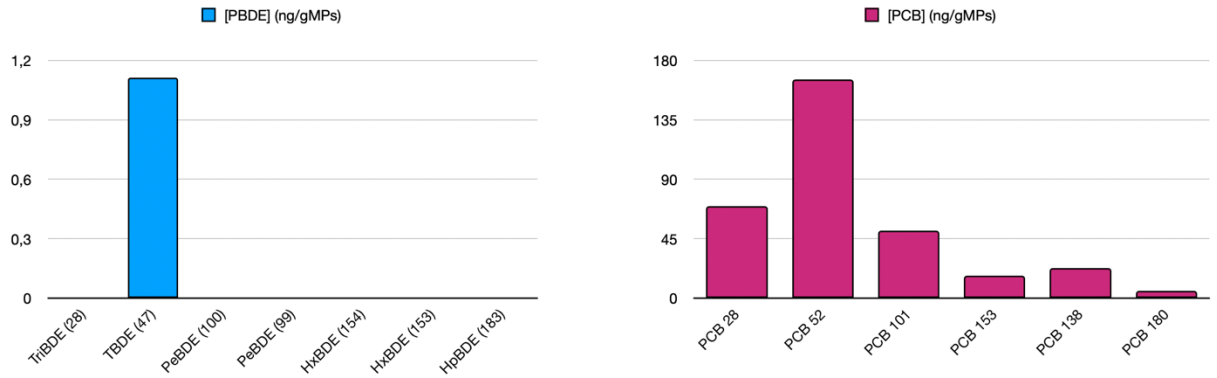

Figure 3: the concentrations of PCBs and PBDEs of Sambre microplastics selected to TA

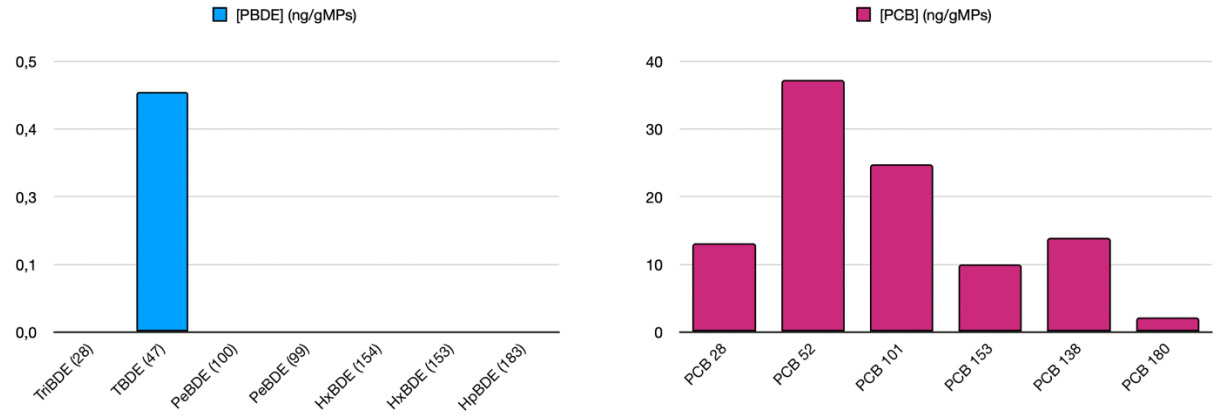

Figure 4: the concentrations of PCBs and PBDEs of Sambre macroplastics selected to TA

The quantified concentrations of targeted PCBs in microplastics from Madagascar and the Sambre River were at the same order of magnitude. These results are also consistent with those reported by Emma L. *et al.* for microplastic samples collected along the Japanese coasts, one of the most industrialized regions [12]. In that study, PCB concentrations ranged from 4 to 117 ng/g, while PBDE concentrations ranged from 0.9 to 2.1 ng/g. These values are of the same order of magnitude as those obtained in the present study. Such a trend is plausible given the widespread historical use of these POPs in industrial applications as plastic additives [13,14].

However, PCB concentrations in microplastics from Madagascar were higher than those measured in the Sambre River samples. This difference may be attributed to limited infrastructure and insufficient management of waste, particularly textile, plastics and paint manufactured associated with the specific industrial activities of the capital of Madagascar, which could result in higher environmental release of POPs [15].

The PBDE congener profiles differed between the Madagascar and Sambre samples. In the Madagascar sample, collected downstream of the city of Antananarivo, the generally higher concentrations observed for highly brominated PBDEs are consistent with the extensive use of commercial PBDE mixtures, namely c-octaPBDE, c-decaPBDE, and c-pentaPBDE, as plastic additives [16,17]. However, the absence of detectable PeBDE-100 is inconsistent with this trend and may indicate concentrations below the limit of quantification (LOQ).

In addition, the concentration of HpBDE (BDE-183) was higher than that of the other PBDE congeners. This observation may be explained by the presence of DecaBDE (BDE-209) at significant concentrations, although this compound was not directly detectable using the applied analytical technique. BDE-209 was the dominant congener in the commercial c-decaPBDE mixture, which was widely used in electronic goods [17]. It has been demonstrated that BDE-209 can undergo debromination under anaerobic conditions, leading to the formation of lower-brominated PBDEs, including heptabrominated congeners [16,18].

In the Sambre samples, only one PBDE congener, BDE-47, was identified (Figure 4). This finding is consistent with historical usage patterns in Europe, where BDE-47 was one of the most extensively used PBDE congeners, primarily as a flame retardant in polyurethane foams [19].

For the macroplastic sample, the concentrations of both PCBs and PBDEs were lower than those measured in microplastics. This difference may be attributed to the lower surface-area-to-volume ratio of macroplastics, which limits the sorption and accumulation of hydrophobic organic pollutants.

Across all three samples, PCB concentrations were consistently two orders of magnitude higher than PBDE concentrations, a trend also reported by Emma *et al.* This may reflect the historically high production volumes and widespread use of PCBs in industrial products [20].

Finally, PCB congeners 28, 52, and 101 exhibited higher concentrations in all three samples. This is consistent with the product because the tri-, tetra- and penta-chlorinated biphenyls were among the most produced congeners [21]. These congeners are commonly encountered in indoor environments and construction materials, which raises the possibility of contamination during sample handling or preparation. Although blank corrections were applied during concentration determination, the relatively small mass of plastic samples analyzed may have increased susceptibility to background contamination.

2. Suspect screening analysis of sorbed POPs in micro and macroplastics samples

a) Suspect screening analysis of microplastics Madagascar sample

A suspect screening was performed on the sample. The PCB chromatograms indicated the presence of numerous congeners beyond those initially targeted. For example, the extracted ion chromatograms (EICs) of the tetra- and penta-chlorinated biphenyls were characterized by a large number of peaks in addition to those corresponding to the target PCBs 52 and 101, respectively (Figure S1, in Supporting Information (SI)). While most of these additional peaks were less intense than the target PCBs, some were of similar or higher intensity. Each additional peak was checked for mass accuracy, isotopic pattern and CCS to confirm that the signals were indeed produced by PCBs. In this way, 14 additional TCBs and 16 PeCBs were tentatively identified. Overall, 69 additional PCBs congeners spanning various chlorination degree were tentatively identified (Table S1, SI).

In addition to PCBs, other suspected classes of contaminants were investigated. Polychlorinated dibenzo-p-dioxins (PCDDs) and dibenzofurans (PCDFs), polybrominated biphenyls (PBBs; brominated analogues of PCBs), several organochlorinated pesticides (OCPs), and additional PBDE congeners were not detected (Table S2, SI). In contrast, six polychlorinated naphthalenes (PCNs), hexachlorobenzene (HCB), *o,p'*- and *p,p'*-DDT, along with their corresponding DDE and DDD metabolites, were tentatively identified (Table S1, SI). The detection of DDT-related compounds

is consistent with previous findings reporting elevated concentrations of HCHs and DDTs in South Africa [12]. Similarly, higher concentrations of PCNs have also been reported in South Africa [22].

b) Suspect screening analysis microplastics and macroplastics of Sambre samples

A suspect screening analysis of these samples was also conducted, as the chromatograms indicated the presence of numerous additional PCB congeners. Each additional peak was scrutinized for mass accuracy, isotopic pattern, and CCS to ensure that the signals were indeed attributable to PCBs.

Using this approach, 30 additional PCB congeners were tentatively identified in the microplastic sample and 55 additional congeners in the macroplastic sample, covering a wide range of chlorination degrees (listed in Tables S3-S4, SI). All PCBs tentatively identified in the microplastic sample were also detected in the macroplastic sample from the Sambre River. However, given the small amount of microplastics material analyzed, PCB congeners not detected in the microplastic sample may still have been present at concentrations below the limit of quantification (LOQ).

For many compounds in the microplastic sample, the intensity differences between the blank and the sample were not significant. This observation was particularly evident for PeCBs, as illustrated in Figure S2, SI. Conversely, the macroplastic sample exhibited more pronounced differences in intensity relative to the blank, especially for PeCBs (see in Figure S3, SI).

In addition to PCBs, the presence of other classes of suspected contaminants were screened using the same approach as for the Madagascar sample. Among the compounds investigated only methoxychlor was tentatively detected (see in Table S3-S4, SI).

E. Intermediate conclusion

This study quantified selected PCB and PBDE congeners in three plastic samples: one microplastic sample from Madagascar and two samples from the Sambre River (Belgium), comprising one microplastic and one macroplastic sample. In addition, a suspect screening strategy was performed to each sample to broaden the chemical characterization.

The targeted analysis enabled the quantification of selected PBDE and PCB congeners, of which the concentrations were compared with a study performed in Japanese coasts and the same order of magnitude was evaluated. Across all samples, PCB concentrations were consistently about two orders of magnitude higher than PBDE concentrations.

The suspected screening analysis tentatively identified a large number of additional compounds that were not included in the targeted analysis. Tentative identification relied on accurate mass measurements, isotopic patterns, and collision cross section (CCS) values, highlighting the chemical complexity of micro- and macroplastic-associated contaminants and demonstrating the complementarity of targeted and suspected screening approaches.

F. References

[1] ‘L’histoire Du Plastique | Boîte à Outils | Emploi Plasturgie’. Accessed 14 May 2025. https://www.emploi-plasturgie.org/boite-outils/lhistoire-du-plastique.
[2] Statista. ‘Global Plastic Production’. Accessed 14 May 2025. https://www.statista.com/statistics/282732/global-production-of-plastics-since-1950/.
[3] Plastics Europe. ‘Plastics – the Fast Facts 2023 • Plastics Europe’. Accessed 14 May 2025. https://plasticseurope.org/knowledge-hub/plastics-the-fast-facts-2023/.
[4] mikelamema. ‘Plastics Europe Launches Plastics – the Fast Facts 2023 • Plastics Europe’. Plastics Europe (blog), 19 October 2023. https://plasticseurope.org/media/plastics-europe-launches-the-plastics-the-fast-facts-2023/.
[5] ’91% Des Déchets Plastiques Ne Sont Pas Recyclés | National Geographic’. Accessed 27 May 2025. https://www.nationalgeographic.fr/environnement/91-des-dechets-plastiques-ne-sont-pas-recycles.
[6] Pozo, Karla, Williams Urbina, Victoria Gómez, Mariett Torres, Dariela Nuñez, Petra Přibylová, Ondřej Audy, et al. ‘Persistent Organic Pollutants Sorbed in Plastic Resin Pellet — “Nurdles” from Coastal Areas of Central Chile’. Marine Pollution Bulletin 151 (1 February 2020): 110786. https://doi.org/10.1016/j.marpolbul.2019.110786.
[7] ‘A Thermodynamic Approach for Assessing the Environmental Exposure of Chemicals Absorbed to Microplastic | Environmental Science & Technology’. Accessed 14 May 2025. https://pubs.acs.org/doi/10.1021/es1032025.
[8] Arias, Andres H., Guadalupe Alvarez, Karla Pozo, Petra Pribylova, Jana Klanova, Lucas S. Rodríguez Pirani, A. Lorena Picone, Mónica Alvarez, and Norma Tombesi. ‘Beached Microplastics at the Bahia Blanca Estuary (Argentina): Plastic Pellets as Potential Vectors of Environmental Pollution by POPs’. Marine Pollution Bulletin 187 (1 February 2023): 114520. https://doi.org/10.1016/j.marpolbul.2022.114520.
[9] Lee, Jongsu, Jongmyoung Lee, Sunwook Hong, Sang Hee Hong, Won Joon Shim, and Soeun Eo. ‘Characteristics of Meso-Sized Plastic Marine Debris on 20 Beaches in Korea’. Marine Pollution Bulletin 123, no. 1 (15 October 2017): 92–96. https://doi.org/10.1016/j.marpolbul.2017.09.020.
[10] Samaei, Seyed Hesam-Aldin, Parnian Mojahednia, Jianfei Chen, Zhenyu Li, Katarzyna Jaszczyszyn, Edyta Kiedrzyńska, and Jinkai Xue. ‘What Does the “Trojan Horse” Carry? The Pollutants Associated with Microplastics/Nanoplastics in Water Environments’. ACS ES&T Water 5, no. 4 (11 April 2025): 1530–45. https://doi.org/10.1021/acsestwater.4c01089.
[11] Song, Xiaocheng, Wen Zhuang, Huizhen Cui, Min Liu, Teng Gao, Ao Li, and Zhenhui Gao. ‘Interactions of Microplastics with Organic, Inorganic and Bio-Pollutants and the Ecotoxicological Effects on Terrestrial and Aquatic Organisms’. Science of The Total Environment 838 (10 September 2022): 156068. https://doi.org/10.1016/j.scitotenv.2022.156068.
[12] Teuten, Emma L., Jovita M. Saquing, Detlef R. U. Knappe, Morton A. Barlaz, Susanne Jonsson, Annika Björn, Steven J. Rowland, et al. ‘Transport and Release of Chemicals from Plastics to the Environment and to Wildlife’. Philosophical Transactions of the Royal Society B: Biological Sciences 364, no. 1526 (27 July 2009): 2027–45. https://doi.org/10.1098/rstb.2008.0284.
[13] The secretariat of the Stockholm convention. ‘Ridding the world of POPs: a guide to the Stockholm convention on persistent organic pollutants’. The United Nations Environment Programme (August 2010).

[14] Lavandier, Ricardo, Natalia Quinete, Rachel Ann Hauser-Davis, et al. 'Polychlorinated Biphenyls (PCBs) and Polybrominated Diphenyl Ethers (PBDEs) in Three Fish Species from an Estuary in the Southeastern Coast of Brazil'. *Chemosphere* 90, no. 9 (2013): 2435–43. https://doi.org/10.1016/j.chemosphere.2012.11.001.
[15] Rabezanahary, Andry Ny Aina. Environmental Microplastics Toxicity in Focus: Riverine Spatio-Temporal Distribution and Hazard Assessment in Freshwater Fish Based on in Situ and in Vivo Approaches. n.d., p61
[16] Shi, Guangyu, Hua Yin, Jinshao Ye, Hui Peng, Jun Li, and Chunling Luo. 'Aerobic Biotransformation of Decabromodiphenyl Ether (PBDE-209) by Pseudomonas Aeruginosa'. *Chemosphere* 93, no. 8 (2013): 1487–93. https://doi.org/10.1016/j.chemosphere.2013.07.044.
[17] English, Karin, Leisa-Maree L. Toms, Christie Gallen, and Jochen F. Mueller. 'BDE-209 in the Australian Environment: Desktop Review'. *Journal of Hazardous Materials* 320 (December 2016): 194–203. https://doi.org/10.1016/j.jhazmat.2016.08.032.
[18] Deng, Hua, Ruilong Li, Beizhan Yan, et al. 'PAEs and PBDEs in Plastic Fragments and Wetland Sediments in Yangtze Estuary'. *Journal of Hazardous Materials* 409 (May 2021): 124937. https://doi.org/10.1016/j.jhazmat.2020.124937.
[19] A lcock, R. 'Understanding Levels and Trends of BDE-47 in the UK and North America: An Assessment of Principal Reservoirs and Source Inputs'. *Environment International* 29, no. 6 (2003): 691–98. https://doi.org/10.1016/S0160-4120(03)00120-X.
[20] Yeo, Bee Geok, Hideshige Takada, Rei Yamashita, et al. 'PCBs and PBDEs in Microplastic Particles and Zooplankton in Open Water in the Pacific Ocean and around the Coast of Japan'. *Marine Pollution Bulletin* 151 (February 2020): 110806. https://doi.org/10.1016/j.marpolbul.2019.110806.
[21] Breivik, Knut, Andy Sweetman, Jozef M. Pacyna, and Kevin C. Jones. 'Towards a Global Historical Emission Inventory for Selected PCB Congeners — A Mass Balance Approach'. *Science of The Total Environment* 377, nos 2–3 (2007): 296–307. https://doi.org/10.1016/j.scitotenv.2007.02.026.
[22] Jaward, Foday M., Jonathan L. Barber, Kees Booij, and Kevin C. Jones. 'Spatial Distribution of Atmospheric PAHs and PCNs along a North–South Atlantic Transect'. *Environmental Pollution* 132, no. 1 (2004): 173–81. https://doi.org/10.1016/j.envpol.2004.03.029.

G. Supporting Information

Pollutants	GC retention time (min)	Measured mass (Da)	CCS ($Å^2$)
DiCB	16.0	222.000	140.6
DiCB	17.1	222.000	143.7
DiCB	17.5	222.000	141.4
TriCB	17.3	255.960	147.5
TriCB	17.8	255.961	147.3
TriCB	18.4	255.961	149.8
TriCB	18.9	255.961	147.9
TriCB	19.1	255.961	147.8
TriCB	20.4	255.961	148.7
TCB	18.9	291.919	152.6
TCB	19.2	291.918	150.9
TCB	19.4	291.919	151.6
TCB	19.6	291.919	154.9
TCB	20.1	291.919	154.7
TCB	20.1	291.919	153.9
TCB	20.3	291.919	154.3
TCB	20.4	291.918	153.9
TCB	20.6	291.918	153.1
TCB	21.0	291.919	155.0
TCB	21.1	291.918	155.0
TCB	21.2	291.918	155.1
TCB	21.3	291.918	155.2
TCB	21.7	291.918	154.2
PeCB	21.3	325.880	159.7
PeCB	21.4	325.879	159.2
PeCB	21.8	325.879	162.2
PeCB	21.8	325.879	158.4
PeCB	22.0	325.879	160.7
PeCB	22.2	325.879	160.7

PeCB	22.3	325.879	161.1
PeCB	22.4	325.880	160.3
PeCB	22.6	325.879	160.4
PeCB	22.7	325.879	159.8
PeCB	22.8	325.880	160.5
PeCB	23.1	325.879	158.9
PeCB	23.3	325.879	162.4
PeCB	23.4	325.879	162.2
PeCB	23.5	325.879	162.1
PeCB	24.2	325.879	160.4
HxCB	22.7	359.841	163.2
HxCB	22.8	359.841	166.0
HxCB	23.1	359.840	165.9
HxCB	23.2	359.840	165.1
HxCB	23.3	359.840	165.4
HxCB	23.4	359.840	165.1
HxCB	23.7	359.840	163.5
HxCB	23.9	359.840	167.8
HxCB	24.4	359.840	166.6
HxCB	24.6	359.840	165.7
HxCB	24.6	359.840	166.5
HxCB	24.7	359.840	166.4
HxCB	24.8	359.840	166.3
HxCB	25.4	359.840	165.1
HxCB	26.1	359.840	167.5
HpCB	24.4	393.801	167.8
HpCB	24.9	393.800	172.0
HpCB	25.1	393.800	171.6
HpCB	25.7	393.801	170.2
HpCB	25.8	393.800	170.6
HpCB	26.0	393.801	169.6
HpCB	26.3	393.800	173.2

HpCB	26.5	393.801	173.1
HpCB	27.1	393.801	171.4
OCB	25.9	429.759	174.3
OCB	27.3	429.759	177.1
OCB	28.2	429.760	175.5
OCB	28.7	429.760	178.2
DeCB	30.2	497.682	186.2
TriCN	16.6	229.946	138.2
TriCN	17.7	229.946	136.7
TCN	18.5	265.903	145.0
TCN	19.0	265.903	143.6
TCN	19.3	265.903	144.6
TCN	20.4	265.903	142.4
PeCN	21.5	299.864	150.1
PeCN	21.9	299.862	150.2
Hexachlorobenzene	16.1	283.809	140.1
op'-DDE	21.8	317.934	161.3
pp'-DDE	22.7	317.934	165.6
pp'-DDD	22.8	235.008 [M-CCl2]+	147.7
op'-DDD	23.7	235.008 [M-CCl2]+	147.7
pp'-DDT	23.8	235.008 [M-CCl3]+	147.7
op'-DDT	24.7	235.008 [M-CCl3]+	147.7

Table S1: List of suspected compounds tentatively identified in the Madagascar microplastic extract

Pollutants
Polychloro dibenzodioxins (PCDDs)
Polychloro dibenzofurans (PCDFs)
Polybrominated biphenyls (PBBs)

Hexachloro cyclohexanes (a, b, g and d HCHs)
Aldrin
Dieldrin
Heptachlor
Heptachlor epoxide (cis and trans)
Endosulfan sulfate

Table S2: List of suspect screening compounds not detected in the Madagascar microplastic extract

Pollutants	GC retention time (min)	Measured mass (Da)	CCS ($Å^2$)
DiCB	17,1	222.001	142,5
TriCB	17,2	255.961	146,8
TriCB	18,8	255.961	147,3
TCB	19,6	291.919	154,2
TCB	19,7	291.919	153,6
TCB	20	291.919	153,8
TCB	20,1	291.918	152,9
TCB	20,4	291.918	153,4
TCB	20,6	291.919	152,7
TCB	21,1	291.919	155
PeCB	21,8	325.879	161,2
PeCB	22,3	325.880	159,3
PeCB	21,4	325.880	158,6
PeCB	21,7	325.880	158,1
PeCB	22,5	325.880	159,4
PeCB	22,7	325.879	159,4
HxCB	23	359.840	166
HxCB	23,6	359.841	164,3
HxCB	23,7	359.841	163,8
HxCB	23,9	359.840	167,5
HxCB	24,1	359.840	167,6
HxCB	24,7	359.841	166,3
HpCB	24,9	393.802	171,3
HpCB	25,2	393.802	170,6
HpCB	25,7	393.801	169,8
HpCB	25,8	393.801	169,9
HpCB	25,9	393.803	169,9
HpCB	26,4	393.802	172,2

HpCB	27,1	393.802	171,4
OCB	25,9	429.760	174,3
OCB	27,4	429.760	176,7
Methoxychlor	24,6	227.107	151,9

Table S3: List of suspected compounds tentatively identified in the Sambre microplastic extract

Pollutants	GC retention time (min)	Measured mass (Da)	CCS ($Å^2$)
DiCB	16	222.000	139
DiCB	17.1	222.001	141.5
DiCB	18.6	222.000	140.7
DiCB	18.8	221.999	141.7
TriCB	17.3	255.961	146.5
TriCB	17.8	255.961	146.5
TriCB	18.8	255.961	146.9
TriCB	19	255.960	146.4
TCB	18.8	291.918	151.9
TCB	19.1	291.918	150.8
TCB	19.6	291.918	154.1
TCB	19.7	291.918	152.8
TCB	20	291.918	153.7
TCB	20.1	291.918	153.4
TCB	20.3	291.918	153.2
TCB	20.4	291.918	152.9
TCB	21	291.919	154.3
TCB	21.1	291.918	154.9
TCB	21.6	291.918	153.5
PeCB	21.2	325.879	158.7
PeCB	21.4	325.879	158.2
PeCB	21.7	325.880	162.3
PeCB	21.7	325.880	157.9
PeCB	22	325.879	159.8
PeCB	22.3	325.879	159.1
PeCB	22.5	325.879	159.3
PeCB	22.6	325.880	158.9
PeCB	22.8	325.879	159.2
PeCB	23	325.879	158.5
PeCB	23.5	325.879	161.7
PeCB	24.1	325.879	159.2
HxCB	22.6	359.840	163
HxCB	23	359.840	165.9
HxCB	23.1	359.840	165.4

HxCB	23.3	359.841	165.2
HxCB	23.6	359.840	163.8
HxCB	23.9	359.840	167
HxCB	24.3	359.840	165.9
HxCB	24.5	359.839	165.7
HxCB	24.6	359.841	166.3
HxCB	24.7	359.840	166.2
HxCB	24.9	359.840	165.3
HxCB	25.4	359.840	165.4
HpCB	24.3	393.802	167.8
HpCB	24.8	393.802	171.8
HpCB	25.1	393.803	171.1
HpCB	25.2	393.802	170.2
HpCB	25.6	393.800	169.8
HpCB	25.8	393.801	169.9
HpCB	25.9	393.802	169.5
HpCB	26.4	393.800	173.2
HpCB	27.1	393.802	170.8
OCB	27.2	429.759	176.8
OCB	27.4	429.760	176.2
Methoxychlor	24.6	227.106	152.2

Table S4: List of suspected compounds tentatively identified in the Sambre macroplastics extract

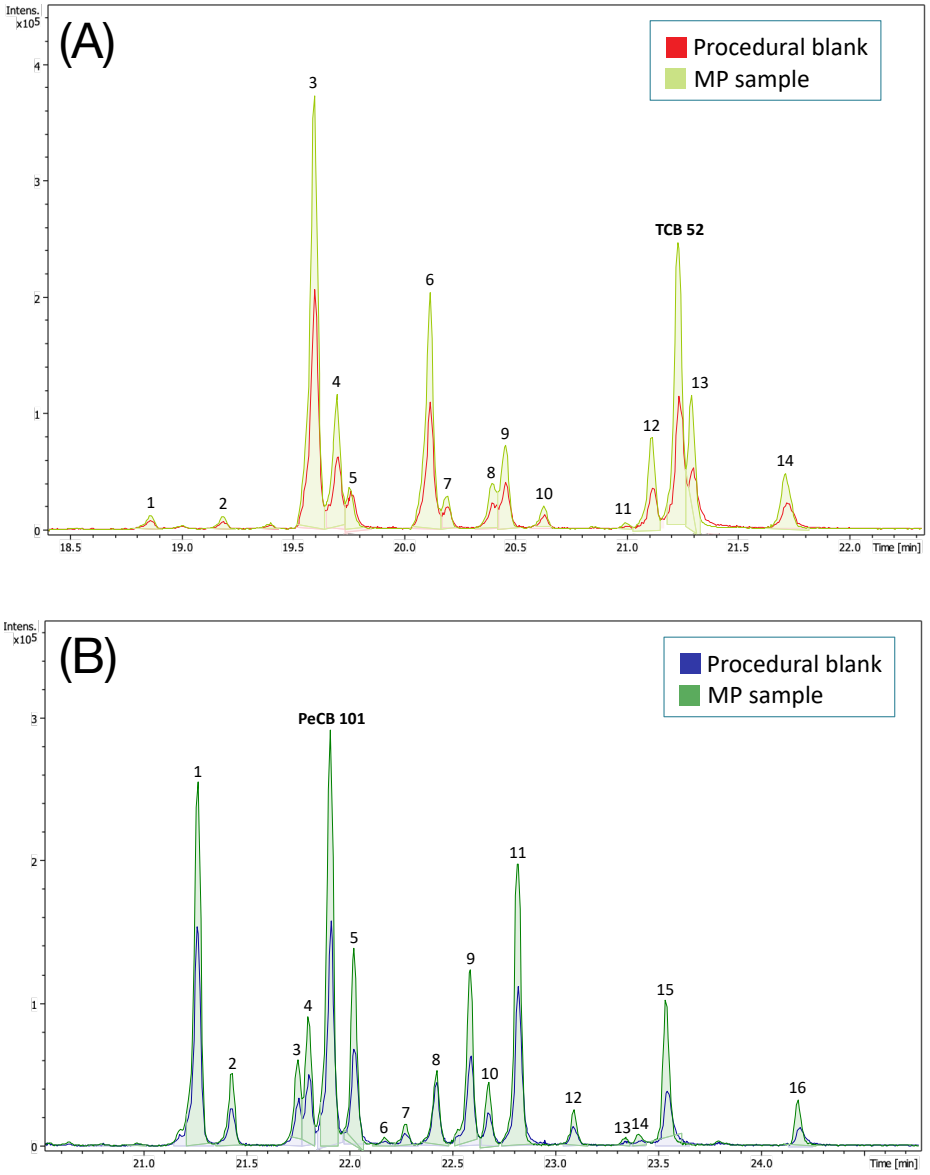

Figure S1 : Extracted ion chromatogram (EIC) of (A) tetrachlorinated biphenyls (TCBs) and (B) pentrachlorinated biphenyls (PeCBs) from the analysis of the Madagascar microplastic mixture

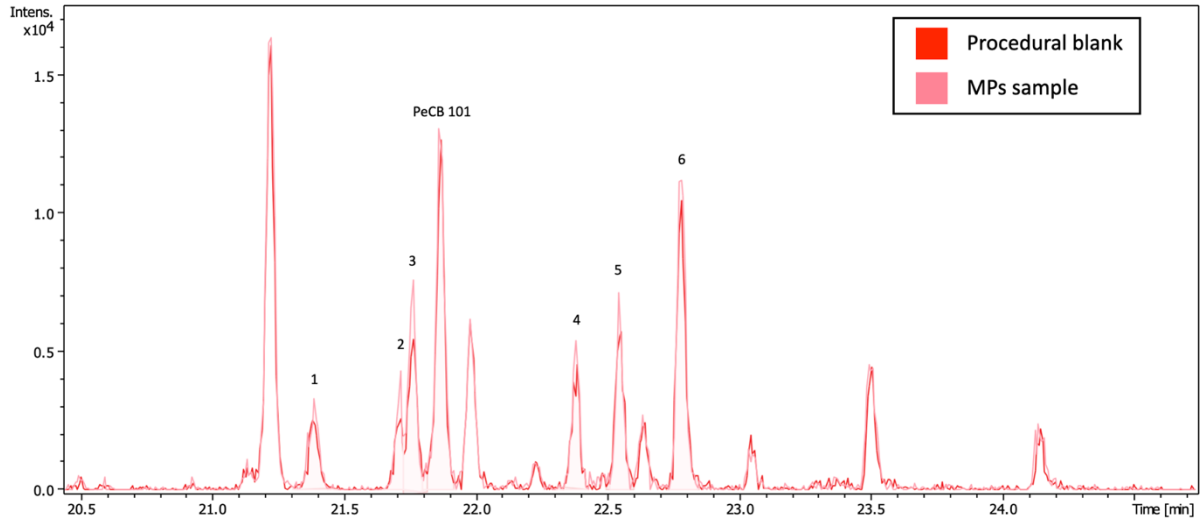

Figure S2: Extracted ion chromatogram (EIC) of pentachlorinated biphenyls (PeCBs) from the analysis of the Sambre microplastic mixture

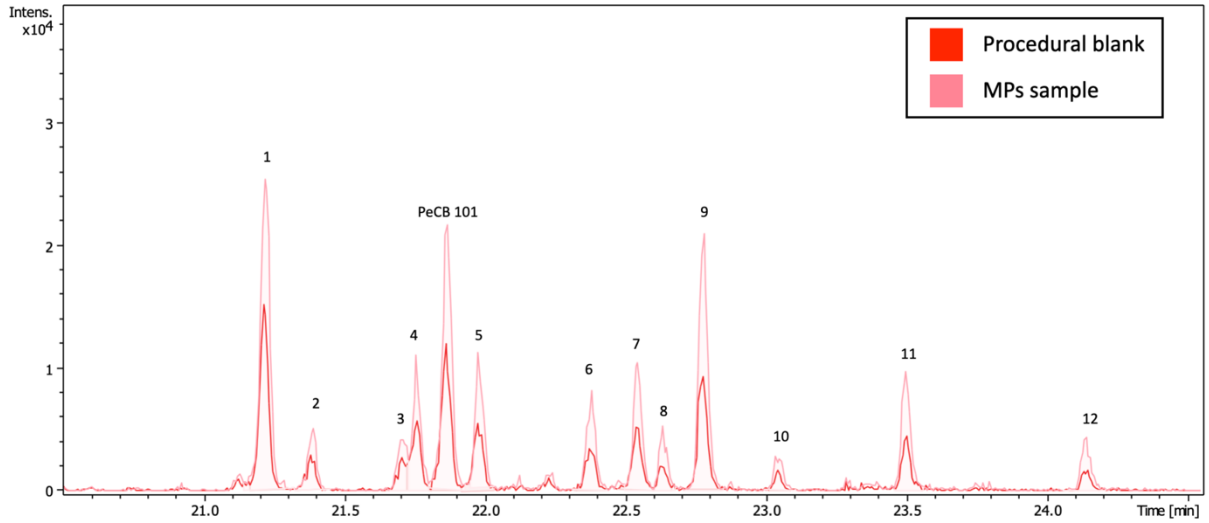

Figure S3: Extracted ion chromatogram (EIC) of pentachlorinated (PeCBs) from the analysis of the Sambre macroplastics mixture

VIII. General conclusions and perspectives

This Master's thesis evaluated GC-APCI-TIMS-TOFMS as an analytical platform for the investigation of halogenated volatile and semi-volatile persistent organic pollutants (POPs). The work combined method development for volatile PFAS, performance benchmarking for ultra-trace halogenated POPs in food matrices, and the analysis of POPs associated with microplastics and macroplastics using targeted quantification complemented by suspect screening.

In Chapter 1, a method was developed for the analysis of three volatile per- and polyfluoroalkyl substances (PFAS), namely perfluorooctyl ethanol (FTOH), N-methylperfluoro-1-octanesulfonamide (N-MeFOSA), and 2-(N-methylperfluoro-1-octanesulfonamido) ethanol (N-MeFOSE), using a GC-APCI-TIMS-TOFMS instrument. Fragmentation patterns were investigated, and source, TIMS, and TOF parameters were successfully optimized through a combination of classical optimization and design of experiments (DOE). A specific analytical challenge was also addressed, as the broad ion mobility peak observed for N-MeFOSA could be attributed to a combination of space-charge effects and the presence of multiple protonation sites with similar collision cross section (CCS) values.

In Chapter 2, GC-APCI-TIMS-TOFMS performance was assessed for brominated and mixed halogenated POPs in food matrices and compared with the reference GC-EI-sector HRMS method. While the reference method remained superior for the most demanding ultra-trace quantification, TIMS provided an additional separation dimension that increased confidence in compound identification, notably through CCS information and improved discrimination of coeluting species.

In Chapter 3, selected PCB and PBDE congeners were quantified in microplastics and macroplastic samples, and suspect screening revealed numerous additional PCB congeners and other contaminants, illustrating the chemical complexity of plastic-associated mixtures. This chapter highlighted the complementarity of targeted quantification and suspect screening, while also underlining the importance of blank control and sample amount for robust interpretation at trace levels.

Future work should address both methodological and application-driven aspects. For volatile PFAS, further theoretical and experimental investigations are needed to better substantiate the origin of the broad N-MeFOSA mobility peak (e.g., controlled ion population studies and protonation-site/CCS modelling) and to improve chromatographic performance, including mitigation of adsorption and peak tailing through optimized injection conditions and the use of an alternative liner. For food analysis, improving quantification reproducibility should include mobility-filtered integration strategies, extended calibration for additional families, and comprehensive validation in representative matrices. For plastic-associated contaminants, expanding the number of samples and strengthening QA/QC (including procedural blanks and contamination control) will be essential to support environmental interpretation. Finally, extending the approach to a broader range of PFAS and POPs, together with CCS-supported

identification workflows, would further consolidate GC-APCI-TIMS-TOFMS as a tool for advanced targeted and screening analyses.